MASTER THESIS

Cold Modelling of a Fluidized Bed System with the Utilization of Helium towards Hydrogen

Carried out for the purpose of obtaining the degree of

Master of Science

at the

Institute of Chemical, Environmental and Bioscience Engineering,

supervised by

Univ.Prof. Dipl.-Ing. Dr.techn. Franz Winter

Dipl.-Ing. Sandra Jezernik BSc

Submitted Technische Universität Wien

Faculty of Technical Chemistry

by

Betina Kipper Pires

Matrikelnummer 11701282

Wien, on 15.03.2024

I confirm, that going to press of this thesis unter the term

Master thesis

needs the confirmation of the examination committee.

Affidavit

I declare in lieu of oath, that I wrote this thesis and performed the associated research myself, using only literature cited in this volume. If text passages from sources are used literally, they are marked as such.

I confirm that this work is original and has not been submitted elsewhere for any examination, nor is it currently under consideration for a thesis elsewhere.

I acknowledge that the submitted work will be checked electronically-technically using suitable and state-of-the-art means (plagiarism detection software). On the one hand, this ensures that the submitted work was prepared according to the high-quality standards within the applicable rules to ensure good scientific practice "Code of Conduct" at the TU Wien. On the other hand, a comparison with other student theses avoids violations of my personal copyright.

Vienna, on 15.03.2024

Betina Kipper Pires

Abstract

The steel industry contributes approximately 2.8 gigatonnes of CO_2 annually, constituting 8 % of total energy system emissions. Austria's steel sector is responsible for up to 15 % of CO_2 emissions within Austria. In order to achieve the goals set by the EU, the European steel industry is aiming for reductions of CO_2 emissions of around 80-95 % by 2050 compared to 1990 levels and is shifting its focus from current production routes towards hydrogen-based steelmaking.

The primary focus of the thesis lies in designing a setup for a cold model for simulating fluidization behavior of mixtures containing iron ore and silica sand in a pressurized vessel designed for iron ore fines reduction with hydrogen. Due to its similar fluid dynamic properties, in particular density wise, helium is chosen as the fluidization gas, while comparative experiments with air are conducted as well. To establish the particle diameter needed to calculate the theoretical minimum fluidization velocity, the particle distributions of iron ore, silica sand and the ten sample mixtures were determined. Additionally, the study evaluates the impact of an internal cyclone by comparing experiments with and without it, documenting bed material losses. The cold model experiments were documented through pressure measurements and assessed by deducing the experimental minimum fluidization velocity. Subsequently, the experimental values were compared with the theoretically derived ones.

In summary, the investigation revealed that an increase in the proportion of iron ore results in a decreased minimum fluidization velocity, attributed to a higher fraction of particles with a smaller diameter. Specifically, for mixtures of fine iron ore with 0.063-0.125 mm diameter, test runs using helium as the fluidization gas exhibited lower minimum fluidization velocities compared to those with air. This phenomenon can be attributed to the predominant influence of dynamic viscosity on the fluidization velocity for smaller particle diameters, rather than fluid density. The opposite was observed for samples mixtures of coarser iron ore of 0.5-1mm diameter, where test runs with helium resulted in higher fluidization velocities than with air. At larger particle diameters, the density shows a more significant impact on the fluidization velocity compared to dynamic viscosity. The cyclone plays a decisive role, particularly for samples with an increased proportion of fine iron ore and quartz sand particles. The losses of the fine ore amount to up to 20 %, which leads to the conclusion that the cyclone design must be improved.

Kurzfassung

Die Stahlindustrie verursacht jährlich ca. 2,8 Gigatonnen CO_2, was 8 % der Gesamtemissionen des Energiesystems ausmacht. Der österreichische Stahlsektor ist für bis zu 15 % der CO_2-Emissionen innerhalb Österreich verantwortlich. Um die von der EU gesetzten Ziele zu erreichen, strebt die europäische Stahlindustrie bis 2050 eine Reduktion der CO_2-Emissionen um 80-95 % im Vergleich zu 1990 an und verlagert ihren Schwerpunkt von den derzeitigen Produktionsrouten auf die wasserstoffbasierte Stahlerzeugung.

Das Hauptaugenmerk dieser Arbeit liegt auf dem Aufbau eines Kaltmodells zur Simulation des Fluidisierungsverhaltens von eisenerz- und quarzsandhaltigen Gemischen in einem Druckbehälter, der für die Eisenerzfeinreduktion mit Wasserstoff ausgelegt ist. Aufgrund seiner ähnlichen fluiddynamischen Eigenschaften, insbesondere in Bezug auf die Dichte, wird Helium als Fluidisierungsgas gewählt, wobei auch Vergleichsexperimente mit Luft durchgeführt werden. Zur Ermittlung des Partikeldurchmessers, der für die Berechnung der theoretischen Lockerungsgeschwindigkeit erforderlich ist, wurden die Partikelverteilungen von Eisenerz, Quarzsand und der zehn Probenmischungen bestimmt. Darüber hinaus wird in der Studie der Einfluss eines internen Zyklons durch den Vergleich von Versuchen mit und ohne Zyklon bewertet und der Verlust von Bettmaterial dokumentiert. Die Kaltmodellversuche wurden durch Bestimmung der Lockerungsgeschwindigkeit bewertet. Anschließend wurden die experimentellen Werte mit den theoretisch abgeleiteten Werten verglichen.

Zusammenfassend ergab die Untersuchung, dass eine Erhöhung des Eisenerzanteils zu einer Verringerung der Lockerungssgeschwindigkeit führt, was auf einen höheren Anteil von Partikeln mit einem kleineren Durchmesser zurückzuführen ist. Besonders bei Mischungen von Quarzsand mit feinem Eisenerz (0,063-0,125 mm) zeigten Tests mit Helium als Fluidisierungsgas niedrigere Mindestfluidisierungsgeschwindigkeiten im Vergleich zu Luft. Dies liegt daran, dass bei kleineren Partikeldurchmessern die dynamische Viskosität den größten Einfluss auf die Lockerungsgeschwindigkeit hat, im Gegensatz zur Fluiddichte. Das Gegenteil wurde für Gemische mit gröberem Eisenerz (0,5-1 mm) beobachtet, wo die Dichte bei größeren Partikeldurchmessern die Lockerungsgeschwindigkeit stärker beeinflusst als die dynamische Viskosität. Der Zyklon spielt besonders für Proben mit erhöhtem Anteil an feinen Eisenerz- und Quarzsandpartikeln eine entscheidende Rolle. Die Verluste des Feinerzes belaufen sich dabei auf bis zu 20 %, woraus die Erkenntnis schließt, dass das Zyklondesign verbessert werden muss.

Table of Contents

1 Introduction 1

1.1 Motivation 1

1.2 Aim 1

2 Theoretical background and state of the art 3

2.1 Fluidized bed technology 3

2.1.1 Classification of Fluidization by Flow Regimes 3

2.1.2 Advantages and Disadvantages of Gas Fluidization 5

2.1.3 Variables effecting the Quality of Fluidization 6

2.2 Fundamentals of Iron Ore Reduction 16

2.2.1 Fundamentals of Iron Oxides 16

2.2.2 Iron Ore Production 17

2.2.3 Iron Ore Reduction – Chemical Reactions 18

2.2.4 Steelmaking Processes – Direct vs Indirect Reduction 21

2.3 Fluidized Bed Scale-Up using Scaling Parameters (Similarity Theory) 31

2.4 Reh and Grace Diagram 34

2.5 Similar Research – State of the Art 37

2.5.1 Cold Model Experiments with Helium at TU Wien 37

2.5.2 Fluidized Bed Reactor at TU Wien 38

3 Experimental 40

3.1 Experimental Setup 40

3.2 Test Matrix 43

3.3 Test Procedure 43

3.4 Sample Analysis 44

3.5 Fluidization Gas 44

3.5.1 Temperature Dependence of Density 44

3.5.2 Temperature Dependence of Kinematic Viscosity 46

3.5.3 Temperature Dependence of Ar and U_{mf} 46

3.6 Similarity of Helium and Hydrogen 48

4 Results 51

4.1 Validation of Experimental Setup 51

4.2 Calibration of Rotameter with a Gas Meter 54
4.2.1 Air 54
4.2.2 Helium 55
4.3 Particle Distribution Curves (Sieve Analysis) 55
4.3.1 Particle Distribution of Silica Sand 55
4.3.2 Particle Distribution of Iron Ore 58
4.3.3 Particle Distribution of Sample Mixtures 60
4.4 Geldart Diagram 62
4.5 Reh and Grace Diagram – Sample Mixtures 63
4.6 Cold Model Experiments 65
4.6.1 Calculation of Theoretical Minimal Fluidization Velocity and Theoretical Pressure Loss 65
4.6.2 Influence of Sieve on Pressure Loss 66
4.7 Comparison of Theoretical and Experimental Results 77
4.7.1 Comparison of Sample Mixtures 77
4.7.2 Comparison of Cold Model Experiments with Air vs Helium 78
4.7.3 Influence of the Presence of a Cyclone on the Cold Model Experiments 86
5 Conclusion 89
6 Bibliography 92
Symbols 97
List of tables 100
List of figures 102
Appendix 106

1 Introduction

1.1 Motivation

Major environmental consequences are caused by the enhanced greenhouse effect resulting primarily from fossil fuel burning, which play an important role in specific steelmaking routes. The steel industry is responsible for approximately 2.8 gigatonnes of CO_2 emissions annually, constituting 8 % of the total emissions from the energy system. In Austria, the steel industry is responsible for up to 15 % of the total CO_2 emissions. Given the indispensable role of steel in modern economies and advancing technologies, a significant surge in steel demand is anticipated in the coming years. This rise is closely tied to factors like population growth, GDP expansion, and overall industrialization. Especially for energy transition and decarbonisation steps, steel will play a crucial role in the renewables sector as well due to its application in the production of wind turbines, solar panels, geothermal plants and electric vehicles to name a few.[1], [2], [3], [4]

CO_2 emissions and energy utilization in European steel production have undergone a 50 % reduction since 1960. The industry is now targeting additional cuts of 80-95 % by 2050 compared to 1990 levels. Given the carbon-intensive nature of the conventional Blast Furnace - Basic Oxygen Furnace production route, typically yielding a carbon footprint of 1.6-2.0 tonnes of CO_2 per tonne of crude steel, and with most EU steel mills already operating at optimal efficiency, the focus is increasingly shifting towards hydrogen-based steelmaking as a key measure for sectoral decarbonization. 30 % of the primary steel production within the EU is anticipated to undergo decarbonisation by 2030 through the utilization of renewable hydrogen.[5]

Due to their enhanced mass and heat transfer qualities, fluidized beds are ideal for the reduction of iron ore. Established reduction processes such as Finmet, Circofer and Circored have already applied the fluidized bed technology. A major advantage is the ability to reduce iron ore fines without the need for additional agglomeration steps, which contribute to increased production costs.

1.2 Aim

The aim of this work is to investigate and evaluate the fluidization behaviour of mixtures of iron ore and quartz sand in a cold model. In this context, a test rig for the existing cold model

with flow meter, pipelines and pressure gauges is developed and constructed. An additional task is to determine whether the built-in cyclone in the cold model is suitable or not. Furthermore, the similarities of helium and hydrogen as fluidizing gases will be demonstrated and theoretically investigated by applying Glickman's similarity rules. In addition, experiments with air will also be carried out to enable a comparison.

2 Theoretical background and state of the art

A brief overview of the fundamentals of fluidized bed technology and iron ore production will be given in this section, providing some insights into influencing parameters of fluidization and comparing iron oxide production routes. In addition, the determination of the similarity theory scaling parameters and the application of dimensionless numbers in state diagrams Reh and Grace will be presented.

2.1 Fluidized bed technology

Fluidization engineering makes use of several unique aspects of this contacting technique. Although there are numerous alternative configurations imaginable, the fluid is typically a gas that is blasted upward by a blower or compressor through a perforated flat plate or a succession of orifices. [6], [7]

2.1.1 Classification of Fluidization by Flow Regimes

The state of fluidization differs depending on fluid velocity. For instance, a fluid simply moving slowly upward through a bed of small particles by traveling through the void spaces between stationary particles is referred to as a fixed bed. As the fluid´s flowrate rises, particles disperse and some vibrate and move in constrained areas, this phenomenon is called an expanded bed.

Once the velocity reaches what is known as the minimum fluidization velocity, a threshold is attained where every particle is merely upheld by the ascending flow of the fluid. At this equilibrium point, the gravitational forces acting on the particles are exactly offset by the frictional forces between particles and fluid. This state is recognized as the starting point of fluidization, commonly referred to as an incipiently fluidized bed or a bed operating at minimum fluidization conditions.

When further increasing the fluid velocity in liquid – solid systems above minimum fluidization velocity, the bed is uniformly expanded, whereby any significant flow disruptions are mitigated and remain minimal. This state is referred to as a homogenously fluidized bed. In contrast, such beds in gas – solid systems are only possible for the combination of very fine particles and highly dense gases at high pressures. In the following chapters, the focus will be set on gas fluidization, as it is this thesis' main topic.

Rising gas flow rates lead to the formation of bubbles and gas channels, while also inciting a

vigorous movement of the particles. As a result, the bed height rises beyond the one established at minimum fluidization velocity. The corresponding fluidization state is called heterogeneous fluidized bed or bubbling fluidized bed.

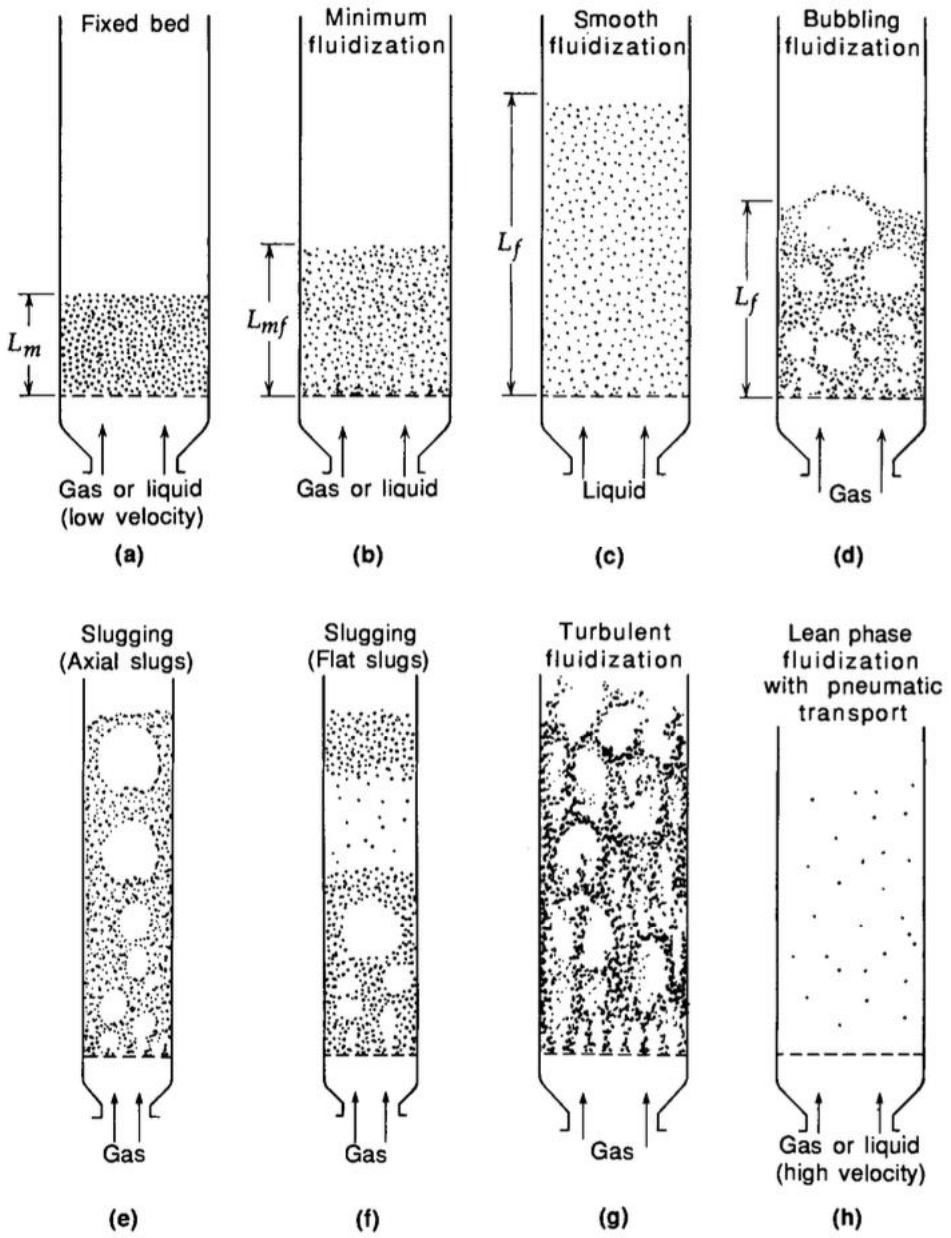

Figure 1: Types of fluidization [6]

As the gas velocity rises even further in fluidized beds with smaller diameters, bubble coalescence increases throughout their ascent, leading to the formation of larger bubbles. The existence of the column wall has a significant impact on the shape and rising speed of these bubbles, especially when the bubble's volume-equivalent diameter is greater than roughly 0.1 times the column diameter. Bubbles can elongate and change into gas slugs when they get close to the column diameter, for instance, when the ratio of the bubble's equivalent diameter to the

column diameter is exceeded by 0.6. This transition marks a shift from a bubbling pattern to a slugging form of fluidization. Fine particles just flow down by the wall around the gas slugs, while coarse particles are pushed upwards by the slugs, causing the particles to only fall, once the slug disintegrates. However, simultaneously, another slug takes shape, and the particles are pushed back up, resulting in an unstable motion.

Fine particles, which are subjected to sufficiently high gas flow rates, surpass their terminal velocity, resulting in the vanishing of the upper surface of the bed and entrainment. The terminal velocity is defined as the velocity, at which, when exceeded, the particles are carried out of the bed. This state, which is called turbulent fluidized bed, is characterized by the turbulent motion of solid clusters and gas voids of different shapes and sizes.

At high velocities above the terminal velocity, the fluidization state called pneumatic (hydraulic) transport is reached. The entrained particles must be returned to the bed by the means of a cyclone to assure steady state conditions, if steady state operation is to be assumed.[6], [7]

2.1.2 Advantages and Disadvantages of Gas Fluidization

Fluidized bed reactors offer a multitude of advantages that make them a versatile choice for various industrial processes. One key benefit is their exceptional temperature uniformity due to favourable gas – solid contacting, with variations rarely exceeding 10 °C within the dense bed, effectively eliminating troublesome "hot spots." Furthermore, fluidized beds exhibit remarkable bed-to-surface heat transfer coefficients, typically surpassing those found in fixed beds by an order of magnitude and outperforming empty columns by two orders of magnitude. Additionally, fluidized beds maintain relatively low pressure drops, only necessitating enough support for the bed's weight per unit cross-sectional area. Their scalability to considerable sizes, including commercial reactors spanning hundreds of square meters, underscores their industrial viability. Fluidized beds allow for good turndown capability, accommodating wide variations in gas flow rates, typically by a factor of 2-3. The capacity of fluidized beds to handle a wide range of particle sizes—often with a ratio of upper to lower decile particle diameter (d_{p90}/d_{p10}) of 10:20—allows them to be flexible for a variety of industrial applications. [7]

Fluidized beds are known for their substantial vertical (axial) gas mixing, which arises as gas is pulled downward by descending particles. This phenomenon introduces considerable "backmixing" and leads to significant deviations from plug flow, often characterized by axial

Peclet numbers in the range of 5 to 10. Additionally, vigorous motion of particles and their clusters results in substantial axial dispersion and backmixing of solids. In continuous processes, this means that some particles spend very little time within the bed, while others linger much longer than the mean residence time, causing variations in material flow. Moreover, fluidized beds may experience gas bypassing, especially when rising bubbles move through the bed more swiftly with limited interaction with solid particles compared to denser gas phases, which enable better gas – solid contacting. Particles of distinctive geometries, such as needle or flat disc shapes, or those smaller than approximately 30 µm in mean diameter can be difficult or even impossible to fluidize effectively. Additionally, entrainment poses a challenge as fine particles can be carried upward by exhaust or product gases, necessitating continuous feedback /recirculation to minimize losses. Additionally, fluidized bed particles may experience attrition, breakage, or abrasion as a result of their interactions with one another and fixed surfaces, which could result in problems with particle integrity. In comparison to fixed bed reactors, fluidized beds are noted for their complexity, which presents difficulties in their design, operation, and modelling. The likelihood of operational issues rises as a result of complexity. [7]

2.1.3 Variables effecting the Quality of Fluidization

This chapter aims to identify the fundamental particle and fluid attributes that have a significant impact on the fluidization of particles and play an important role in determining the characteristics of fluidized beds. When assessing the advantages of incorporating fluidization into a particular process and throughout the phases of designing, operating, and modelling fluidized bed processes, it is crucial to thoroughly analyze these characteristics and assess their potential significance. In this section, the four Geldart powder groups will be presented. Furthermore, this chapter delves into diverse approaches for quantifying and predicting the minimum fluidization velocity, a parameter that holds substantial implications for the behaviour of fluidized beds.

2.1.3.1 Particle Properties

2.1.3.1.1 Geldart Characterization of Particles

Geldart [8] introduced a widely accepted and valuable classification system that categorises particulate materials into four distinct powder categories based on their collective gas fluidization characteristics, as see in Figure 2.

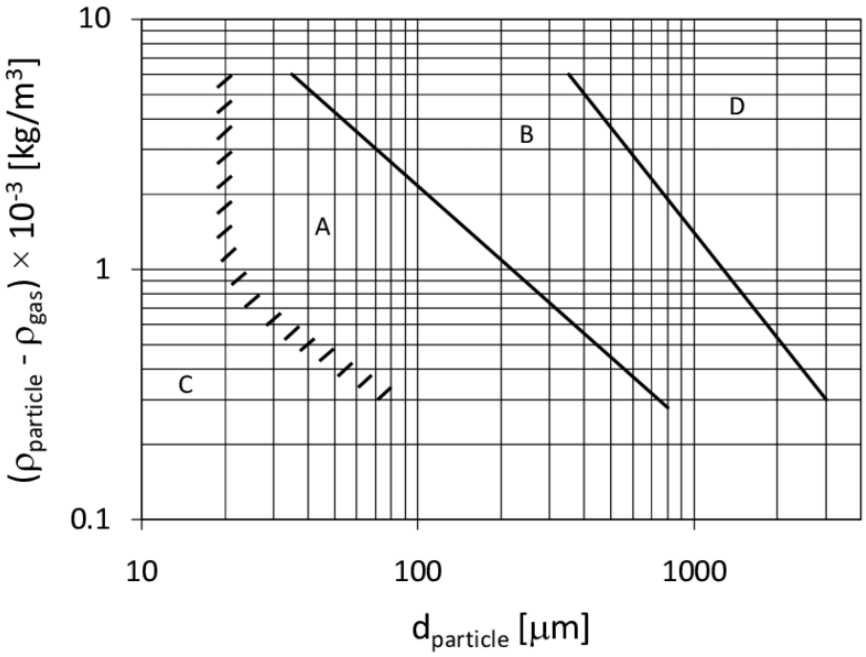

Figure 2: Geldart Characteristics of Particles [9]

Group A (aeratable): Typical Group A powders are materials with a small mean size and/or a low particle density (<1.4 g/cm^3). The powders within this particular group exhibit significant expansion prior to the onset of bubbling, which starts at the minimum bubbling velocity. When the gas supply is abruptly halted, the bed undergoes a gradual collapse. This behaviour is akin to gross circulation of the powder, and it is observed even when there are few bubbles present, facilitating rapid mixing. Cohesive forces are negligibly low. These powders fluidize well, which is also why they are, for instance, used for fluid catalytic cracking.

Group B (bubble readily): Group B consists of materials in the mean size and density ranges 40 µm< d_{SV} < 500 µm, 4 g/cm^3 > ρ_S > 1.4 g/cm^3, sand being the most typical powder. In contrast to powders belonging to group A, the formation of bubbles in this particular type of powder occurs naturally at or slightly above the minimum fluidization velocity. The growth of the bed is minimal, and its collapse occurs swiftly upon the halt of gas flow. In the absence of bubbles, the circulation of powder is minimal or nonexistent, and when bubbles do form, they break individually at the surface of the bed. Interparticle forces are negligible.

Group C (cohesive): Group C powders are primarily influenced by cohesive forces between particles, which worsen fluidization. The interparticle forces are greater than the forces being applied to the particle by the fluid causing the powders to lift as a cohesive mass and thereby creating undesirable fissures or gaps through which gas flows. Typically, this results from very small particle sizes, strong electrostatic charges, or the presence of highly moist or adhesive

materials within the bed. Consequently, particle mixing and heat transfer between a surface and the bed are significantly poorer compared to powders belonging to Groups A or B. To enable or enhance fluidization, mechanical stirrers or vibrators are employed to disrupt these stable channels. A typical example for a Group C material is flour.

Group D: Group D consists of larger particles and/or dense particles that cannot be fluidized as easily as particles from Group A or B. As gas enters the base and exits from the top of bubbles, it causes all bubbles except the largest ones to ascend at a slower rate than the fluidizing gas. This creates a distinct pattern of gas exchange and bypassi ng, different from what is observed in the case of group A or B powders. The regime found in this specific group of powders is mostly turbulent, which could result in some particle attrition and the rapid removal of produced fines. Given the limited interactions between particles and the high particle momentum, the fluidization of relatively sticky materials becomes possible. Examples for Group D materials are cereal grains and peas. [7], [8]

2.1.3.1.2 Particle Size and Shape

The particle size plays a crucial role in fluidization processes. Typically, this size is quantified as a diameter, often determined through sieve (screening) analysis. Additionally, various sphere-equivalent diameters, such as the volume-equivalent diameter (representing the diameter of a sphere with the same volume as the particle), are commonly used. Among these equivalent diameters, the most suitable average for fluidization is the Sauter mean [7]:

$$d_{SV} = \frac{6 \cdot V_p}{S_p} \tag{2.1}$$

Since the fixed bed consists of particles of various sizes, a mean particle diameter ($\overline{d_p}$) must be calculated as representative value for the mixture of particles and is given by Equation 2.2. In order to determine the average diameter (d_p) and the mass share (y) of each class i, a sieve analysis needs to be conducted. Sieve analysis is a method employed to ascertain the distribution of particle sizes within a solid substance. This is achieved by measuring the quantity of powder that is captured by a set of sieves, each equipped with apertures of varying sizes. A particle size distribution curve is produced using the results from the sieve analysis. This curve, which is frequently represented as a histogram or cumulative distribution curve, displays the percentage of material that falls into certain size ranges.[6]

$$\overline{d_p} = \frac{1}{\sum_i \left(\frac{y}{d_p}\right)_i} \tag{2.2}$$

However, in most calculations, the Sauter mean is used, which is why an approximate relationship between Sauter mean and mean particle diameter with the use of a shape factor called sphericity (Φ) is established, which expresses the deviation from a perfectly spherical particle and is determined by Equation 2.3. The relation between equivalent diameter and mean particle diameter is given by Equation 2.4.

$$\Phi = \left(\frac{surface\ of\ sphere}{surface\ of\ particle}\right)_{of\ same\ volume} \tag{2.3}$$

$$d_{SV} = \Phi \cdot \overline{d_p} \tag{2.4}$$

A perfectly spherical particle has a sphericity of 1 and decreases in value as the shape deviates further from that of a sphere.[7]

2.1.3.1.3 Particle Density and Internal Porosity

In the case of nonporous particles, the particle density ρ_p is equal to the density of the material of which the particle is comprised and is referred to as the hydrodynamic particle density and can be calculated by the following equation:.

$$\rho_P = \frac{m_P}{V_P} \tag{2.5}$$

For the determination of density of porous materials, the fraction of pores, called porosity, is subtracted from the material density.

$$\rho_{P,porous} = \rho_{bulk} = \frac{m_P}{V_P - V_{Pores}} = \rho_P \cdot (1 - \varepsilon) \tag{2.6}$$

For fluidization purposes, the particle density is better described by the hydrodynamic particle density and is therefore used in the calculation concerning the minimum fluidization velocity.[7][10]

For mixtures of sand and iron ore, the theoretical density must be considered:

$$\rho_{p,theoret} = y_{Sand} \cdot \rho_{Sand} + y_{Iron\ Ore} \cdot \rho_{Iron\ Ore} \tag{2.7}$$

2.1.3.2 Fluid Properties

2.1.3.2.1 Gas Density

Earlier and more robust fluidization is achieved when the resistance on particles is heightened by elevated gas density. Gas density rises as pressure increases and declines with higher temperatures. In assessing the impact of temperature and pressure on gas-fluidized beds, ideal gas behaviour is typically a satisfactory approximation. [7]

In order to calculate the gas density, the ideal gas law can be applied[11]:

$$\rho_g = \frac{p}{Z \cdot R \cdot T} \tag{2.8}$$

2.1.3.2.2 Gas Viscosity

Increased gas viscosity generates greater resistance for small particles, while its influence is relatively minor for larger particles, such as those in the Geldart D category. While largely steady across pressure fluctuations, gas viscosity rises with temperature.[7]

A formula for the calculation of the gas viscosity and its constants is given by[11]:

$$\mu = A + B \cdot T + C \cdot T^2 + D \cdot T^3 + E \cdot T^4 \tag{2.9}$$

2.1.3.3 Fluidization Parameters

2.1.3.3.1 Minimum Fluidization Velocity

The minimum fluidization velocity U_{mf} is forecasted by applying the principle that achieving minimum fluidization demands a balance between the weight of the particles minus the buoyancy and the drag exerted by the fluid when transitioning from packed bed flow to fluidization.

$$\frac{\Delta p}{H} = 150 \cdot \frac{\left(1-\varepsilon_{mf}\right)^2}{{\varepsilon_{mf}}^3} \cdot \frac{\mu \cdot U_{mf}}{d_{SV}^2} + 1.75 \cdot \frac{\left(1-\varepsilon_{mf}\right)}{{\varepsilon_{mf}}^3} \cdot \frac{\rho_g \cdot {U_{mf}}^2}{d_{SV}} \tag{2.10}$$

$$\frac{\Delta p}{H} = (1-\varepsilon) \cdot \left(\rho_p - \rho_g\right) \cdot g \tag{2.11}$$

The drag on a fixed bed rises with an increase in pressure drop. Consequently, U_{mf} is anticipated by pinpointing which pressure drop across a stationary bed equals the buoyant weight of the bed per unit cross-sectional area. Simplified this means finding velocity at which the pressure drop for fixed (Ergun equation) and fluidized bed is equal by equating Equation (2.10) and Equation (2.11), which results in a quadratic equation (Equation 2.12). [7]

$$U_{mf} = \frac{-\frac{150(1-\varepsilon_{mf})}{\varepsilon_{mf}^{3}\Phi_s^{2}} \cdot \frac{d_p\rho_g}{\mu}}{\frac{3{,}5}{\varepsilon_{mf}^{3}\Phi_s} \cdot \left(\frac{d_p\rho_g}{\mu}\right)^2} + \frac{\sqrt{\left(\frac{150(1-\varepsilon_{mf})}{\varepsilon_{mf}^{3}\Phi_s^{2}} \cdot \frac{d_p\rho_g}{\mu}\right)^2 - 4 \cdot \frac{1{,}75}{\varepsilon_{mf}^{3}\Phi_s} \cdot \left(\frac{d_p\rho_g}{\mu}\right)^2 \cdot \left(-\frac{\rho_g \cdot g \cdot (\rho_p - \rho_g) \cdot d_{SV}^3}{\mu^2}\right)}}{\frac{3{,}5}{\varepsilon_{mf}^{3}\Phi_s} \cdot \left(\frac{d_p\rho_g}{\mu}\right)^2} \tag{2.12}$$

Wen and Yu [12] derived the following commonly used equation for U_{mf} after some approximations including the sphericity and void fraction for simplicity purposes, resulting in approximations for the Reynolds number (Re) as follows:

$$U_{mf} = \frac{\mu}{\rho_g \cdot d_{SV}} \cdot Re \tag{2.13}$$

$$Re = \left[\sqrt{\{33.7^2 + 0.0408 \cdot Ar\}} - 33.7\right] \tag{2.14}$$

The Archimedes number (Ar) which represents the ratio of gravity to viscous forces and is calculated with the following equation:

$$Ar = \frac{\rho_g \cdot g \cdot (\rho_p - \rho_g) \cdot d_{SV}^3}{\mu^2} \tag{2.15}$$

Both gas-fluidized and liquid-fluidized beds can be described by equations (2.10) and (2.11). For liquid-solid fluidization as well as for gas-solid fluidization involving Geldart group B and D particles, predictions derived from this relationship typically exhibit a fairly high degree of accuracy, typically within about 20% (as discussed in Section 2.7). Prediction accuracy for Geldart group A powders, on the other hand, is normally within 40%. Van der Waals and other interparticle forces, which are not taken into account in the variables used to formulate Eq.

(2.11), play a significant role in the behaviour of group A particles but have secondary effects on the behaviour of group B and group D solids, which is the cause of the accuracy discrepancy.[7]

There are numerous other correlations for the Reynolds number, depending on the particle density and the particle diameter of the species. For comparison purposes, three other correlations are used to calculate the minimum fluidization velocity, whereby the correlations were chosen according to particle diameter and particle density of the species used for the cold model experiments. [13]The correlations are as follows:

Bourgeis and Grenier for 86 µm<d_p<25000 µm and 1200 kg/m^3<ρ_p< 19300 kg/m^3: [14]

$$Re = \left[\sqrt{25.46^2 + 0.0382 \cdot Ar\}} - 25.46\right] \quad (2.16)$$

Vaid and Sen Gupta for 114µm<d_p<1829µm and 1669 kg/m^3<ρ_p< 4332 kg/m^3: [15]

$$Re = \left[\sqrt{224^2 + 0.0546 \cdot Ar\}} - 24\right] \quad (2.17)$$

Bin for 40 µm<d_p<2129 µm and 1600 kg/m^3<ρ_p< 7500kg/m^3: [16]

$$Re = \left[\sqrt{27.31^2 + 0.0386 \cdot Ar\}} - 27.31\right] \quad (2.18)$$

Baeyens and Geldart for 50µm<d_p<4000 µm and 850kg/m^3<ρ_p< 8810 kg/m^3: [17]

$$Re = \left[\sqrt{27.31^2 + 0.0386 \cdot Ar\}} - 27.31\right] \quad (2.19)$$

2.1.3.3.2 Terminal Velocity

The terminal velocity is the velocity at which the particles are carried out of the fluidized bed.

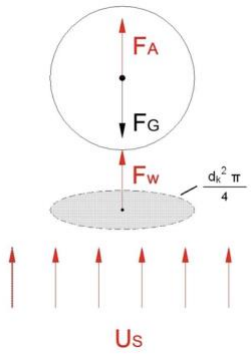

Figure 3: Acting forces on spherical particle[10]

To determine the terminal velocity, one must consider the forces acting on a spherical particle, as depicted in Figure 3. For one, gravitational forces push the particle down, while buoyancy forces drive the particle upwards. Additionally, drag forces are exerted on the particle by the fluidizing gas.

The equation of momentum equilibrium is given by the following equation:

$$\frac{\pi}{6} \cdot d_p^3 \cdot (\rho_p - \rho_g) \cdot g - C_W \cdot A_p \cdot \frac{\rho_g \cdot U_t^2}{2} = \frac{\pi}{6} \cdot d_p^3 \cdot \rho_p \cdot \frac{dU_t}{dt} \tag{2.20}$$

Assuming steady state, the terminal velocity is calculated with the following equation:

$$U_t = \sqrt{\frac{4}{3} \cdot \frac{\rho_p - \rho_g}{\rho_g} \cdot \frac{d_p \cdot g}{C_W}} \tag{2.21}$$

The drag coefficient C_W is defined as a function of the particle Reynolds Number (Re_p) and is determined according to the prevalent flow regime.

$$Re_p = \frac{\rho_g \cdot U_S \cdot d_p}{\mu} \tag{2.22}$$

For particles in the Stokes and Newton regime, the terminal velocity can be calculated numerically. However, an iterative solution or other numerical approximations are needed for the transition regime. [10]

Laminar regime $Re_p < 0.2$ (Stokes regime)

$$C_W = \frac{24}{Re_p} \quad \rightarrow \quad U_t = \frac{(\rho_p - \rho_g) \cdot {d_p}^2 \cdot g}{18 \cdot \mu} \tag{2.23}$$

Transition regime $0.2 < Re_p < 1000$ [16]

$$C_W = \frac{24}{Re_p} + \frac{4}{\sqrt{Re_p}} + 0.4 \quad \rightarrow \quad U_t = \sqrt{\frac{4}{3} \cdot \frac{\rho_p - \rho_g}{\rho_g} \cdot \frac{d_p \cdot g}{C_W}} \tag{2.24}$$

Turbulent regime $Re_p > 1000$ [17] (Newton regime)

$$C_W = 0.43 \quad \rightarrow \quad U_t = \sqrt{\frac{4}{3} \cdot \frac{\rho_p - \rho_g}{\rho_g} \cdot \frac{d_p \cdot g}{C_W}} \tag{2.25}$$

2.1.3.3.3 Pressure (Drop)

Pressure drop is experienced by the fluidizing gas as it flows through the bed of solid particles and is quantified as the difference between the inlet pressure and the outlet pressure of the fluidized bed. The decrease in pressure is mainly caused by frictional resistance between the particles and the fluid, especially when flowing through the void spaces between particles. Additionally, the size and shape of the particles influence the pressure reduction. To determine the minimum fluidization velocity, inlet and outlet pressure are measured, as well as the flowrate. The resulting function of pressure drop and superficial velocity of the fluidizing gas, is seen in Figure 4. Based on the fact, that pressure drop across a fluidized bed is constant, the minimum fluidization velocity can be easily estimated using Figure 4. [7], [18]

Gas velocity can exhibit local variations, especially in the gaps between the particles. Hence, it is valuable to employ the superficial gas velocity U as a reference value. The superficial gas velocity is defined as the ratio of the gas flowrate to the cross – sectional area and corresponds to the gas velocity that would be measured in case of an empty column. [7]

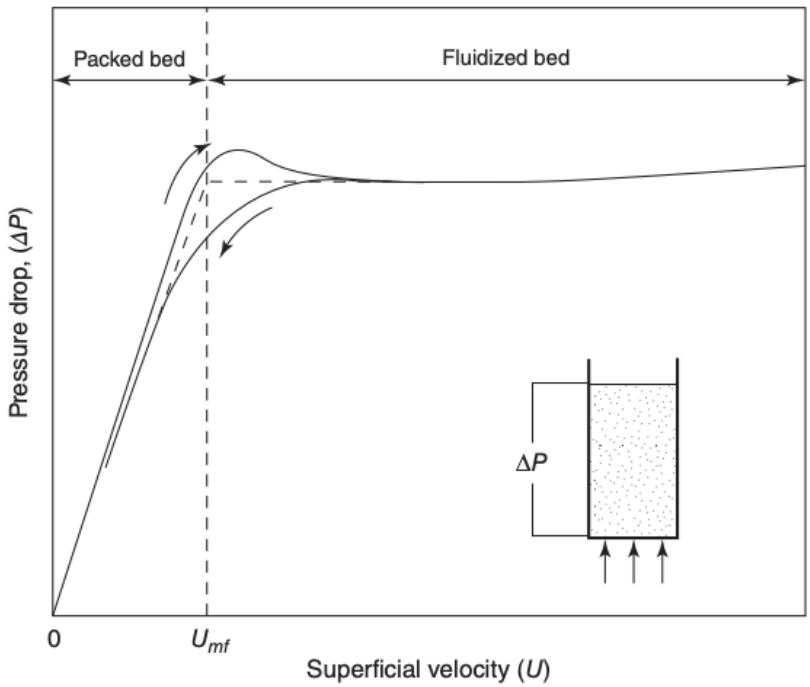

Figure 4: Pressure drop as a function of superficial velocity [7]

The pressure drop – velocity function can be divided into three different regimes. At lower superficial velocities, the pressure drop linearly increases with velocity, until reaching a maximum, which is slightly higher than the static pressure of the bed. With a slight increase in gas velocity, the particle packing starts “loosening” up, which translates into a higher void

fraction and in turn results in a pressure decrease to the static pressure of the bed. This initial pressure reduction observed over a fixed bed is primarily governed by the bed´s static characteristics such as bed height and particle size distribution.

The fixed bed regime is best described by the two following correlations, depending on the Reynolds number:

Carman – Kozeny correlation for Re < 1 (laminar regime): [18]

$$\frac{\Delta p}{H} = 180 \cdot \frac{(1-\varepsilon)^2}{\varepsilon^3} \cdot \frac{\mu \cdot U}{d_{SV}^3} \tag{2.26}$$

Ergun correlation for Re > 1 (turbulent regime): [7]

$$\frac{\Delta p}{H} = 150 \cdot \frac{(1-\varepsilon)^2}{\varepsilon^3} \cdot \frac{\mu \cdot U}{d_{SV}^2} + 1.75 \cdot \frac{(1-\varepsilon)}{\varepsilon^3} \cdot \frac{\rho_g \cdot U^2}{d_{SV}} \tag{2.27}$$

In case of a wide size distribution of particles, the smaller particles are prone to sliding into the gaps between the larger particles, allowing them to become fluidized while the larger particles stay immobile, causing a state of partial fluidization. To pinpoint U_{mf} of a mixed particle system a tangent must be placed on the fixed bed curve, as depicted in Figure 5. The tangent represents the hysteresis of the pressure drop curve in the case of a mixture of predominant large particles (d_p>1 mm), caused by the particles' segregation. The intersection of the tangent with the fluidized bed´s constant pressure drop equals the point of minimum fluidization velocity. [6], [7]

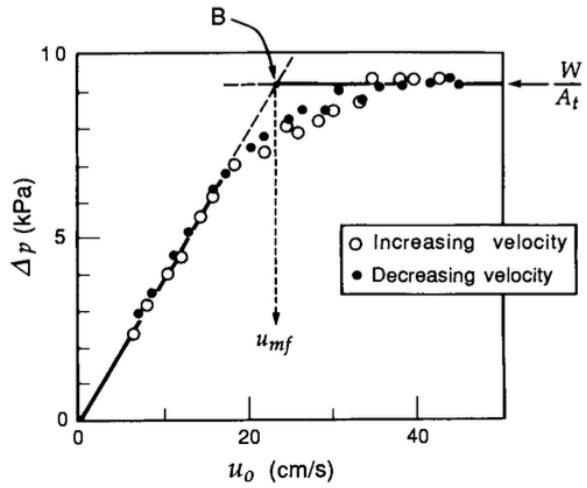

Figure 5: Pressure drop as a function of superficial velocity for a wide size distribution of particles [6]

As mentioned before, the pressure drop over the fluidized bed regime is constant and is given

by [7]:

$$\Delta p = (1 - \varepsilon) \cdot \left(\rho_p - \rho_g\right) \cdot g \cdot H \tag{2.28}$$

When surpassing U_{mf}, the particles are carried out of the fluidized bed, marking the beginning of the third and last regime referred to as pneumatic transport. In the case of recirculation of the particles, the pressure drop continuously increases, whereas the pressure decreases, when no feedback of the particles takes place, due to the reduction of the bed mass.[10]

2.1.3.3.4 Temperature and Pressure

Temperature and pressure of the fluidizing gas influence the fluid properties, which in turn impact the minimum fluidization velocity. With an increase in temperature, the fluid´s density decreases, while its viscosity rises, both resulting in a reduction in the minimum fluidization velocity. When pressure is elevated, the fluid´s viscosity shows almost no signs of change, whereas the density increases, leading to a slightly lower minimum fluidization velocity. [13], [19]

Other factors such as moisture leads to an increase in U_{mf} due to capillary forces between the particles. In multicomponent mixtures consisting of particles with significantly varying characteristics such as size the chances of their segregation are high, potentially even leading to their division into two distinct layers, each having its own U_{mf}. As a result, the smaller or less dense material is fluidized on top of the bigger or denser species of particles during a specific time window. [7]

2.2 Fundamentals of Iron Ore Reduction

This chapter focusses on the production of iron ore, also giving an introduction into the chemical reactions. In addition, various processes for steelmaking, which are used nowadays, are presented, while comparing the different routes of direct and indirect reduction of iron oxides.

2.2.1 Fundamentals of Iron Oxides

Iron is typically found in nature in the +2 and +3 oxidation states and is rarely encountered in its metallic form, except in meteorites. Among the prevalent minerals present in commercially valuable iron ores are magnetite (Fe_3O4), hematite (Fe_2O_3), goethite (FeO(OH)), and siderite ($FeCO_3$). The two primary minerals utilised to produce metallic iron are magnetite and

hematite.[20]

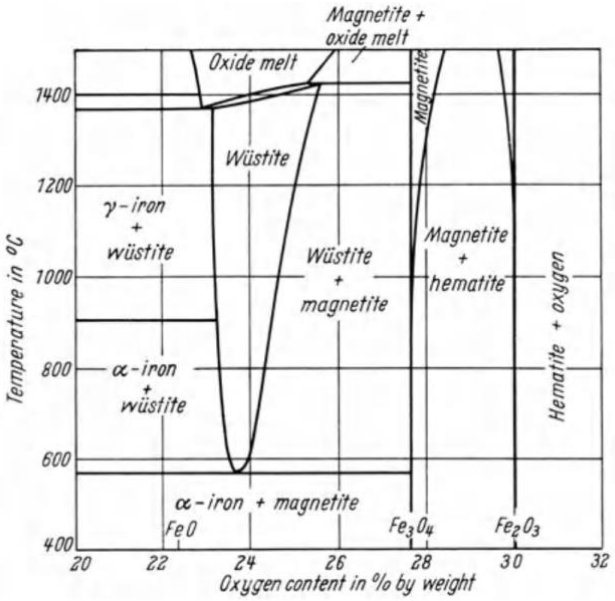

Figure 6: Fe - O binary system [21]

A portion of the binary Fe-O system is shown in Figure 6. The oxide with the most oxygen is hematite, which is then followed by magnetite and wüstite. Only at temperatures above 570 °C does wüstite become stable. It breaks down to Fe_3O_4 and Fe below 570 °C. Wüstite's stability region widens as temperature rises due to the lack of occupancy in the lattice by iron ions. Consequently, wüstite's chemical formula is $Fe_{(1-x)}O$ rather than FeO, where (1-x) stands for vacancies in the iron lattice.[22]

2.2.2 Iron Ore Production

Like many other metals, iron tends to build up in particular geological formations, creating a variety of economically feasible ore deposits. Iron concentrations in raw iron ore fall within the range of 25% to 67%. As the economic threshold for ironmaking usually lies in the low 60s and beyond, the majority of ores necessitate physical beneficiation processes (involving liberation and separation) to produce a usable concentrate.

Crushing and grinding the iron ore to its liberation size, or the largest size at which individual gangue particles are separated from the iron minerals, is the first step in physical beneficiation. The number of necessary steps for crushing and grinding varies, contingent upon several factors like the extent of impurities and the ore's hardness. Along with phosphorus, sulphur, and manganese, the principal gangue mineral that needs to be separated is typically silica.

In the second step, the gangue must be removed from the iron-bearing phases after the iron ore

has been processed to its liberation size. Only a certain number of separation technologies are practical due to the small size of the individual particles following normal liberation processes. While magnetic separation is used for magnetite due to its magnetic properties, hematite is commonly separated by froth flotation. The flotation process is split up into three steps. Depending on the type of collector, either the iron oxide particles or the silica particles are made hydrophobic by their addition. The slurry is subsequently transferred into a flotation cell, where the frother enhances the formation of air bubbles, which are created by an impeller or an aerator. During collision with the bubbles, the hydrophobic particles adhere and form an aggregate of bubble and particles, whose density is smaller than the suspension´s, causing them to rise to the surface of the bath. The floated particles are finally extracted from the bath´s surface and the process is reiterated, in case the desired iron concentration is not attained. Magnetite is won by using a magnetic drum, which is passed by the slurry and collects the magnetic material.

Depending on the process followed by the physical beneficiation and the form of iron, agglomeration of iron ore might be necessary. In the case of fine ores, pelletization or sintering are two methods applied to make the material usable, unless the following iron ore reduction is to take place in a fluidized bed. The fluidized bed technology was particularly designed for the direct use of fine iron ore.

Water and a binder are added to fine iron ore enabling the adhesion of both to form pellets. To ensure the needed durability for storage and transportation purposes, the pellets are dried and exposed to temperature of up to 1200 – 1300 °C. During the sintering process, the material is subjected to high temperatures and oxidized in the presence of coke, softening and causing bonding of the particles. [20]

2.2.3 Iron Ore Reduction – Chemical Reactions

The reduction of iron ore can be carried out with either a solid reducing agent, such as coke or coal, or a gaseous reducing agent like hydrogen and carbon monoxide. Since the thesis covers the topic of iron ore reduction in a fluidized bed, which entails the reaction with gaseous reducing agents, the focus on this chapter will be put onto the reduction of iron oxide with H_2 and CO.

Reduction with Carbon Monoxide:

The reduction of iron ore with carbon monoxide is divided into three steps. These steps and the reactions occurring at their boundaries are visually represented in Figure 7. The reaction

sequence, as well as the stability of each iron oxide phase depends on the reaction temperature. As depicted in Figure 7, the intermediate oxide phase $Fe_{(1-y)}$ is unstable at reduction temperatures below 570 °C, causing the decomposition of wüstite to metallic iron and magnetite. However, when reaction temperatures exceed 570 °C, the wüstite phase needs to be considered in the reduction. The stability of the iron oxide phases is also contingent on the quantity of carbon monoxide present in the CO/CO_2 mixture. [21]

The wüstite phase is denoted as Fe1 - y O in the graph, which arises due to iron vacancies within the crystal lattice during this phase. The parameter y in this context signifies the ratio of iron vacancies to the total available iron lattice sites.[21], [22]

The reaction sequence is defined as follows, considering the dependence on the reduction temperature (T):

$$3\,Fe_2O_3 + CO \rightarrow 2\,Fe_3O_4 + CO_2$$

For $T < 570\,°C$:

$$Fe_3O_4 + 4\,CO \rightarrow 3\,Fe + 4\,CO_2$$

For $T > 570\,°C$:

$$(1-y)\,Fe_3O_4 + (1-4y)\,CO \rightarrow 3\,Fe_{(1-y)}O + (1-4y)\,CO_2$$

$$Fe_{(1-y)}O + CO \rightarrow (1-y)\,Fe + CO_2$$

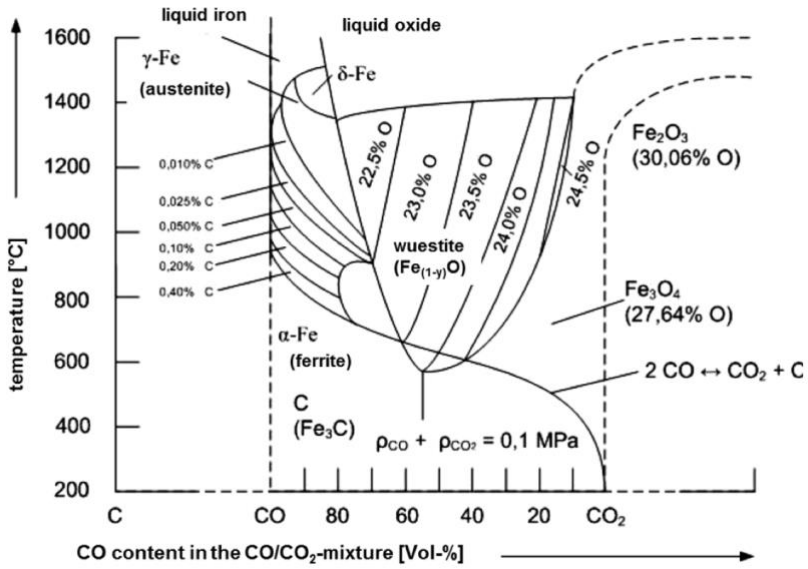

Figure 7: Baur - Glässner diagram for metallic iron, wüstite, magnetite, hematite and a CO_2/CO mixture [23]

The reaction´s direction, so either reduction or oxidation, depend on the partial pressure of oxygen within the oxide and the gas mixture. It is necessary to expose the oxide to a gas environment characterized by a lower oxygen partial pressure compared to that of the ore, otherwise oxidation would take place.

Reduction with Hydrogen:

As for the reduction of iron oxide with hydrogen as a reducing agent, the reduction sequence remains the same. The corresponding Baur – Glässner diagram, as seen in Figure 8, shows the same instability of wüstite at reduction temperatures under 570 °C as for the reduction with carbon monoxide. The reduction mechanism is as follows [21]:

$$3\,Fe_2O_3 + H_2 \rightarrow 2\,Fe_3O_4 + H_2O$$

For $T < 570\,°C$:

$$Fe_3O_4 + 4\,H_2 \rightarrow 3\,Fe + 4\,H_2O$$

For $T > 570\,°C$:

$$(1-y)\,Fe_3O_4 + (1-4y)\,H_2 \rightarrow 3\,Fe_{(1-y)}O + (1-4y)H_2O$$

$$Fe_{(1-y)}O + H_2 \rightarrow (1-y)\,Fe + H_2O$$

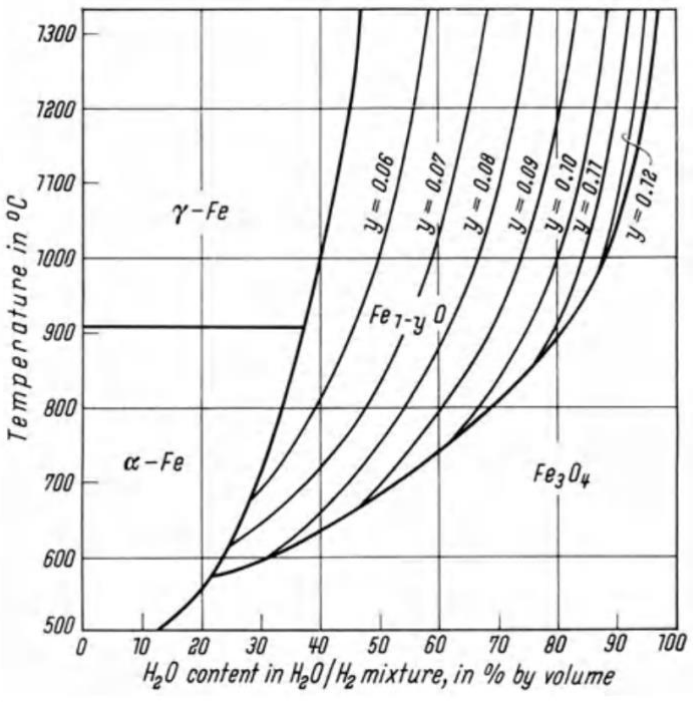

Figure 8:Baur - Glässner Diagram for metallic iron, wüstite, magnetite, hematite and a H2/H2O mixture [21]

In addition to the chemical aspect of the iron ore reduction, mass transfer mechanisms occur within the pores of the iron ore. Figure 9 provides a depiction of the reduction mechanism within a porous iron ore particle. The reduction gas fluidizes iron oxides, initiating the sequence with the mass transfer of gas species through the laminar layer of the iron oxide particles (1).

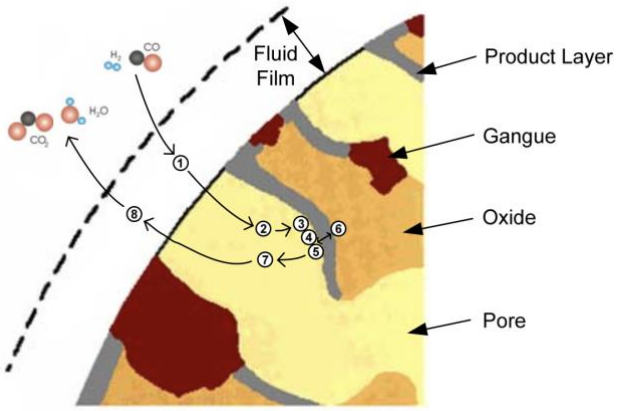

Figure 9: Reduction mechanism - mass transfer phenomena [24], [25]

Following this, once cracks, pores, and grain boundaries are filled through diffusion (2), gas molecules adhere to the surface of the oxide (3). Oxygen is extracted from the crystal´s surface during the phase boundary reaction (4), creating vacancies. These vacancies are subsequently balanced through solid-state diffusion (6), resulting in the nucleation and growth of solid product phases. The mechanisms for gaseous reaction products cover desorption (5), pore diffusion (7), and mass transfer through the laminar layer into the free gas stream (8). [26]

An increase in porosity and grain boundaries positively influence the diffusion step of the reduction mechanism. Other parameters, such as temperature, influence the rate – limiting step. While the chemical reaction limits reduction the most at lower temperatures, mass transfer mechanisms hinder the reduction speed at higher temperatures. [27]

2.2.4 Steelmaking Processes – Direct vs Indirect Reduction

In 2022, around 71.5 % of steel worldwide was produced via blast furnaces, while electric furnaces account for 28.2 % of the global steel production. [28]

Various process routes are employed in the production of steel, the primary distinctions being the nature of the input materials and the energy sources used, resulting in different process concepts. Four processes can be differentiated as follows [29] :

1. Blast furnace / Basic oxygen furnace
2. Electric arc furnace

3. Smelting reduction
4. Direct reduction

Figure 10 depicts the four steelmaking processes, showing all the input materials, including the various reducing agents. The following chapter will give an overview of the state – of the art steelmaking routes, while primarily focusing on the direct reduction using fluidized beds, as it is the main topic of this thesis.

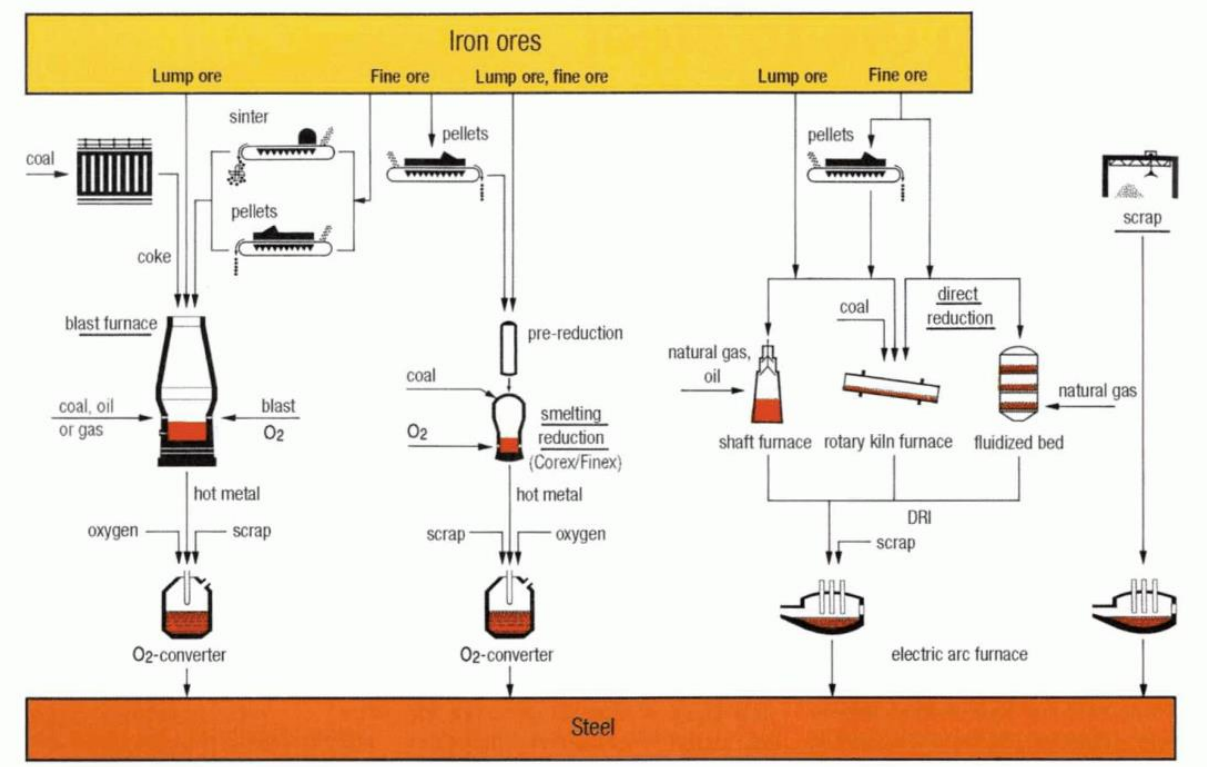

Figure 10: Crude steel production methods [30]

2.2.4.1 Blast Furnace

The reduction process in a blast furnace has been a fundamental method for iron and steel production for centuries, dating back to the first one in 1735. The primary raw materials employed in the blast furnace process are iron ore, coke (carbon), and limestone. Depending on the iron ore form, ranging from iron lumps to sinters and pellets, the raw material needs to be pre-treated. A mixture of the raw materials, referred to as a burden, is charged into the furnace from the top through a charging system, as seen in Figure 11. As the solid burden descends, it encounters a rising counterflow of hot reducing gas, which is blown into the furnace through nozzles. The ignition of coke in the lower section is initiated by the hot air blast. The coke functions as both a heat source and a reducing agent. The carbon undergoes a reaction with atmospheric oxygen, resulting in the formation of carbon monoxide (CO), a powerful reducing

gas[29], [30], [31]:

Combustion of coke:

$$C + O_2 \rightarrow CO_2$$

Boudard reaction (coke gasification):

$$C + CO_2 \rightarrow 2\,CO$$

The iron ore is then reduced by carbon monoxide in various steps, as described in 2.2.3:

$$Fe_2O_3 + 3\,CO \rightarrow 2\,Fe + 3\,CO_2$$

The increase in temperature of the burden, as it moves down the blast furnace, promotes the reduction reactions and slag formation. The reduced iron drips down to the bottom of the furnace, at first forming sponge iron and then finally accumulating as molten iron (hot metal). [29]

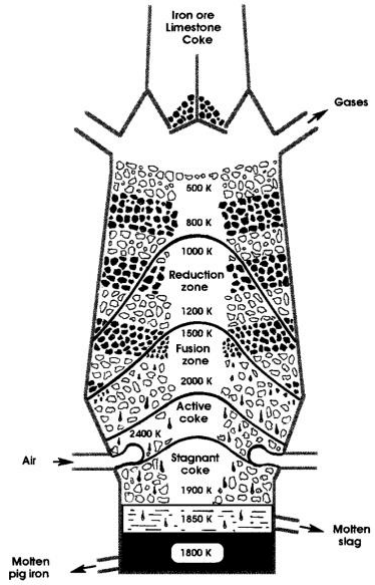

Figure 11: Blast furnace [31]

The limestone acts as a flux and converts sand and other impurities, forming a molten slag that floats on top of the molten iron due to its low density. The slag formation is given by[31]:

$$CaCO_3 \rightarrow CaO + CO_2$$

$$CaO + SiO_2 \rightarrow CaSiO_3$$

Periodically, the molten iron and slag are tapped from the furnace through separate openings.

The iron is directed into molds to form pig iron or further processed into steel, while the slag is discarded or used in various applications. Blast furnace gas, which retains some heat energy, is collected from the furnace's to be repurposed as a fuel for heating or for electricity production. The composition of blast furnace gas typically consists of approximately 20-28 % carbon monoxide (CO), 1-5 % hydrogen (H_2), inert substances such as 50-55 % nitrogen (N_2) and 17-25 % carbon dioxide (CO_2), as well as varying amounts of sulphur and cyanide compounds. Additionally, the gas contains significant quantities of dust originating from the burden. [29]

2.2.4.2 Smelting Reduction

The process of smelting reduction combines the reduction process and the melting process. The furnace is practically divided into two units. In the second unit, the coal is gasified, resulting in the reducing gas, consisting of CO, H_2 and only small amounts of CO_2. Following the cooling to 850 °C with the use of cooling gases and the dust removal by cyclones, the gas mixture is introduced into the first unit as a reducing agent for the iron ore reduction, resulting in the formation of iron sponge. The coal in the second unit serves a dual purpose, as the heat produced during its gasification is used for the smelting of the iron sponge. The elevated temperatures of the top gas are taken advantage of, for instance in electricity production.

Smelting reduction processes can use a wider range of iron ore feedstocks, including lower-grade ores and fines, which may not be suitable for blast furnace operations. This flexibility in feedstock can lead to cost savings and resource utilization. Additionally, start-up times are shorter. [29], [32]

2.2.4.3 Direct Reduction

The process of direct reduction entails the synthesis of solid primary iron by the utilisation of iron ores and a reducing agent, such as natural gas. The solid substance is commonly referred to as direct reduced iron (DRI) and is mostly utilised as raw material in electric arc furnaces (EAF). Generally speaking, the methods for the production of DRI can be differentiated by iron ore form and energy source, as seen in Figure 12. The iron ore feedstock used must be of high quality, typically consisting of ores or concentrates with around 68 % iron content and a gangue component of approximately 27 %, as the iron is not separated from the gangue within the reduction reactor. The reducing gas used in direct reduction is typically a mixture of carbon monoxide (CO) and hydrogen (H_2). This gas is produced from natural gas through reforming. The process operates at temperatures below 1000°C. DRI produced through this process boasts

a high metallization rate (>92%) and a low carbon content (<2%). DRI procedures can be categorised according to reactor type, as follows [29]:

1. Shaft furnaces (Midrex®)
2. Rotary kilns
3. Rotary hearth furnaces
4. Fluidized bed reactors (Circored®, Circofer®, Finmet®)

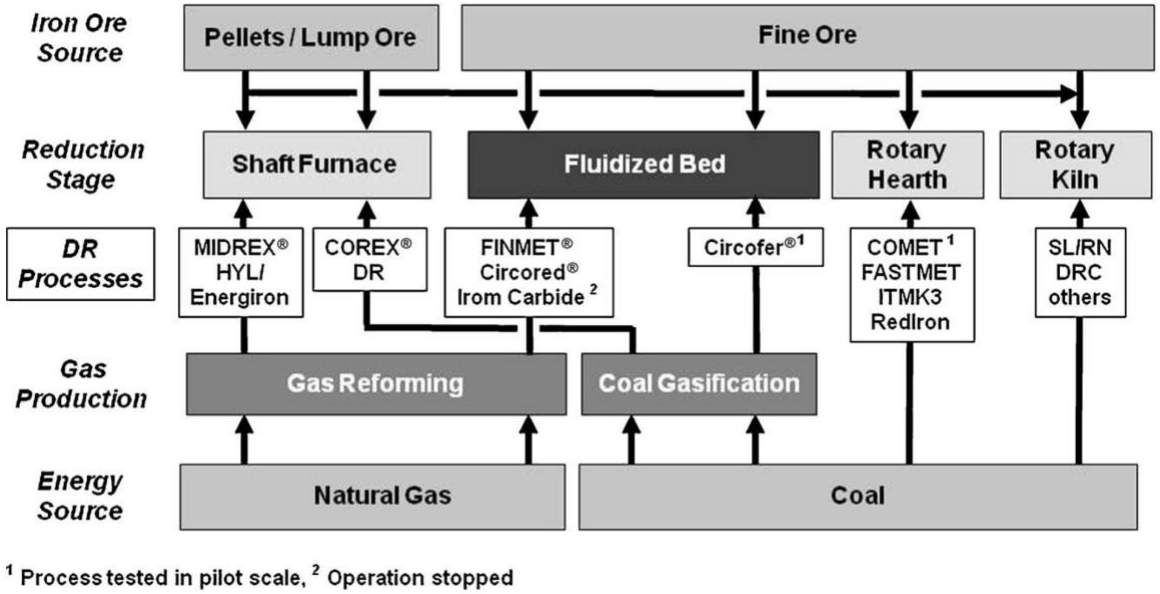

Figure 12: Classification of direct reduction processes [33]

Depending on the DRI production route, different criteria for feedstock must be met as described in [29]. While shaft furnaces necessitate iron ore pellets and lump ore, processes with a fluidized bed do not require the agglomeration of iron ore fines and concentrates.

In comparison to the blast furnace route, the CO_2 emissions can be significantly lowered by up to 25 %, when using natural gas instead of coal due to the elimination of a coke oven plant. The level of dust discharge is minimal, as is the demand for water, which can be recycled. Additionally, it is worth noting that a direct reduction unit utilising methane as its primary source emits far lower amounts of carbon dioxide compared to a unit reliant on coal. [29]

The process that is the most relevant to this thesis, is the direct reduction using a gas fluidized bed, which is why the next section will present said thematic. The two processes that fit into this category are Circored® and Finmet®, which use natural gas, and HYFOR®, which is a pilot-scale reactor for the reduction of fine iron ore with pure hydrogen.

2.2.4.3.1 Circored®

The utilisation of a two-stage reactor configuration, consisting of a circulating fluidized bed (CFB) and a bubbling fluidized bed (FB) downstream, is employed in the Circored process due to the unique reduction properties exhibited by iron ore. Figure 13 shows the various steps of the Circored process. Iron ore fines, ranging in size from 0.1 to 2.0 mm, undergo drying and preheating in a CFB preheater, elevating their temperature to approximately 900°C. Subsequently, these prepared fines are introduced into the initial CFB reactor for the primary reduction phase. The early phase of this process enables efficient pre-reduction, resulting in reduction rates of up to 80%. The final reduction phase takes place within the bubbling FB reactor, where reduction degrees exceeding 95% are attained.

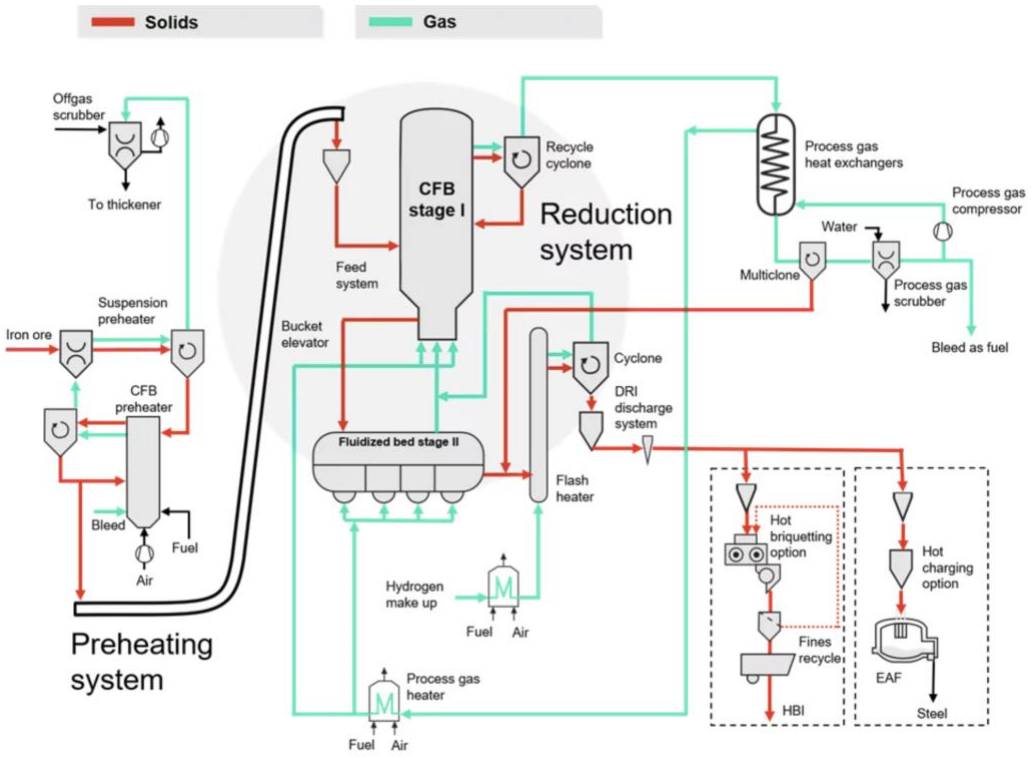

Figure 13: Flowchart of the Circored® process [34]

Hydrogen serves as the exclusive reductant in this process, allowing for relatively low operating temperatures of less than 700°C in both the CFB and FB reactors. This lower temperature helps prevent particle agglomeration and ensures better process control. Further reductions in CO2 emissions can be realized by utilizing alternative energy sources such as renewable electricity and/or non-fossil fuels. [34]

To address the processing of ultrafine ores (< 50 µm) and scrubber dust, a microgranulation process was developed, where the ultrafine particles are agglomerated into microgranules with

an average size of less than 0.5 mm by incorporating a binder. In cases involving low-grade iron ores, a viable option is to combine a single reduction stage using the Circored process, achieving a metallization degree of up to 85%, with smelting reduction performed in an electric smelter to produce hot metal. This combination offers the advantage of removing substantial impurities within the smelter through slag, with further metal refinement achievable in downstream steel facilities.

The emissions for the Circored process are 0.2 t CO_2-equivalents per ton of produced steel, which is only 11.1 % of the emissions produced by a blast furnace. When including the microgranulation for the ultrafine ores, the emissions increase by 0.7 t CO_2-equivalents per ton of steel. Although the CO_2 emissions from both the Circored process and shaft furnace direct reduction are roughly comparable, the Circored method offers an advantage by eliminating the need for the pelletizing stage. [34]

2.2.4.3.2 Finmet®

The Finmet® plant consists of a series of four fluidized bed reactors in sequence, a reformer to produce fresh reducing gas, and a briquetting section, as depicted in Figure 14.

The fine iron ore enters the first reactor R4 and drops downwards due to gravity, while the reducing gas is introduced into the final reactor and flows in a countercurrent. The reducing gas consisting of a mixture of CO and H_2 is produced by steam reforming. In the top reactor R4, the fine ore undergoes preheating to achieve temperatures of 550-570 °C, enabling the ore dehydration and the reduction of hematite to magnetite. During the downwards transfer of the ore towards the bottom reactor R1, the ore goes through more reduction steps, resulting in metallic Fe. The ore in bottommost reactor R1 is exposed to temperatures of up to 800 °C. The exhaust reducing gas leaving the first reduction reactor is subjected to a scrubbing and cooling process in order to eliminate dust and a significant portion of the water generated during the reduction process. The recycled gas is mixed with the produced natural gas to act as reducing gas. [35]

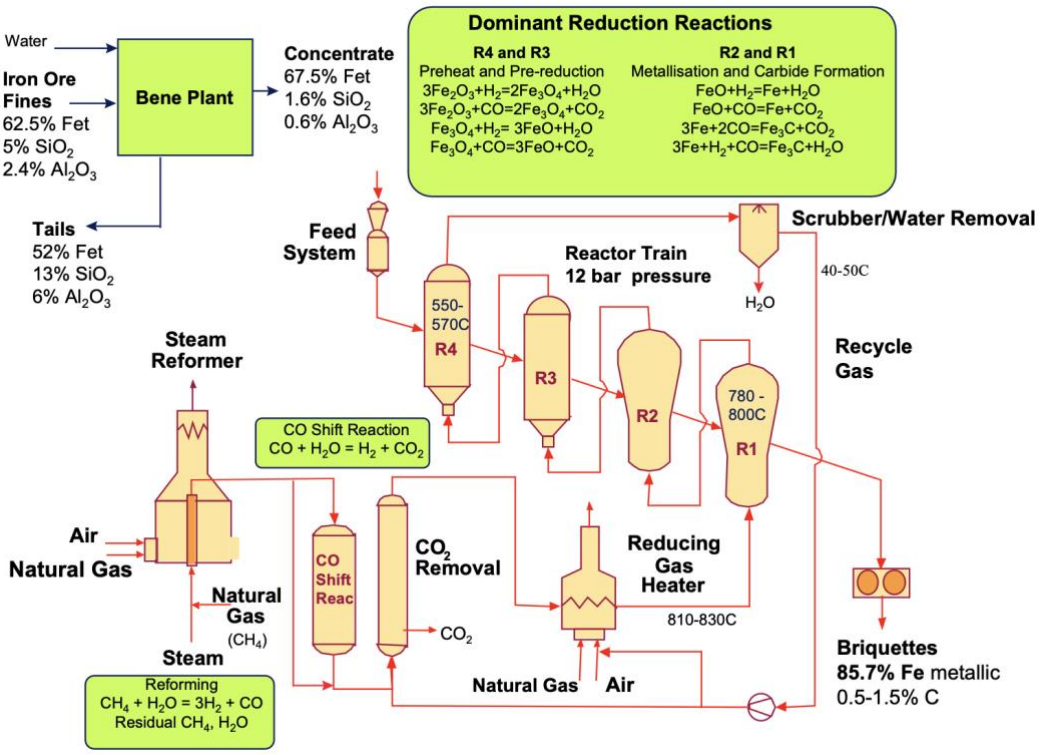

Figure 14: Flowsheet of the Finmet® Process [35]

2.2.4.3.3 FINEX®

The Finex® process differentiates itself from the blast furnace route by mainly three points, first one being the direct use of gasified coal as a reducing agent and energy source. In addition, no agglomeration processes such as sintering or pelletising are necessary, resulting in the direct charge of fine iron ore with a typical mean grain size of 1 to 2 mm. As pure oxygen instead of nitrogen – rich hot blast is used, the export gas only contains low amounts of nitrogen and can be utilized for reduction work, for heat or energy generation due to its high net calorific value. The Finex® process is characterized by its separation into two process steps, first reduction in the fluidized bed reactor tower followed by reduction in the the melter- gasifier. As the first step, the iron ore and the additive drier are pneumatically transported to a series of three fluidized bed reactors. The reduction gas produced in the melter-gasifier flows through each of the fluidized-bed reactors in a counter-flow direction to the ore. The ore undergoes progressive reduction. Once the reduced iron exits the last fluidized-bed reactor, it is compressed into a material known as hot-compacted iron (HCI). This HCI is then conveyed through a hot-transport system to the upper section of the melter-gasifier, where it is directly combined with coal for charging into the melter-gasifier. The coal releases hydrocarbons, which are dissociated to carbon monoxide and hydrogen at high temperatures of 1000 °C. By oxygen injection into the melter – gasifier, the coal is gasified, resulting in heat generation and the production of a

valuable reduction gas, consisting of mainly carbon monoxide and hydrogen. The produced reduction gas is introduced into the fluidized beds, following a cleaning process. The Finex® product´s quality is identical to the one produced by the blast furnace route. By incorporating CCS (Carbon Capture and Storage) to the Finex® process, the CO_2 emission rate could be decreased by 45 % in comparison to the CO_2 emissions of the blast furnace route.[36]

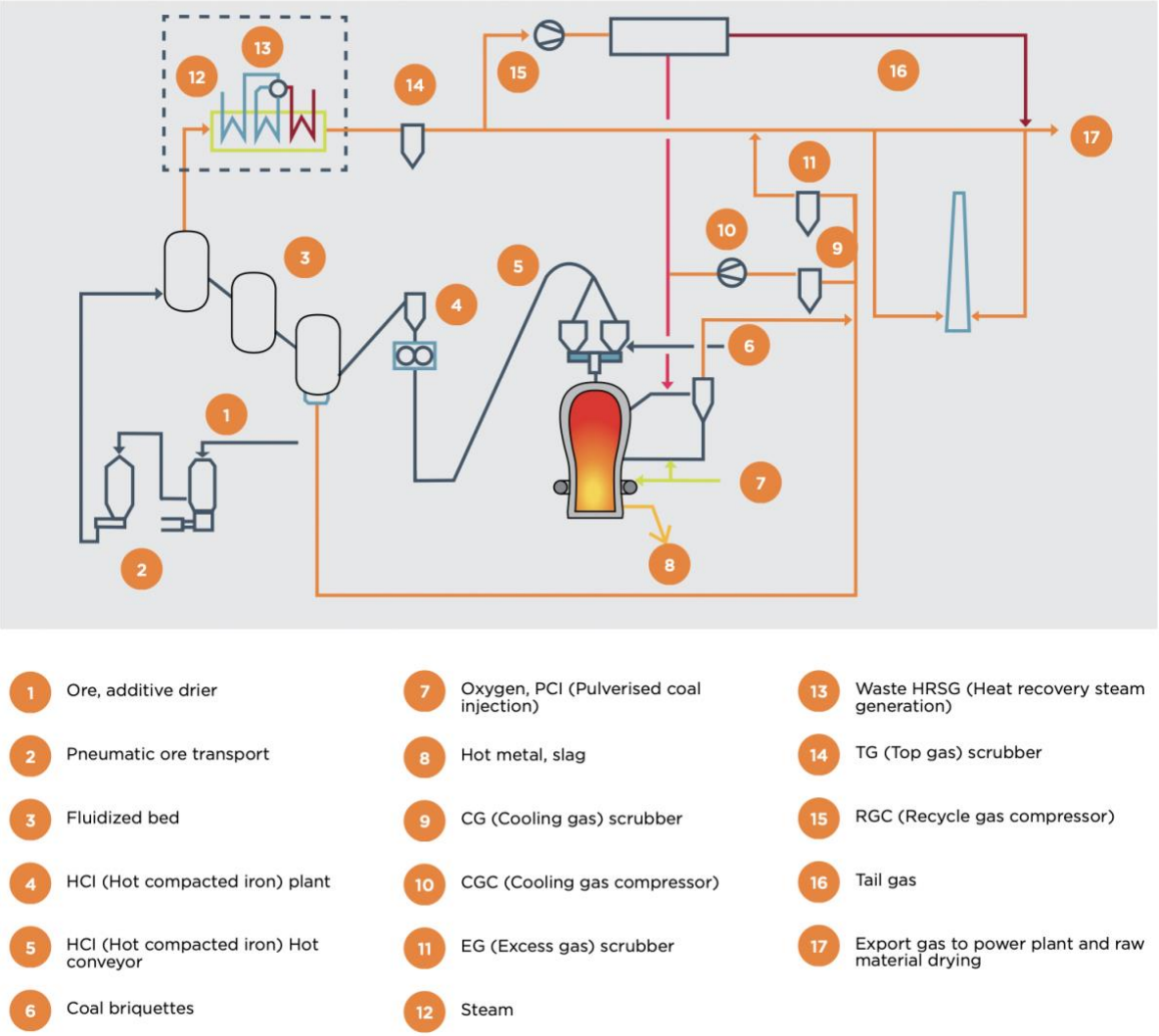

Figure 15: Flowsheet of the FINEX® Process [36]

2.2.4.3.4 HYFOR®

The HYFOR® enables the exclusive utilization of environmentally friendly or low-carbon hydrogen (H_2) as the reducing agent, effectively circumventing the generation of CO_2 during reduction. The new process uses 100% hydrogen from renewable energy sources, or alternatively H_2-rich gases from other gas sources such as natural gas pyrolysis or conventional steam reformers, resulting in a low or even zero CO_2 footprint. The distinctive feature of the

HYFOR process lies in its capacity to employ iron ore concentrates with particle sizes entirely below 150 µm, which is a typical characteristic of various iron ore concentrates. This capability extends across all types of iron ore, including hematite, limonite, and magnetite, regardless of their quality, whether high or low. A pilot plant was successfully started up in Donauwitz in 2021.[37]

The pilot plant comprises three distinct sections, as depicted in Figure 16: the preheating-oxidation unit, a gas purification system, and the core reduction unit. The material is introduced into the reactor, while a weir is built on the opposite side to maintain a consistent bed height within the reactor. This allows for the adjustment of residence time. The material that passes over the weir can be pneumatically transferred back to the material bins and recharged into the reactor. This process ensures that the overall required reduction time is achieved in order to reach the specified metallization degree. Prior to entering the reactor, the hydrogen required for the reduction process undergoes pre-heating within a heat exchanger. In the preheating-oxidation unit, the finely ground ore concentrate is subjected to temperatures up to 900 °C, followed by the introduction into the reduction unit. The resulting hot direct-reduced iron (HDI) exits the reduction unit at approximately 600 °C before undergoing cooling.[37], [38]

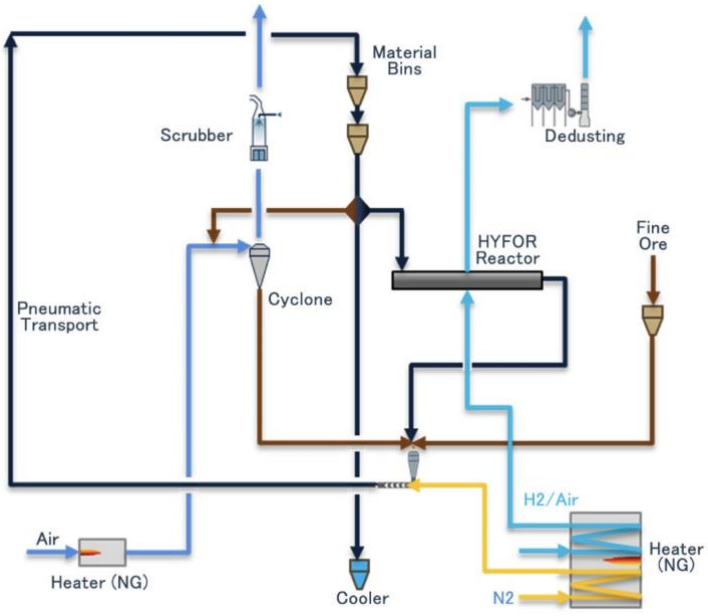

Figure 16: Schematic flowsheet of the HYFOR® pilot plant [38]

Following the fluidization and reduction of the material, the off-gas is dedusted before undergoing post-combustion and exiting into the surrounding environment. In an industrial setting, it's highly likely that a recirculation system for unreacted hydrogen would be implemented. The dust separated during this process is reintroduced into the reactor, thereby

enhancing the overall process yield.[37], [38]

The next stage will involve the expansion of the pilot operation through the incorporation of a hot-briquetting test facility, aimed at producing hot-briquetted iron (HBI). The objective of this study is to verify the effectiveness of the HYFOR® process and utilise the experimental trials as a means to collect the necessary data for the eventual implementation of a large-scale industrial prototype.[37]

A potential industrial prototype plant is depicted in Figure 17. A series of cyclones is used for the pre-heating and oxidizing of the material. The necessary energy provided by a hot gas generator fueled by hydrogen-containing bleed gas from the recycle gas loop. Following pre-heating, the material is placed in a bin to serve as a buffer before entering the initial reduction reactor. Adequate residence times are achieved by the employment of multiple reduction reactors in sequence. Each reactor receives an injection of clean reducing gas. The off-gas from all reactors undergoes separation of dust, which is reintroduced into the reducing reactors with high efficiency. [38]

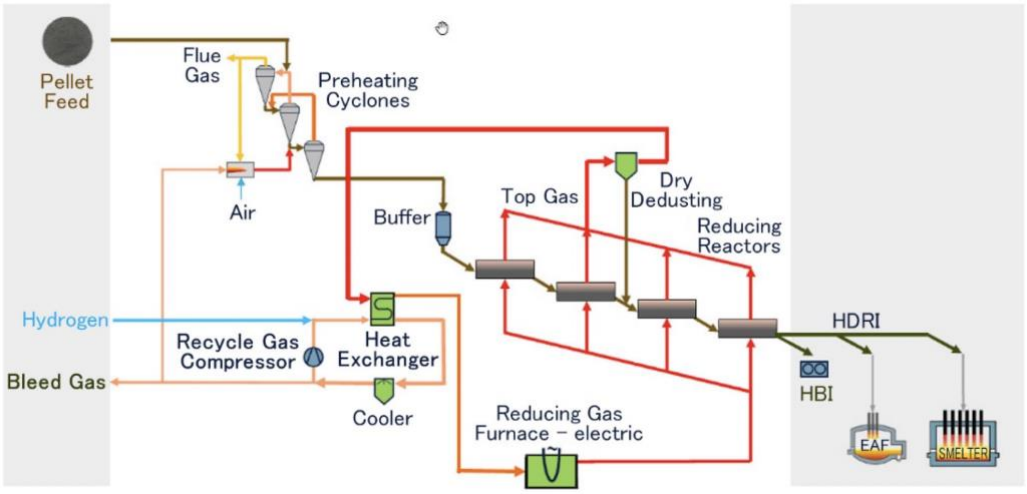

Figure 17: HYFOR Industrial Prototype Plant - Schematic Flowsheet [38]

2.3 Fluidized Bed Scale-Up using Scaling Parameters (Similarity Theory)

This section presents the scaling relationships for fluidized bed, starting with a basic explanation of its derivation and the simplification of the scaling parameters by making assumptions along the way. These similarity criteria are essential for the cold model experiments, to ensure that the results from the cold tests are applicable to the reduction tests, it's essential for the cold tests to exhibit fluid-dynamic similarity with the reduction tests. This can be achieved by utilizing similarity criteria, which define the test parameters for the cold

tests. This approach enables the execution of cold tests that accurately replicate the flow dynamics within a fluidized bed for iron ore reduction.

The complete set of scaling relationships is derived by non-dimensionalizing the equations of motion for both the particles and the fluid within a fluidized bed, in addition to their respective boundary conditions. By taking the characteristic bed dimension, denoted as "L," as a representative length dimension, the non-dimensionalization of these equations results in the following dimensionless parameters[39]:

$$\frac{\beta \cdot d_p}{\rho_s \cdot u_0}, \frac{g \cdot d_p}{{u_0}^2}, \frac{L}{d_p}, \frac{D}{d_p}, \frac{\rho_F}{\rho_s}, \frac{P_0}{\rho_s \cdot {u_0}^2} \tag{2.29}$$

The components that are not taken into account include surface forces exerted on particles as a result of factors such as static charge or Van der Waals forces. In addition, the omission of the influence of the particle's coefficient of restitution or friction coefficient on inter-particle forces has been noted.[40]

The initial non-dimensional parameter signifies the proportion of particle drag compared to inertia forces, while the second parameter indicates the proportion of the gravitational force acting on the particle relative to the particle's inertia force. The term $\frac{P_0}{\rho_s \cdot {u_0}^2}$ may be deemed negligible in situations when the fluid velocity is considerably lower than the sonic velocity or when the absolute pressure variations are insufficient to appreciably affect the thermodynamic parameters of the fluid. The coefficient β can be expressed through the Ergun equation, when the particles are close to one another, almost equal to a packed bed, as follows [39]:

$$\frac{\beta \cdot d_p \cdot \Phi_S}{\rho_s \cdot u_0} = 150 \cdot \frac{\epsilon \cdot (1-\epsilon)^2}{\epsilon^3} \cdot \frac{\mu}{\rho_s \cdot u_0 \cdot d_p \cdot \Phi_S} + \frac{1.75(1-\epsilon) \cdot \rho_f \cdot \left|\bar{u}' - \bar{v}'\right| \cdot \epsilon^2}{\epsilon^3 \cdot \rho_s} \tag{2.30}$$

Therefore, the first parameter in Equation (2.29) can be replaced by the Reynolds number. While the viscous component of the drag is best described by the first term in Equation (2.30), the second term corresponds to the fluid´s inertia.

As a condition for fluid-dynamic similarity, the fluidized bed in the model as well as in the scaled- up plant must exhibit the same geometry. In addition to sharing the same Reynolds number, Froude number, and the ratio of particle to fluid density, sphericity and dimensionless particle size distribution must be equal. When dealing with small Reynolds numbers ($Re_p < 4$), the fluid inertia forces can be neglected, eliminating the second term of Equation (2.30)

resulting in a region dominated by viscous forces. Besides particle size distribution and bed geometry, the governing parameters for the viscous region become[39]:

$$\frac{g \cdot d_p}{{u_0}^2}, \frac{\mu}{\rho_s \cdot U_0 \cdot d_p}, \frac{L}{d_p}, \frac{D}{d_p}, \Phi_S \tag{2.31}$$

The first term is the Froude number (Fr). The combination of the second term with the first one to eliminate the superficial velocity results in a modified form of the Archimedes number (Ar).

Glicksman simplified Equation (2.31) in [41] as follows:

$$\frac{g \cdot d_p}{{U_0}^2}, \frac{L}{d_p \cdot Re}, \frac{L}{D}, \Phi_S, \text{particle size distribution, bed geometry} \tag{2.32}$$

Equation (2.32) can be rewritten to incorporate the minimum fluidization velocity [41]:

$$\frac{{U_0}^2}{g \cdot L}, \frac{U_o}{U_{mf}}, \frac{L}{D}, \Phi_S, \textit{particle size distribution} \tag{2.33}$$

For high particle Reynolds number, greater than 400, the viscous drag forces can be neglected due to the low influence of the fluid´s viscosity, resulting in the following governing parameters [39] :

$$\frac{g \cdot d_p}{{U_0}^2}, \frac{\rho_F}{\rho_s}, \frac{L}{d_p}, \frac{D}{d_p}, \Phi_S, \text{particle size distribution, bed geometry} \tag{2.34}$$

The three dimensionless numbers derived from the scaling relationships are listed in Table 1.

Table 1: Dimensionless numbers

Reynolds Number	$Re = \frac{\text{Inertial forces}}{\text{Viscous forces}} = \frac{\rho_g \cdot U \cdot d_p}{\mu}$	(2.35)
Archimedes Number	$Ar = \frac{\text{Gravitational forces}}{\text{Viscous forces}} = \frac{\rho_g \cdot g \cdot (\rho_p - \rho_g) \cdot d_{SV}^3}{\mu^2} = \frac{g \cdot (\rho_p - \rho_g) \cdot d_{SV}^3}{\rho_g \cdot \nu^2}$	(2.36)
Froude Number	$Fr = \frac{\text{Inertial forces}}{\text{Gravitational forces}} = \frac{U^2}{g \cdot d_p}$	(2.37)

2.4 Reh and Grace Diagram

Utilizing a diagram proves beneficial in showcasing essential values and improving the understanding of fluidization patterns. By employing at least two dimensionless similarity numbers, one can pinpoint the operational point of a specific condition within a generalized regime map. Reh (1961) introduced a meaningful chart, incorporating the modified Froude number (Fr*) on the vertical axis and the Reynolds number (Re) on the horizontal axis. The Reh chart additionally exhibits the Archimedes number (Ar) and the Liatschenko number (Ω), signifying the influences of particle density and gas velocity. The dimensionless numbers needed for the Reh diagram are listed in Table 2. [42]

Table 2: Dimensionless numbers for Reh Diagram

Reynolds Number	$Re = \frac{\rho_g \cdot U \cdot d_p}{\mu}$	(2.38)
Modified Froude Number	$Fr^* = \frac{3}{4} \cdot \frac{U^2 \cdot \rho_g}{g \cdot d_p \cdot (\rho_p - \rho_g)}$	(2.39)
Archimedes Number	$Ar = \frac{\rho_g \cdot g \cdot (\rho_p - \rho_g) \cdot d_{SV}^3}{\mu^2}$	(2.40)
Liatschenko Number	$\Omega = \frac{U^2 \cdot \rho_g}{\mu \cdot g \cdot (\rho_p - \rho_{g)}}$	(2.41)
Bed Porosity	$\varepsilon = 1 - \frac{\rho_{bulk}}{\rho_p}$	(2.42)

For a given particle diameter, the fluidization velocity is determined by moving along the lines with constant Archimedes number, whereas the particle diameter for a specified velocity value is deduced by moving along the lines with constant Ω- Number. [42], [43]

Grace (1986) then presented a fluidization diagram with some modifications, integrating the ranges of minimum fluidization velocity (U_{mf}) and terminal velocity (U_t). Grace (1986) opted for an arrangement of dimensionless numbers explicitly related to fluidization velocities (U*) on the vertical axis and particle diameters (d_p*) on the horizontal axis for this modification, as listed in Table 3.[42], [43]

Table 3: Dimensionless numbers for Grace Diagram

Modified Particle Diameter	$d_p^* = Ar^{\frac{1}{3}}$	(2.43)
Modified Fluidization Velocity	$u^* = \frac{Re}{Ar^{\frac{1}{3}}} = \Omega^{\frac{1}{3}}$	(2.44)

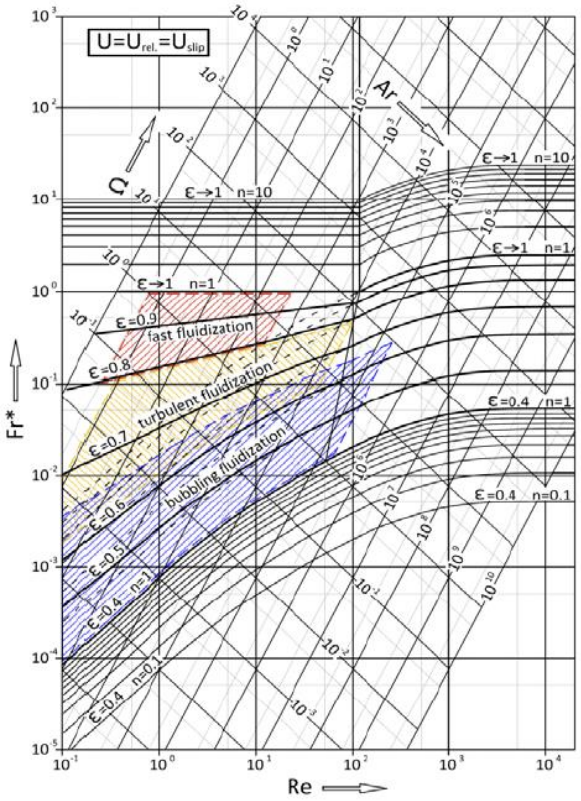

Figure 18: Fluidization regime map following Reh[44]

The Reh and Grace diagrams, depicted in Figure 18 and Figure 19, exhibit a remarkable agreement, particularly in illustrating the distinctive behaviour of gas-solid systems undergoing fluidization with an Archimedes number smaller than approximately 10000. Notably, the behaviour of the smallest particle sizes belonging to Geldart's (1973) "group B" and particularly "group A" particles deviates significantly from observations of individual particles. Reh (1961) illustrates this phenomenon by expanding the region of varying fluidized bed porosity (voidage) between (ε=0.4) at (U_{mf}) and ($\varepsilon \rightarrow 1$) at (Fr*=1). Using data from Kunii and Levenspiel (1997) the three most common fluidization regimes within the Reh diagram can be roughly pinpointed.[42]

Bi and Grace (1995a) further elaborate on this by introducing determined velocity lines as boundaries between discernible flow regimes (U_{se}, U_c). The superficial gas velocity (U_0) at

which a substantial entrainment of solids from the fluidized bed reactor initiates is represented by (U_{se}). This velocity marks the transition from turbulent to fast fluidization. Considering (U_c) as the boundary for turbulent fluidization, its determination involves various pressure measurement methods such as differential pressure fluctuations (DPF) and absolute pressure fluctuations (APF). To account for these variations, the Grace diagram integrates two boundary lines within the diagram.[42]

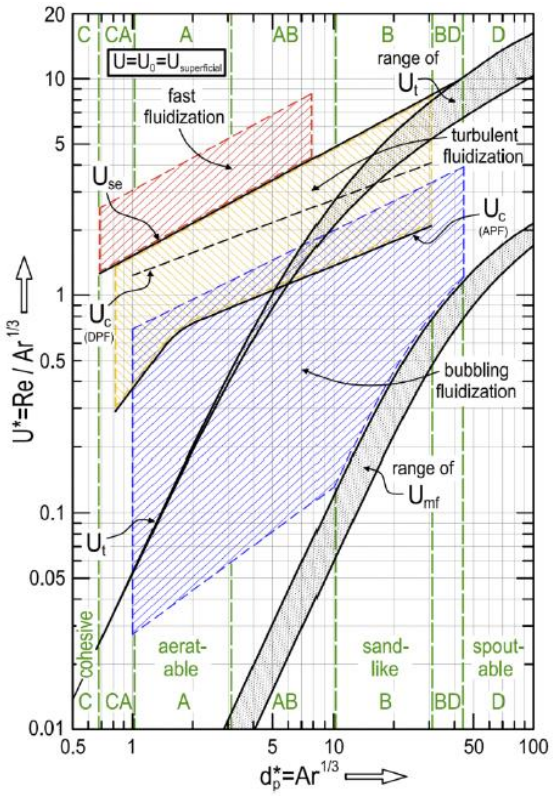

Figure 19: Fluidization regime map following Grace [45]

A significant contrast between Reh´s and Grace´s method lies in the employment of different velocities when computing the dimensionless parameters for their respective diagrams. Within fast fluidized beds, notable phenomena such as particle agglomerations and intense back-mixing processes occur, both in wall layers and the core flow. The fast fluidization regime is characterized by a continual formation and breakup of various flow structures and mixing conditions, which change with the height of the fluidized bed reactor. Hence, for precise calculations of (Ω, Re, Fr*, c_D) using the Reh diagram (1961), one must account for the slip velocity (u_{slip}) and solids feed/circulation rate (G_s). However, gas flow velocity and slip velocity between the gas phase and solids vary and are not easily predictable across different locations. Furthermore, slip velocity between gas phase and solids is not as readily available as superficial velocities(u_0), which is the velocity that Grace adopted for computing fluid dynamic similarity

numbers. The calculation for slip velocity for the Reh diagram, as well as the superficial velocity for the Grace Diagram are given by Equations 2.45 and 2.46.[42]

$$U_{slip} = \frac{U}{\varepsilon} - \frac{G_s}{(1-\varepsilon)\cdot\rho_p} \tag{2.45}$$

$$U = \frac{\dot{V}_g}{A_0} \tag{2.46}$$

The solids feed rate G_s can be calculated as followed, where the terminal velocity is calculated as in [46]:

$$G_s = \rho_B \cdot (U - U_t) \tag{2.47}$$

$$U_t = \frac{g\cdot(\rho_p - \rho_f)\cdot d_p^2}{18\cdot\mu} \text{ for } Re < 2 \tag{2.48}$$

$$U_t = 0.153\,\frac{g^{0.71}\cdot(\rho_p - \rho_f)^{0.7}\cdot d_p^{1.14}}{\rho_f^{0.29}\cdot\mu^{0.43}} \text{ for } Re \sim 2-500 \tag{2.49}$$

2.5 Similar Research – State of the Art

2.5.1 Cold Model Experiments with Helium at TU Wien

Habermann [47] optimized test conditions for tests in the hot reactor by performing reduction tests in a cold model. The gas mixture of the hot reactor is simulated by using a mixture of helium and nitrogen in the cold model (25 °C), which shows the same density as the gas mixture at temperatures of 780 °C. The composition of the mixture consisting of helium and nitrogen is determined by applying the laws of similarity. [47]

It is crucial to choose test conditions that ensure effective fluidization of particles within the fluidized bed, promoting ideal mixing. Additionally, measures need to be taken to avoid the discharge of fine particles, which tends to increase during the reduction tests. The quality of fluidization can be thoroughly assessed through cold tests conducted in the cold model. Consequently, the results are derived from visual observations, pressure measurements, and discharge measurements.[47]

During the reduction tests, it is expected that particle size reduction and oxygen depletion will occur, resulting in a higher proportion of fine particles. To mimic this phenomenon, 25% fines

(< 0.063 mm) were intentionally added to the remaining ore fraction (0.063 - 1.0 mm).

The tests showed that a fluidization velocity of over 0.2 m/s was ideal to achieve good fluidization. However, at velocities over 0.3 m/s, the iron ore loss could reach values of more than 2 %. In order to avoid high losses during the reduction tests, the gas velocity should therefore not exceed 0.3 m/s. [47]

2.5.2 Fluidized Bed Reactor at TU Wien

To explore reduction kinetics for potential use in industrial facilities, a laboratory-scale pressured fluidized bed reactor (PFBR) was constructed based on chemical similarity criteria [75]. The "reactor in pressure vessel" setup, which involves placing the fluidized bed reactor and gas preheating system inside a pressure vessel to prevent pressure differentials at the reactor's hot walls and to realize temperatures of up to 900 °C and pressures of up to 10 bar. The upper section of the reactor has a conical shape to decrease superficial velocity and prevent the loss of sample material during processing. The reactor is divided into a gas preheating section, where sand is used as bed material, and a reduction section, where the reduction of iron ore takes place. An internal cyclone is utilized to separate exhaust gas from ore particles, and the reactor is heated using electrical heating. All components of the reducing gas (H_2, N_2, CO, CO_2, CH_4), except for water vapor, are sourced from gas bottles, with the water vapor being supplied by a steam generator. To prevent condensation of water vapor, all pipes are insulated and equipped with electrical heating. In order to establish the necessary pressure level and mitigate the potential for additional chemical reactions in the event of a leak, the pressure vessel is filled with inert gas (N_2). The process is monitored by flue gas analysis using a FT-IR spectrometer.[24]

The sampling of bed material is carried out under operating conditions. The sampling system consists of a pneumatic cylinder, that is moved back allowing the sample material to flow through a pipe to a sample container. The connecting pipe is separated into two sections by a ball valve to facilitate the removal of the sample container. While the analysis by FT – IR spectrometer gives information about the flue gas' composition, which in result enables the determination of the reduction degree, microscopic analysis is used to visualize morphological changes of the reduced material. [24]

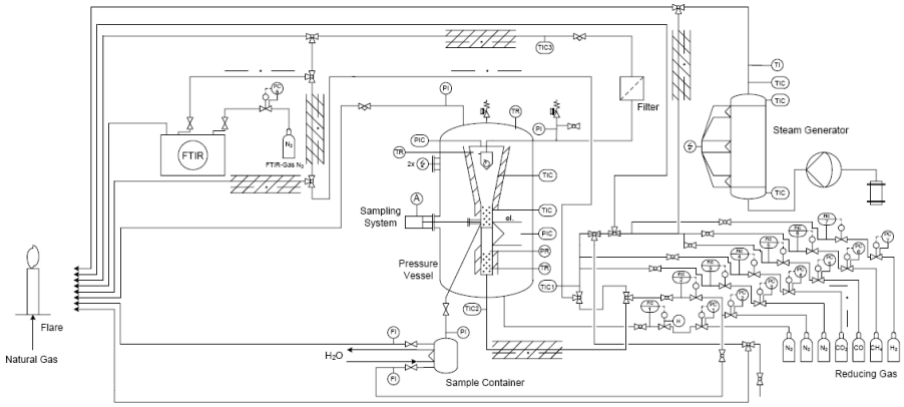

Figure 20: Flow chart of the compressed fluidized bed reactor [24]

3 Experimental

This chapter focuses on the design of the cold model including the selection of rotameters and the experimental setup. Furthermore, the test procedures are explained in detail. By conducting cold model experiments, the fluidization behaviour of the iron ore and the sand are investigated by determining the minimum fluidization velocity and identifying the influence of particle diameter and particle distributions on the minimum fluidization velocity. In addition, the effect of an internal cyclone is to be studied as part of the cold tests.

3.1 Experimental Setup

The piping and the rotameter for the test setup were designed to fit the existing cold model, which has the identical dimensions as the hot reactor in the pressure vessel. A rack was designed to set up the cold model with its instruments. Two separate racks (seen in Figure 21) made of item profiles, allow the setup to be separated into two parts, one being the cold model (left side when looking from the front), the other being the rotameter and piping with suitable storage possibilities. The front view (Figure 21a) shows the front side with two magnetically lockable doors where samples etc. can be stored. The side view (Figure 21b) also clearly shows the storage area, which has been adapted so that a screen can be set up for pressure measurement recordings. The view from the back (Figure 21c) shows another set of magnetically lockable doors with some storage to fit the piping needed for the rotameters.

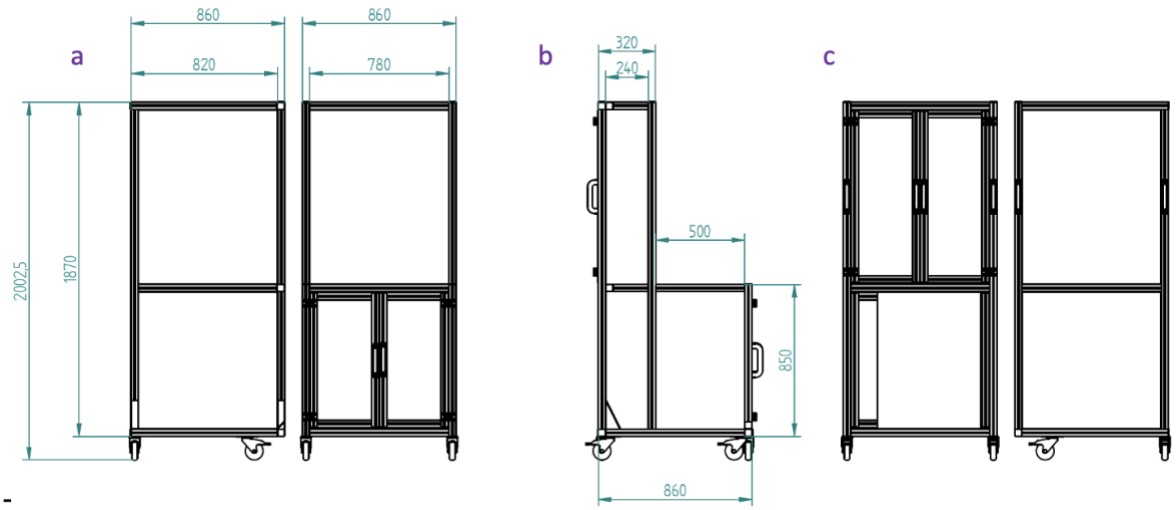

-

Figure 21:a) Front view of test rack with dimensions; b) Side view of test rack with dimensions; c) Back of view of the rack[48]

In order to determine the right rotameter for this setup, theoretical calculations were performed [49] to specify the necessary flowrates, assuming lowest and highest particle diameters of sand

and iron ore, which are listed in Table 4.

The flowrate is calculated by determining the Archimedes number and then the minimum fluidization velocity, which is lastly converted into a volume flow by multiplication with the cross-sectional area of 0.00128 m^2. Since the use of helium as fluidization gas is supposed to be investigated and compared to air as fluidization gas, flowrates for both gases must be calculated, as seen in Table 5 and Table 6.

Table 4: Assumptions for lowest and highest particle diameters

	Minimum Particle Diameter	**Maximum Particle Diameter**
	$d_{p,min}$	$d_{p,max}$
	µm	µm
Iron Ore	125	1000
Sand	300	1000

Table 5: Calculation of Flowrates for Rotameter assuming air as fluidization gas

Fluidization Gas: Air						
	Archimedes Number (Ar)		**Minimum Fluidization Velocity (u_{mf})**		**Volume Flow ($\dot{V}$)**	
	-		m/s		L/min	
	Ar_{min}	Ar_{max}	$u_{mf,min}$	$u_{mf,max}$	$\dot{V}_{min}$	$\dot{V}_{max}$
Iron Ore	120	61300	0.0122	0.56	0.933	42.9
Sand	1210	45000	0.0478	0.41	3.66	31.4

Table 6: Calculation of Flowrates for Rotameter assuming helium as fluidization gas

Fluidization Gas: Helium						
	Archimedes Number (Ar)		**Minimum Fluidization Velocity (u_{mf})**		**Volume Flow ($\dot{V}$)**	
	-		m/s		L/min	
	Ar_{min}	Ar_{max}	$u_{mf,min}$	$u_{mf,max}$	$\dot{V}_{min}$	$\dot{V}_{max}$
Iron Ore	14.2	729	0.013	0.682	0.865	52.2
Sand	364	535	0.374	0.476	28.6	36.4

Considering the resulting flowrates, it was decided to use four rotameters, which are appropriate for different flowrate ranges, as listed in Table 7. Since the test equipment is supposed to include the possibility of creating a fluidization gas by mixing two gases, the rotameter setup was doubled, therefore meaning eight rotameters, four for every respective gas.

Table 7: Rotameter - Flowrates

Rotameter Nr.	Flowrate Range
Rotameter 1	0 – 1.2 L/min
Rotameter 2	0 – 5,5 L/min
Rotameter 3	0 – 10 L/min
Rotameter 4	0 – 50 L/min

While the air for the experiments is provided by a compressor, helium is stored in a gas bottle. For both gases, pressure reducing valves regulate the gas pressure, with which the gas enters the rotameter series. To enable the pressure measurement recording, an SPS system is integrated into the cold model.

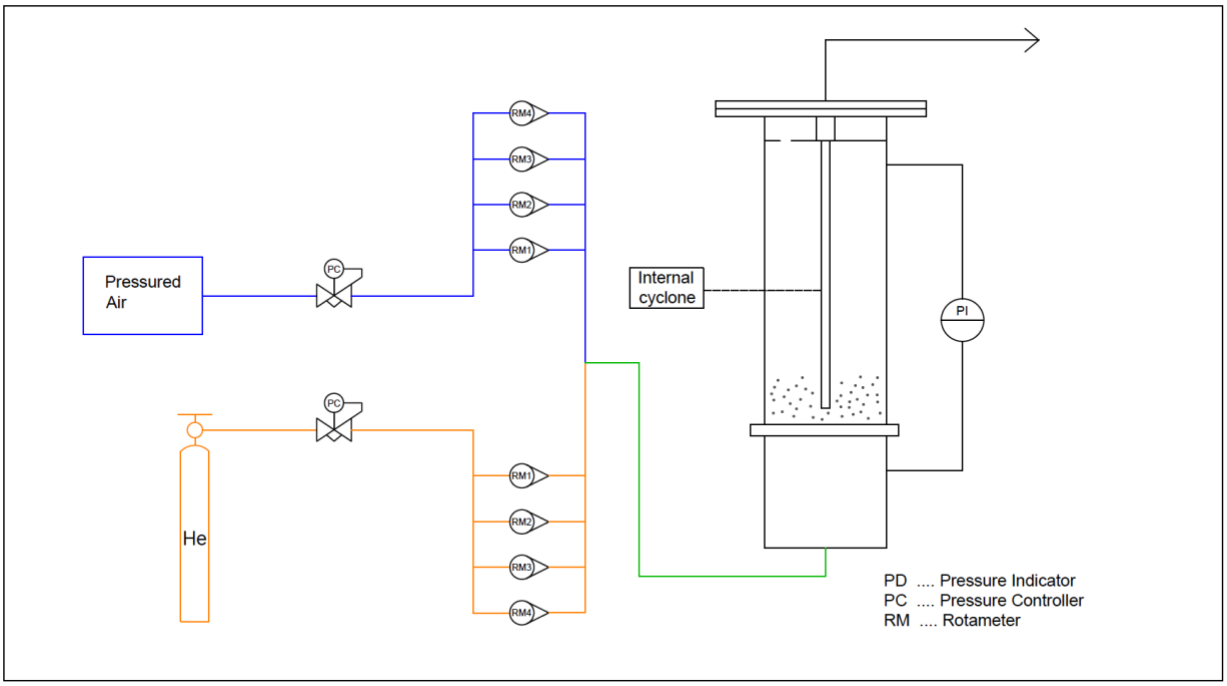

Figure 22: Cold Model - Experimental Setup

The flow chart of the cold model is depicted in Figure 22. The cold model itself consists of Plexiglas, which has the same geometries as the hot model, and a detachable internal cyclone. The cold model is made up of three parts, which can be disassembled, allowing for the insertion of the sieve tray, which is where the bed of particles is placed on. As mentioned before, the reactor is divided into three parts, which simulate the gas entry zone, preheating zone and the reduction zone. The sieve tray for the bed of particles is situated between preheating zone and reduction zone. After entering the cold model at the bottom, the gas flows through the fluidized bed of particles and exits at the top, where the model is closed by removable lid.

In order to measure the pressure drop across the fluidized bed, the pressure is measured at two points by two pressure cells: One before the sieve tray and the bed of particles and one right before the gas exit. Due to the placement of the first pressure cell right before the sieve tray, the pressure drop over the sieve tray must be subtracted from the pressure drop measured over the fluidized bed.

3.2 Test Matrix

Prior to starting a test series, the cold model setup is validated by running tests with silica sand and comparing results to [49]. In the test series, the focus is set on mixtures of iron ore fines in a range from 0.063 - 0.125 mm particle diameter and quartz sand in ranges from 0.1 – 1 mm. Iron ore particles with diameters of up to 1 mm are analyzed. The chosen mixtures are listed in Table 8.

Table 8: Sample Mixtures – Test Matrix

Sample Name	Particle Distribution Size		Mass Share	
	mm		%	
	Iron Ore	Sand	Iron Ore	Sand
P1	0.063 – 0.125	0.1 – 0.8	20	80
P2	0.063 – 0.125	0.1 – 0.8	40	60
P3	0.063 – 0.125	0.1 – 0.8	80	20
P4	0.063 – 0.125	0.1 – 0.2	20	80
P5	0.063 – 0.125	0.1 – 0.2	40	60
P6	0.063 – 0.125	0.5 – 0.8	20	80
P7	0.063 – 0.125	0.5 – 0.8	40	60
P8	0.5-1	0.8-1	40	60
P9	0.5-1	0.5-1	20	80
P10	0.5-1	0.5-1	40	60

For every mixture, cold model tests are conducted with air and helium and no cyclone, just as well as with an attached internal cyclone, meaning four tests per mixture (e.g. P1.1-P1.4).

3.3 Test Procedure

Prior to performing any tests, the accuracy of the rotameter must be tested with a gas meter. The tests are performed as followed: First, the sample is filled onto the sieve tray by opening the lid at the top of the cold model, while opening one of the rotameters for the fluidization gas to push the particles slightly up and ensure that no iron ore fines pass through the sieve. Then

the rotameter is closed. Prior to shutting the lid, the internal cyclone is attached or detached to the lid of the model with screws, depending on the test being conducted.

In order to start the fluidization investigation of the bed particles, the rotameter with the smallest flow range is opened and the volume flow is increased, while recording the measured pressure drop. Once the upper end of the flowrate spectrum of the rotameter is attained, the volume flow is decreased step by step and the pressure continues to be documented. These steps are carried out for every rotameter until reaching the fluidization point, characterized by a constant pressure drop.

To confirm the fluidization point, the flowrate is raised further, until no significant change at volume flows of up to five times the fluidization point is noticeable. After finishing a test run with air or helium, the other gas is connected, and the same procedure is repeated. In-between tests the cold model is cleaned, and the new samples are prepared.

3.4 Sample Analysis

In order to calculate the theoretical minimal fluidization velocity, a particle diameter for every sample must be assumed. This particle diameter is determined by sieve analysis. All the mixtures, as well as the pure iron ore and sand fractions undergo a sieve analysis in a vibration sieve machine for five minutes at an amplitude value of 1.

Additionally, the bed density is calculated by measuring the mass and volume of a sample bed of particles in a cylinder. The determination of the bed density is necessary for the calculation of the bed porosity.

3.5 Fluidization Gas

In this thesis, air and helium are used as fluidization gases. This chapter focuses on these fluids` properties and their dependency on temperature at atmospheric pressure. Furthermore, the use of helium as a fluidization gas in the cold model experiments is explained.

The quality of fluidization can be notably influenced by gas properties, particularly the two thermophysical properties, density and viscosity.

3.5.1 Temperature Dependence of Density

The fluidization gas in the hot model consists of a multitude of gases (H_2, N_2, O_2, CO, CO_2,

H_2O), the main one being hydrogen. Since the hot model is compressed, the thermophysical data for hydrogen is shown for a pressure of 5 bar, which corresponds to the pressure in the future hot model, in addition to the data for atmospheric pressure. The fluid property data for hydrogen and helium is taken from NIST (National Institute of Standards and Technology) [50], while the data for air is taken from VDI Heat Atlas [11]. The data for hydrogen is only available for temperatures up to 700 °C, which is why the not available densities are calculated by the ideal gas law, while the dynamic viscosities are calculated by Equation 2.9 and then converted into kinematic viscosities by dividing with the according densities. The constants A-E for hydrogen are given in Table 9.

Table 9: Constants A-E for hydrogen for calculation of its dynamic viscosity

A	B	C	D	E
1.8024E-06	2.7174E-08	-1.3395E-11	5.85E-15	-1.04E-18

In order to simulate the fluidization of hydrogen in the hot model, helium is used in the cold model due to the similarity in densities of helium and hydrogen at cold (atmospheric pressure) and hot model pressure conditions (5 bar). As seen in Figure 23, hydrogen at atmospheric pressure shows the lowest density of the three investigated gases, while air exhibits the highest values.

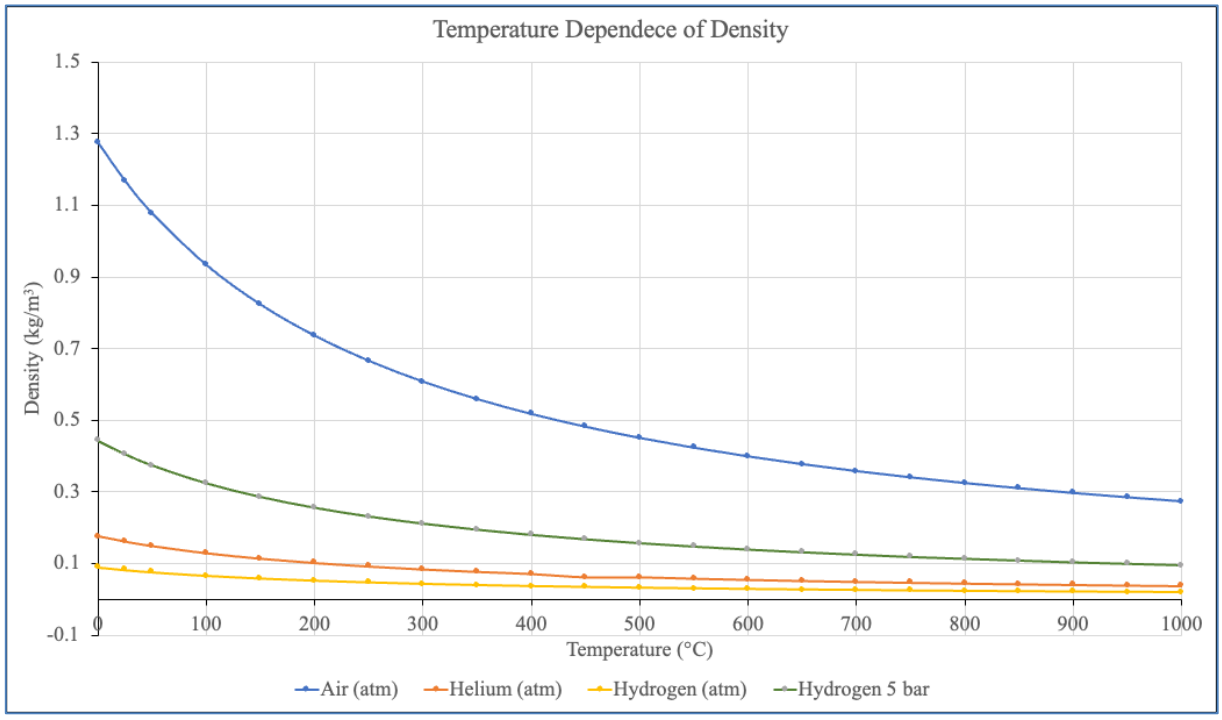

Figure 23: Temperature Dependence of Density

At room temperature (25 °C), the density of helium approximately corresponds to the one of

hydrogen at 700 °C and 5 bar (approximate operation temperature). The density of both air and helium decrease with increasing temperature, just like hydrogen.

3.5.2 Temperature Dependence of Kinematic Viscosity

The dependence of kinematic viscosity on the temperature is the exact opposite to the one of density, as depicted in Figure 24. With increasing temperature, the viscosity of air, helium and hydrogen increase. While helium displays the lowest density, it also reveals the highest viscosity. The kinematic viscosities of hydrogen and helium at atmospheric pressure demonstrate similarities, while the kinematic viscosity for hydrogen at hot model pressure conditions seems to correspond better with the kinematic viscosity of air.

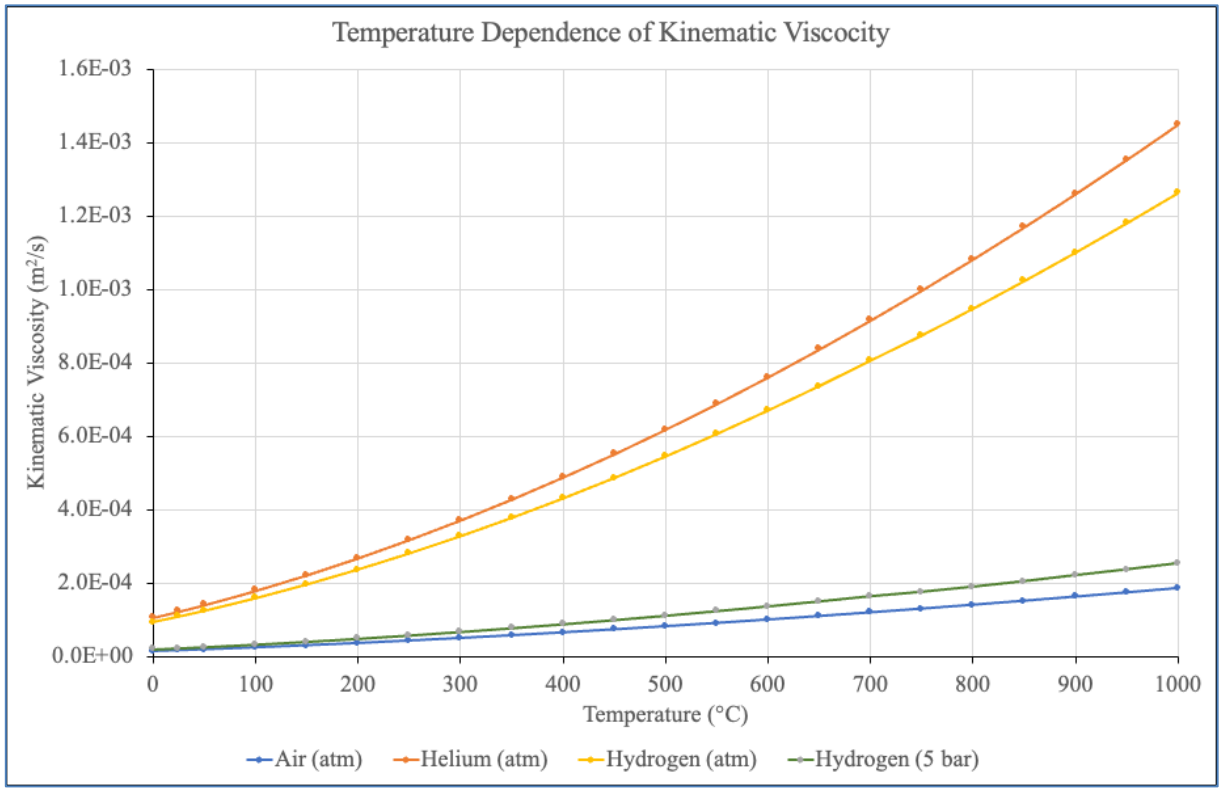

Figure 24: Temperature Dependence of Kinematic Viscosity

3.5.3 Temperature Dependence of Ar and U_{mf}

In order to determine the Archimedes Number and the minimum fluidization velocity following Equations 2.13 – 2.15, two variables, the particle diameter and the particle density, must be assumed. For this purpose, the particle density is assumed to be the one of iron ore, which corresponds to 4300 kg/m^3. In addition, a particle diameter of 0.5 mm is used for the calculations.

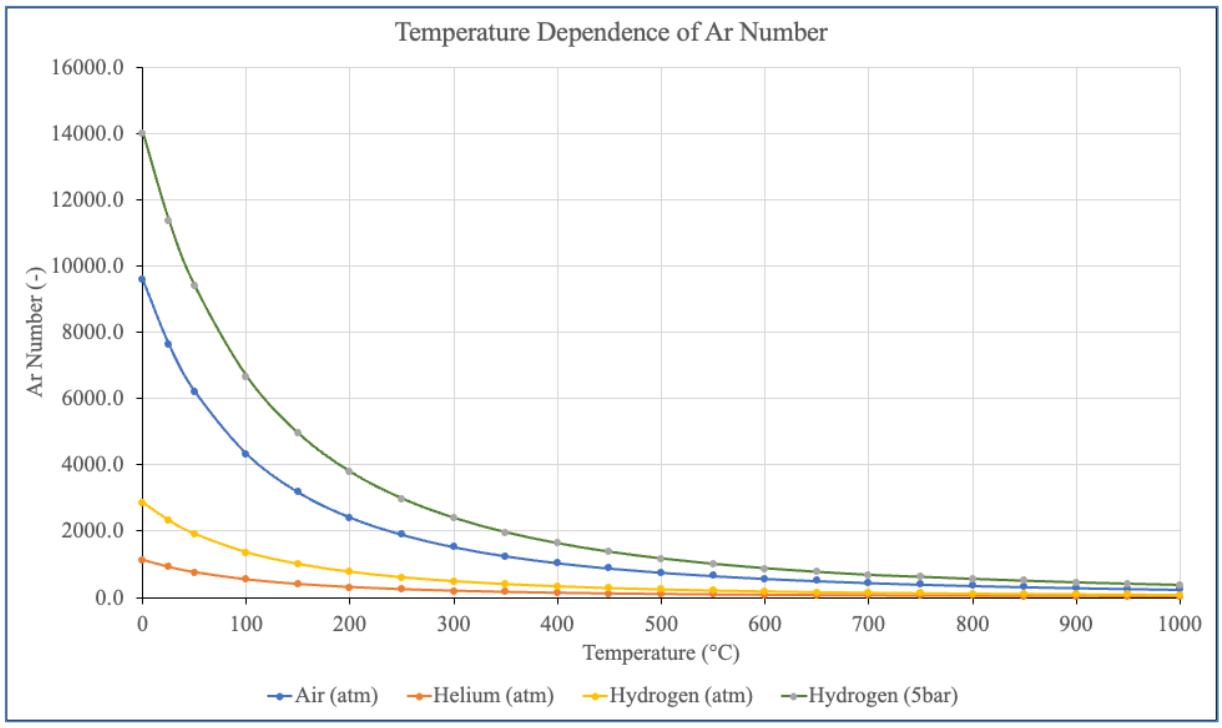

Figure 25: Temperature Dependence of Archimedes Number for an iron ore diameter of 0.5 mm

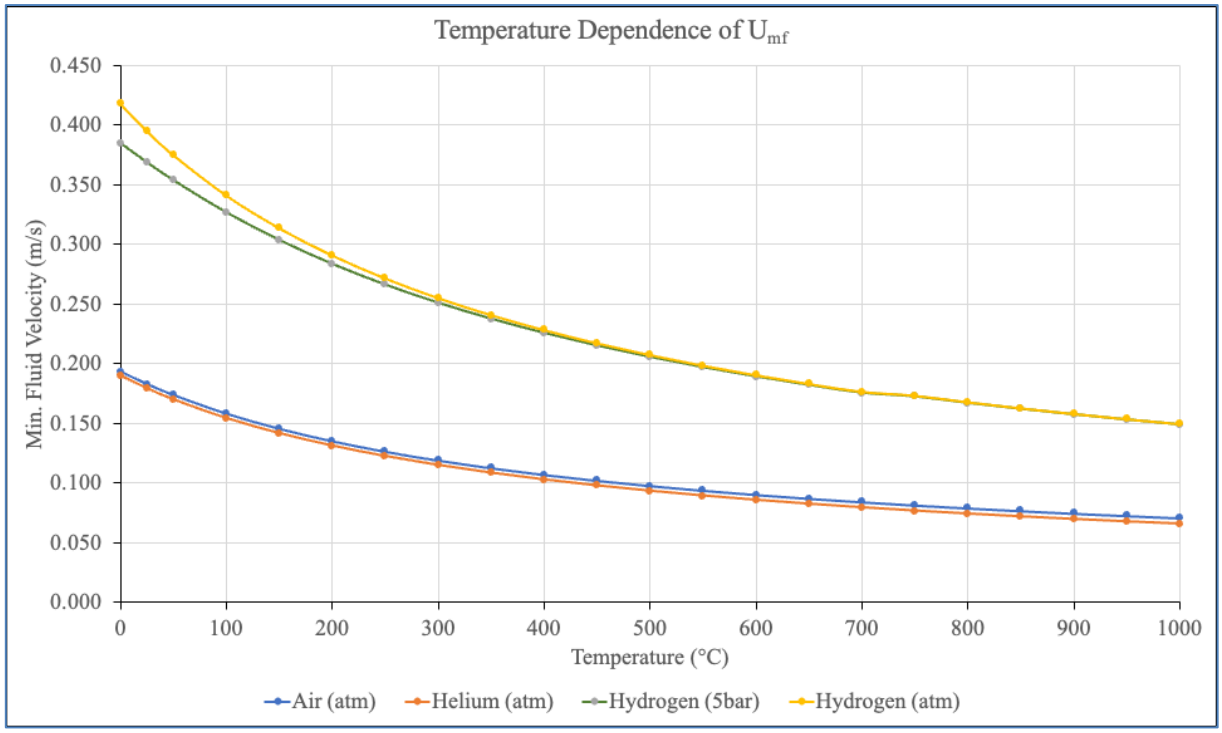

Figure 26: Temperature Dependence of Minimum Fluidization Velocity for an iron ore diameter of 0.5 mm

As seen in Figure 25, the Archimedes number for helium is one tenth of the Archimedes number for air, which can be explained by the same proportions found for the densities of helium and air. This is to be expected since the density factors into the numerator and is therefore in direct proportion to the Archimedes number. The Archimedes number of hydrogen at atmospheric pressure is comparable with the one for helium, especially with increasing temperature.

As seen from the curves in Figure 25, the viscosity does not seem to have as big of an effect on the Archimedes number as the density.

As can be deducted from Figure 26, the minimum fluidization velocity decreases with an increase in temperature. The minimum fluidization velocity observed for helium is most comparable with the one obtained for air. Since the curves for hydrogen at atmospheric pressure, as well as at 5 bar almost completely overlap, it can be assumed that the minimum fluidization velocity is not dependent on the pressure. The minimum fluidization velocity of helium and hydrogen are not as comparable as the ones of helium and air. Summing up, the minimum fluidization velocity is reduced by dropping the operation temperature.

3.6 Similarity of Helium and Hydrogen

According to Glicksman, four different parameters for cold and hot model tests should be identical in order to achieve similarity between cold and hot model. The four parameters are as followed:

1. Reactor geometry
2. Density proportions (ρ_p/ρ_g)
3. Reynolds Number
4. Froude Number

In addition to these parameters, the Archimedes number can also be applied for similarity purposes due to its correlation with Reynolds number and Froude number, as seen in the following equation:

$$\frac{Ar}{Re^2} = \frac{\Delta\rho/\rho_g}{Fr} \tag{2.50}$$

Equation 2.50 can be rewritten as:

$$Ar = \frac{\Delta\rho/\rho_g}{Fr} \cdot Re^2 = \left(\frac{\rho_p}{\rho_g} - 1\right) \cdot \frac{Re^2}{Fr} \tag{2.51}$$

Equation 2.51 shows that, if the four parameters given by Glicksman as similarity conditions for cold and hot model are equal, the Archimedes number should be identical as well.

Firstly, the reactor geometry for both cold and hot model is the exact same. Assuming pure hydrogen as the fluid in the hot model, the four Glicksman parameters are listed in Table 10 and Table 11, assuming iron ore and then silica sand as the fluidized particle.

Table 10: Theoretical data for similarity parameters assuming iron ore as particle; calculation as in Appendix

		Cold model conditions			Hot model conditions
		Helium	**Air**	**Hydrogen**	**Hydrogen**
Reactor material	-	Plexiglas			Steel
Temperature (T)	°C	25			700
Pressure (p)	bar	1.013			5
Fluid Density (ρ_g)	kg/m³	0.16	1.17	0.08	0.12
Particle Density (ρ_p)	kg/m³	4300			4300
ρ_p/ρ_g	-	26644	3680	52230	34552
Dynamic Viscosity (μ)	10^{-5}Pas	1.98	1.84	0.89	2.03
Kinematic Visosity (ν)	10^{-5}m²/s	12.3	1.58	10.8	16.3
Particle Diameter (d_p)	mm	0.5			0.5
Minimum Fluidization Velocity (U_{mf})	m/s	0.18	0.18	0.40	0.18
Operational Velocity (u)	m/s	0.54	0.55	1.19	0.53
Archimedes Number (Ar)	-	911	7636	2312	670
Reynolds Number (Re)	-	1.64	13.03	4.11	1.21
Froude Number (Fr)	-	79	82	383	75

Table 11: Theoretical data for similarity parameters assuming silica sand as particle; calculation as in Appendix

		Cold model conditions			Hot model conditions
		Helium	**Air**	**Hydrogen**	**Hydrogen**
Reactor material	-	Plexiglas			Steel
Temperature (T)	°C	25			700
Pressure (p)	bar	1.013			5
Fluid Density (ρ_g)	kg/m³	0.16	1.17	0.08	0.12
Particle Density (ρ_p)	kg/m³	2600			4300
ρ_p/ρ_g	-	16110	2225	31581	20892
Dynamic Viscosity (μ)	10^{-5}Pas	1.98	1.84	0.89	2.03
Kinematic Visosity (ν)	10^{-5}m²/s	12.3	1.58	10.8	16.3
Particle Diameter (d_p)	mm	0.5			0.5
Minimum Fluidization Velocity (U_{mf})	m/s	0.12	0.13	0.27	0.12
Operational Velocity (U)	m/s	0.37	0.38	0.82	0.36
Archimedes Number (Ar)	-	669	5602	1696	492
Reynolds Number (Re)	-	1.21	9.71	3.04	0.89
Froude Number (Fr)	-	35	37	172	34

The minimum fluidization velocity is calculated to make an appropriate assumption about the

operational velocity, which is here assumed as three times the minimum fluidization velocity. The Reynolds number is calculated using the assumed operational velocity. For comparison purposes, the data for air as fluid is given as well. The hot model operates at temperatures of 600-700 °C and is subjected to a pressure of 5 bar. For the purpose of calculating the similarity, a temperature of 700 °C and a pressure of 5 bar is assumed for hydrogen as hot model conditions. As a reference value, the parameters for hydrogen are also calculated at atmospheric pressure and room temperature of 25 °C. The Froude number would be identical for same fluid velocity and particle diameter as well as for variation of both parameters. When comparing helium and hydrogen at cold model conditions, it is evident that the densities are in the same order of magnitude. However, the dynamic viscosities of helium and hydrogen at cold model conditions shows a greater deviation than helium and air. The opposite can be said for the kinematic viscosities. Even though the densities and dynamic viscosities of helium at room temperature (25°C) and hydrogen at hot model conditions are similar, they are not identical. As a result, the Reynolds Number cannot be equal either. The Reynolds number of helium is comparable to the one of hydrogen at hot model and cold model conditions, the Archimedes number of helium corresponds better with the Archimedes number obtained for hydrogen at hot model conditions. In contrast to helium, the data for air shows another order of magnitude altogether in comparison to hydrogen´s properties, whether for the density proportion or for the Reynolds Number. It can also be said that the Archimedes number obtained by assuming iron ore as the fluidized particle, is larger than the one calculated with silica sand, which is a result of the high particle density of iron ore.

All in all, it can be said that helium does not thoroughly fulfill Glicksman´s criteria, but for this thesis' purpose helium´s properties come very close to the ones obtained for hydrogen, which is why it is used as fluidization gas for the cold model experiments.

4 Results

4.1 Validation of Experimental Setup

In order to validate the designed experimental setup, tests are run with quartz sand of three different particle distribution sizes with air as fluidization gas and no attached internal cyclone. These are chosen to be identical to the ones used by Walla in [49]. For determination of the average diameter, a sieve analysis is performed for all three samples as listed in Table 12. Figure 27 - Figure 29 show the particle distribution of samples A1 - A3.

Table 12: Validation samples

Sample Name	Paricle Distribution Size (Sand)	Average Diameter
	mm	mm
A1	0.1-0.2	0.151
A2	0.25-0.5	0.369
A3	0.5-1	0.796

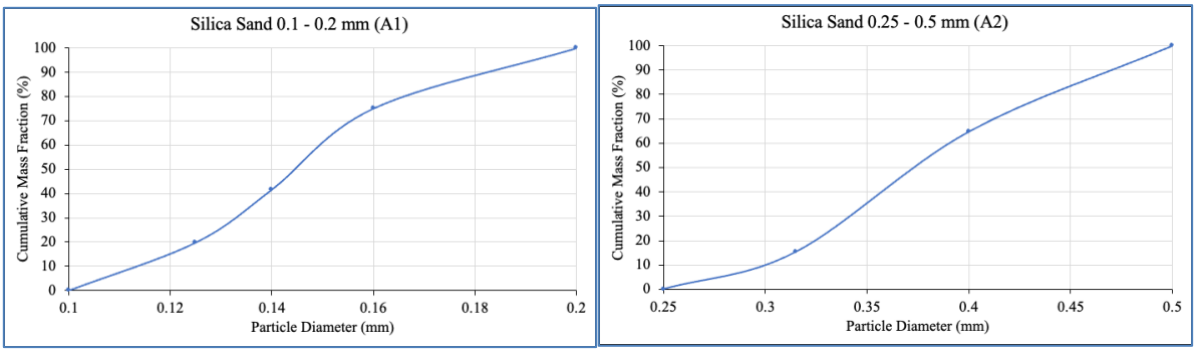

Figure 27 and Figure 28: Particle size distributions for Samples A1 and A2

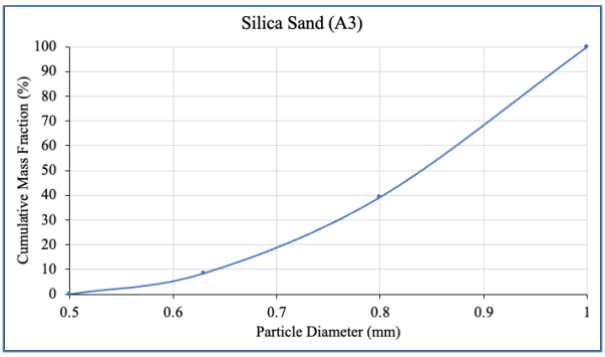

Figure 29: Particle size distribution for sample A3

The pressure loss diagrams for samples A1 and A3 are depicted in Figure 30 and Figure 31.

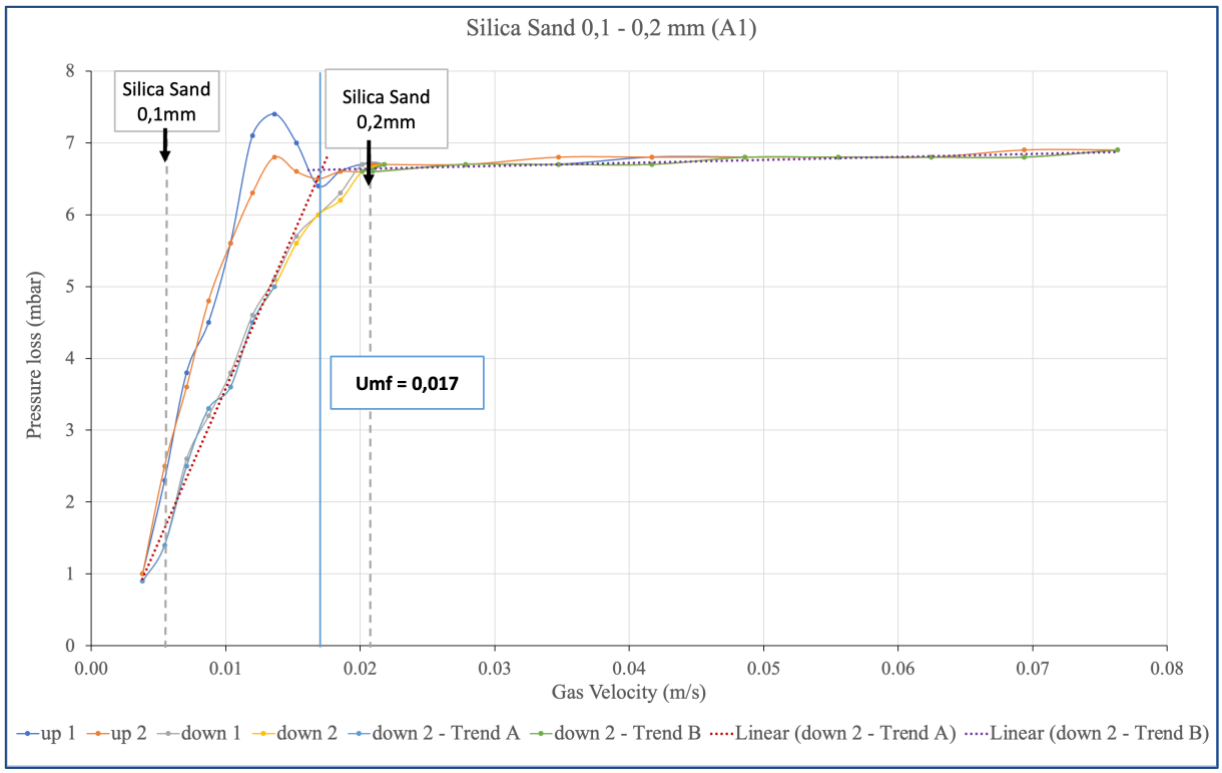

Figure 30: Pressure loss diagram for sample A1

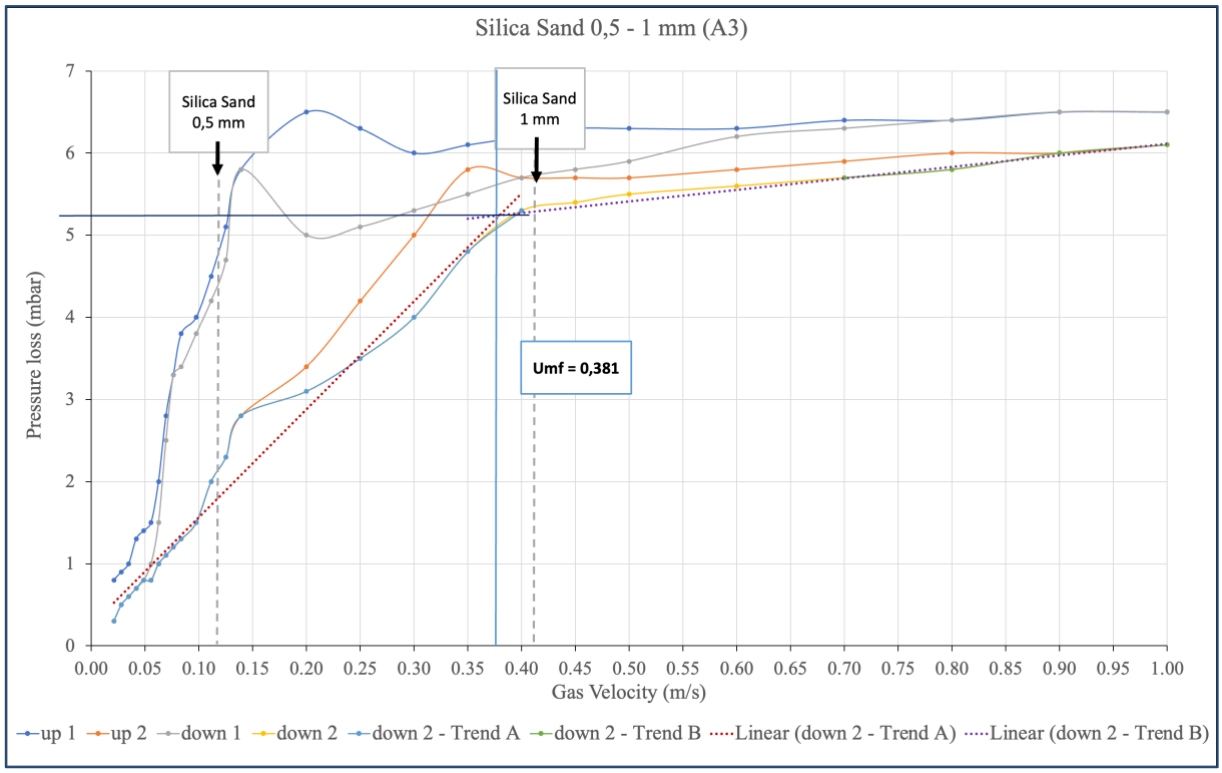

Figure 31: Pressure loss diagram for sample A3

When comparing the upward and downward measurements of sample A1 it is apparent, that the pressure linearly increases at first, reaching a maximum, before decreasing again until hitting an approximate constant value. The overshooting can be explained by the compaction of the

particles, when these are filled into the cold mode. To overcome the compaction, a higher pressure is documented, where the compressed state of the particles is loosened up. The fluidization point is determined by dividing the function into two sections, one linear section and one almost constant section. The fluidization point corresponds to the intersection point of two tangents applied to the two aforementioned sections. The theoretical minimum fluidization velocity values for the minimum and the maximum particle size are depicted in the graph, the fluidization point lies within both points.

The same overshooting behaviour observed for sample A1 is seen for sample A3. Although both upward measurements do not show the same increase, the downward measurements are roughly similar.

Table 13: Calculation Parameters

Calculation Parameters			
Particle Density	**Gas density**	**Gas viscosity**	**Sphericity**
kg/m^3	kg/m^3	10^{-5} Pa s	-
2600	1.164	1.838	0.8

Table 14: Test Results

Sample Name	**d_p**	**Ar**	**$U_{mf,theoret.}$**	**$U_{mf,exp.}$**	**Deviation U_{mf}**	**Δp_{exp}**	**$\Delta p_{theoret.}$**	**Deviation Δp**
	mm	-	m/s	m/s	%	Pa	Pa	%
A1	0.15	154.85	0.0122	0.0171	28.81	670	691.86	3.16
A2	0.37	2267.67	0.0719	0.0850	15.41	510	614.99	17.07
A3	0.80	22725.9	0.2904	0.3809	23.75	525	614.99	14.63

As a reference, the minimum fluidization velocity is determined by theoretical calculation using the calculation parameters listed in Table 13. The results are given in Table 14 and Table 15. The experimental minimum fluidization velocity is comparable to the results obtained in [49]. Even though the velocity deviation for sample A3 seems relatively high, the big difference of 0.1 mm in particle diameter needs to be considered as well. Additionally, the experimental values correspond slightly better to the theoretical values obtained by calculation.

Table 15: Validation results

Sample Name	d_p	Ar	$U_{mf,theoret.}$	$U_{mf,exp.}$	Deviation $U_{mf,exp}$ - $U_{mf,theoret.}$	$U_{mf,exp.}$[49]	d_p [49]	Deviation $U_{mf,exp}$
	mm	-	m/s	m/s	%	m/s	mm	%
A1	0.15	154.85	0.0122	0.0171	28.81	0.0150	0.12	18.63
A2	0.37	2267.67	0.0719	0.0850	15.41	0.0985	0.32	27.04
A3	0.80	22725.9	0.2904	0.3809	23.75	0.4200	0.70	30.86

4.2 Calibration of Rotameter with a Gas Meter

Due to the inaccuracy of the rotameter and the suitability of the rotameter for air, the flowrate was verified and corrected by conducting flowrate measurements with a gas meter.

4.2.1 Air

For every rotameter, four or five flowrate points are chosen and measured. The values are fitted by a linear regression, which is applied to every pressure loss measurement. As seen in Figure 32, the accuracy of the rotameters decreases with increasing flowrate. Particularly Rotameter 4 seems to show significant inaccuracies of up to 55 %, when reaching a flowrate of 40 L/min.

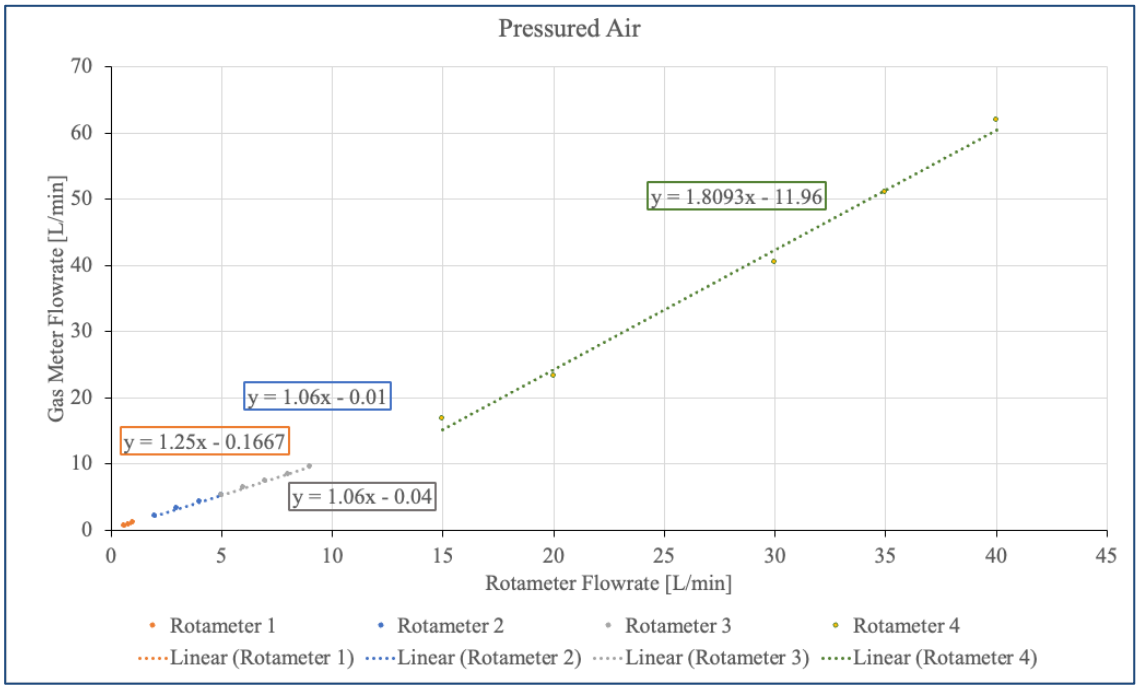

Figure 32: Correction of Rotameter Flowrate by Gas Meter (Air)

4.2.2 Helium

When utilizing helium as a fluidization gas, the flowrate measured by the gas meter is approximately double the volume flow of the flowrate displayed at the rotameter, which is expected since the rotameters are designed for air. As seen in Figure 33, the accuracy for Rotameter 4 decreases with rising flowrates, the regression is only a rough approximation.

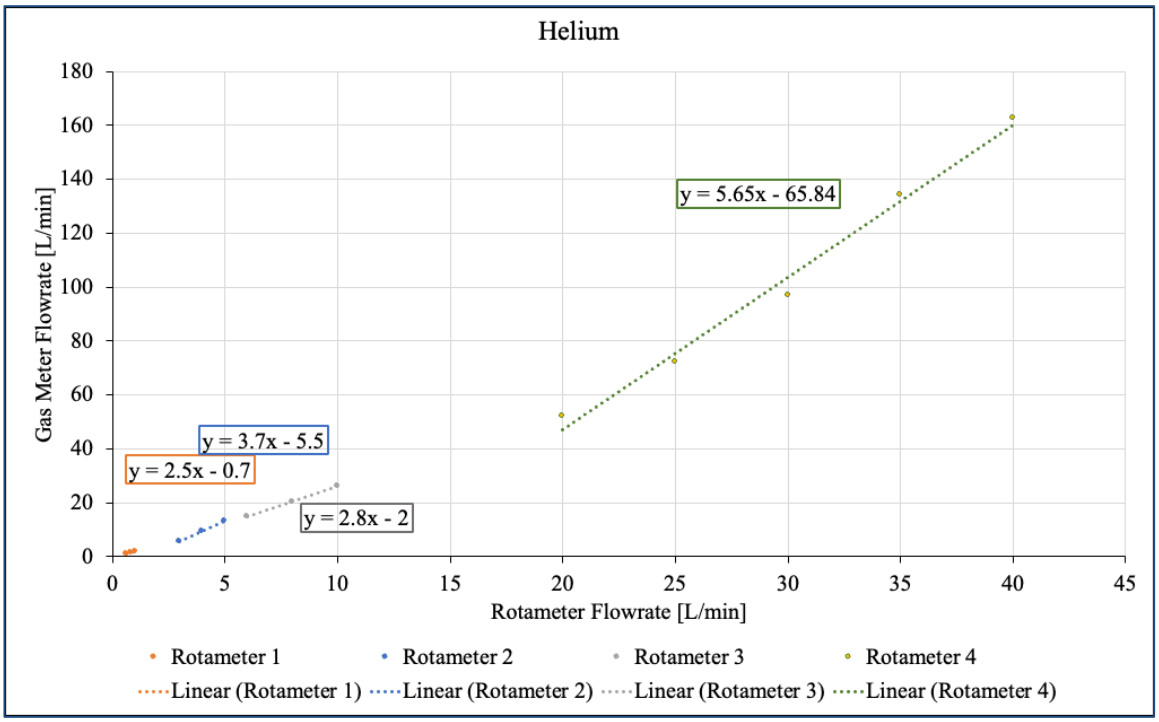

Figure 33: Correction of Rotameter Flowrate by Gas Meter (Helium)

4.3 Particle Distribution Curves (Sieve Analysis)

4.3.1 Particle Distribution of Silica Sand

As a result of the sieve analysis of the silica sand of four different particle size ranges (as listed in Table 16), a particle size distribution is generated.

Table 16: Silica Sand - Particle Distribution Size

	Particle Distribution Size in mm				
Silica Sand	0.1-0.8	0.1-0.2	0.5-0.8	0.5-1	0.8-1

The visualization of particle size distributions allows for the identification of the average particle size, the minimum particle size and the maximum particle size. As an example, Figure 34 shows the particle size distribution for silica sand of a particle size range from 0.1-0.8 mm. While the average particle diameter is calculated by Equation 2.2, it can also be estimated by

analyzing the particle size distribution curve, since the average particle size corresponds to the particle size at a cumulative mass fraction of 50 %. The results for the calculation of the average particle size are found in Table 17. Due to the unavailability of a test sieve for an analysis for the silica sand of a particle size range of 0.8-1 mm, the median was assumed as the average diameter.

Table 17: Sieve analysis result - average diameter (silica sand)

Determination of Mean Particle Diameter by Sieve Analysis					
Particle Distribution Size	mm	0.1-0.8	0.1-0.2	0.5-0.8	0.5-1
Mean Particle Diameter ($\overline{d_p}$)	mm	0.305	0.137	0.616	0.720

It can be deduced from the curve in Figure 34 that half of the analyzed particles have a particle diameter of less than approximately 0.37 mm. However, the calculated average particle diameter for silica sand of a particle size range of 0.1-0.8 mm is equal to 0.305 mm. This deviation can be explained by the big range of particle size and the limited number of allowed sieves for the sieve analysis. Between particle size of 0.25 mm and 0.5 mm only one test sieve was used, leading to a less accurate curve between those points.

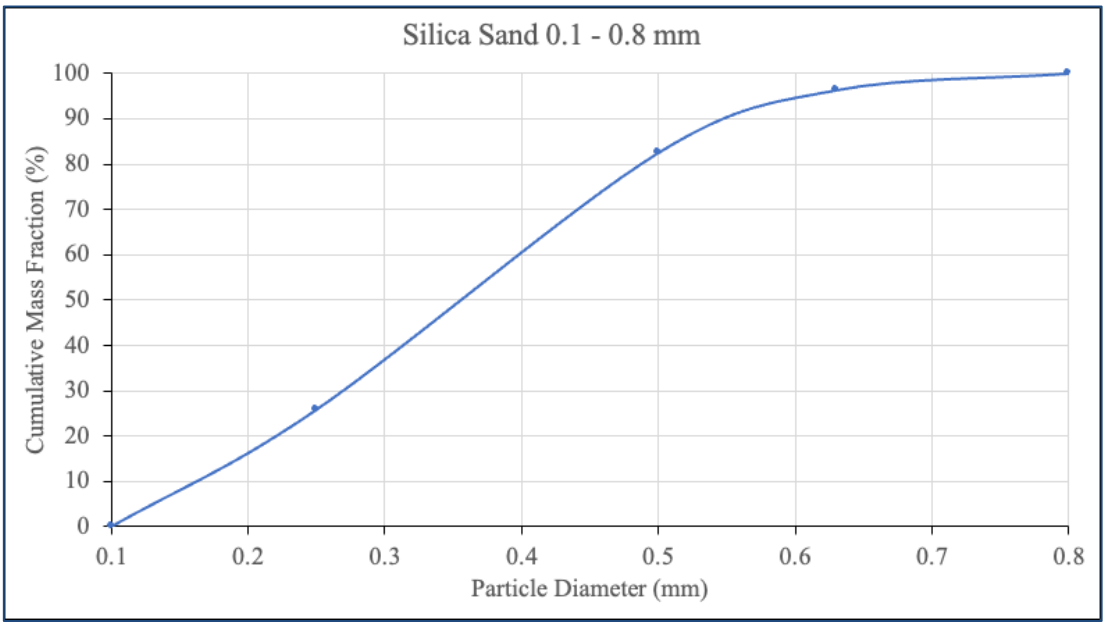

Figure 34: Particle size distribution for silica sand of a particle size range 0.1-0.8 mm

For comparison purposes, the particle size distribution of a smaller particle size range of 0.1-0.2 mm is depicted in Figure 35. In contrast to Figure 34, the average particle diameter deduced from Figure 35 is identical to the calculated value.

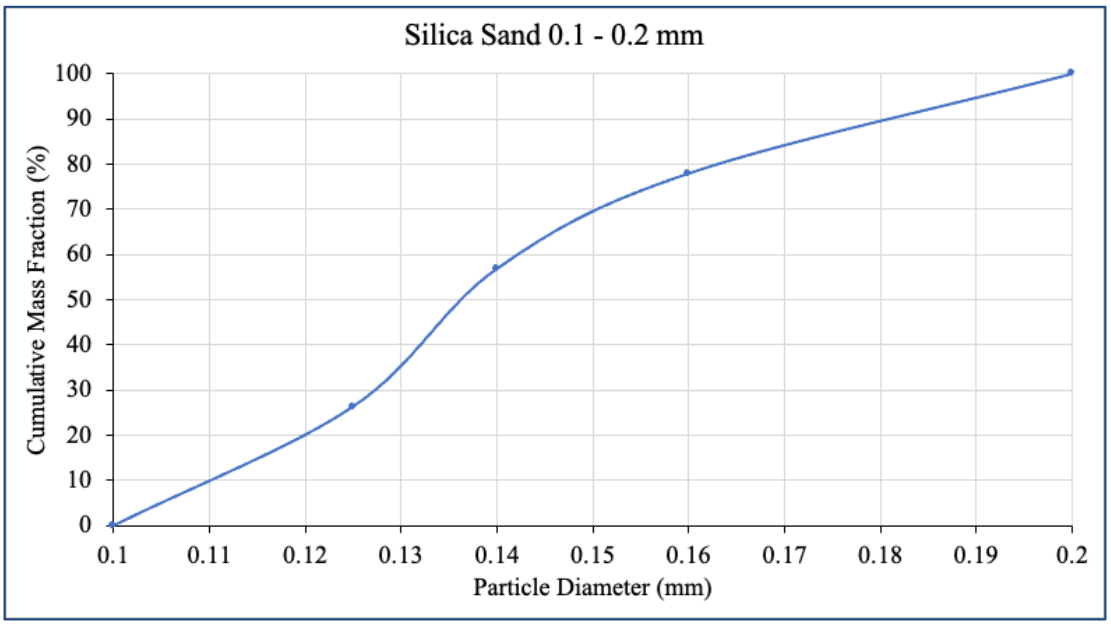

Figure 35: Particle size distribution for silica sand of a particle size range 0.1-0.2 mm

In order to show the fluid – dynamic similarities of helium and hydrogen at atmospheric pressure and room temperature (25 °C), the Archimedes Number is calculated for silica sand of the various particle size ranges and displayed in Figure 36 and Figure 37. The curves show that helium as fluidization gas leads to a higher Archimedes number than hydrogen. Due to the direct proportionality of particle diameter and Archimedes number, the Archimedes number rises with increasing particle diameter, as seen in Figure 36 and Figure 37.

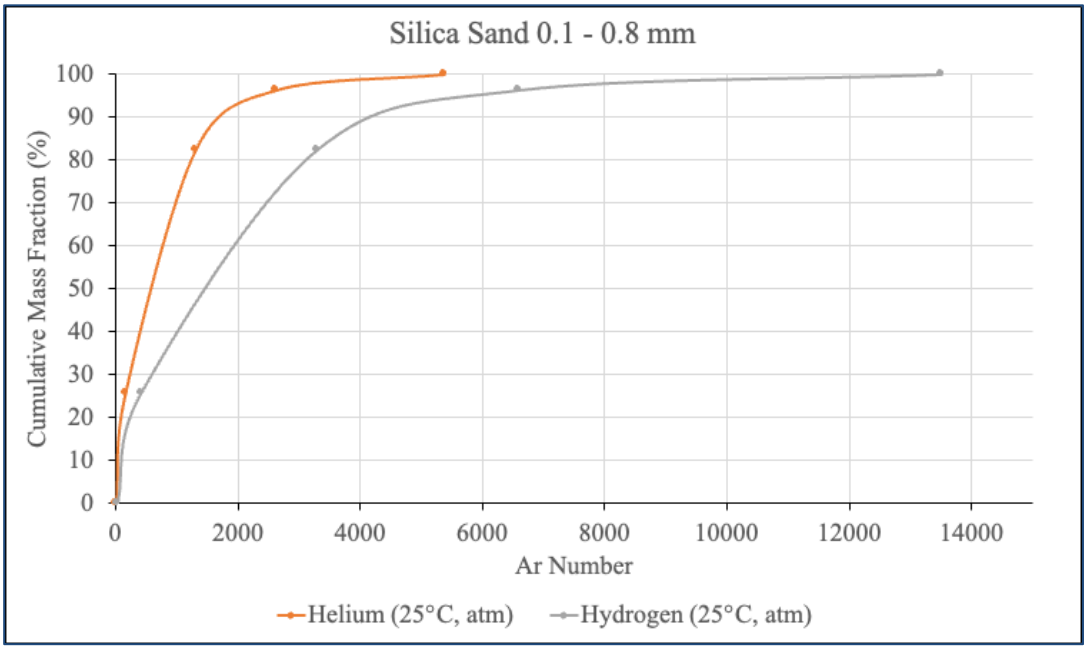

Figure 36: Ar Number Distribution for silica sand of a particle size range 0.1-0.8 mm

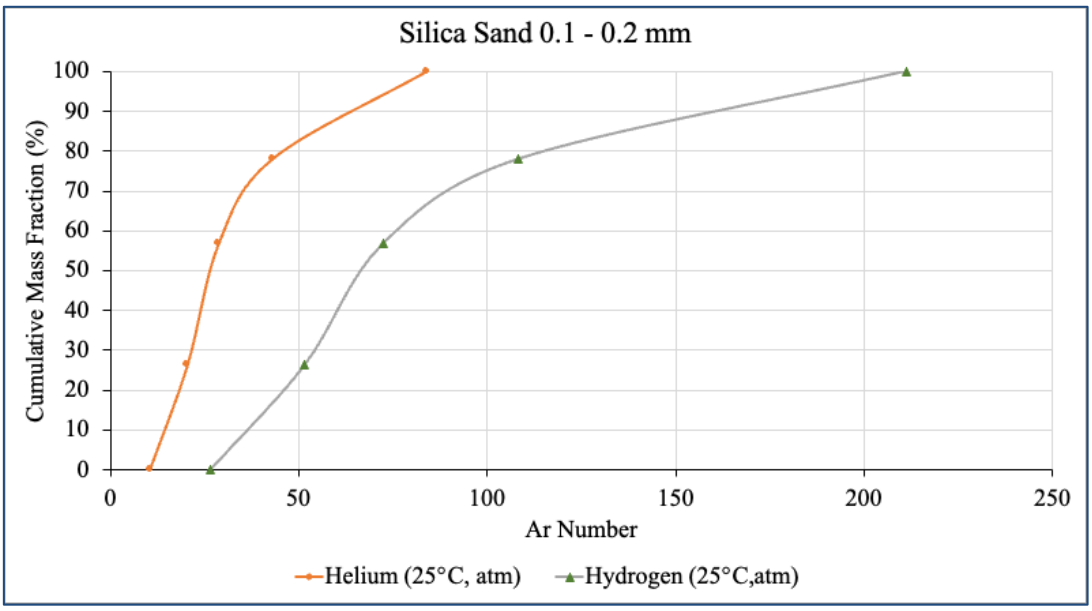

Figure 37: Ar Number Distribution for silica sand of a particle size range 0.1-0.2 mm

4.3.2 Particle Distribution of Iron Ore

Iron ore fines and iron ore with a particle size range of 0.5 – 1 mm are investigated in the experiments, as specified in Table 18.

Table 18: Iron Ore - Particle distribution size

	Particle Distribution Size in mm	
Iron Ore	0.063-0.125	0.5-1

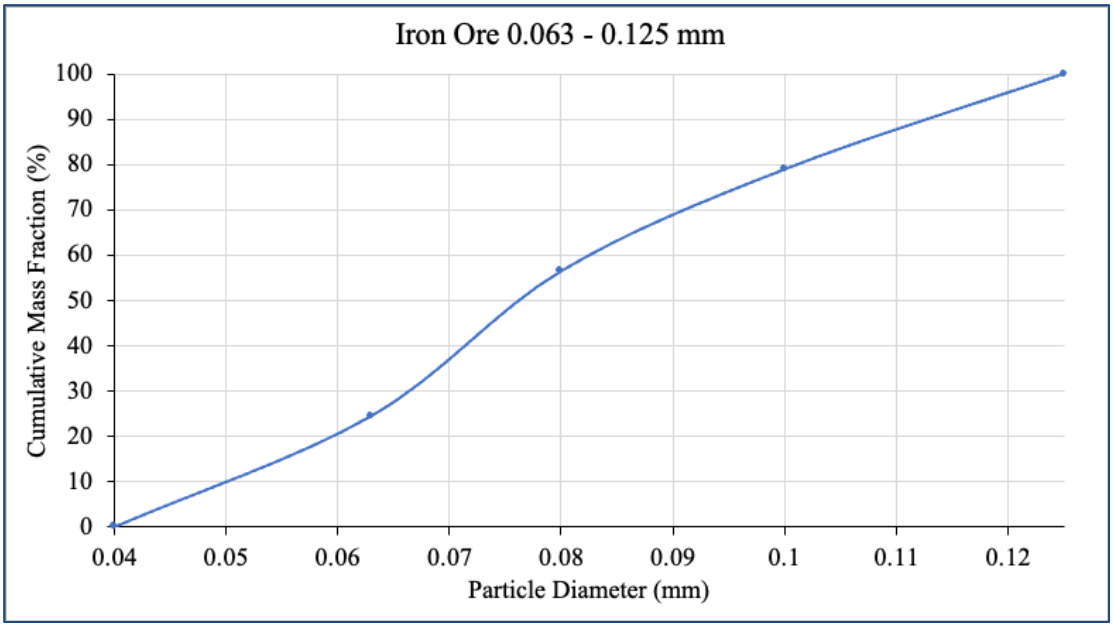

Figure 38: Particle size distribution for iron ore of a particle size range 0.063-0.125 mm

The results for the calculation of the average particle size are found in Table 19. Determining

the average diameter for both particle distribution sizes by using the distribution curve leads to approximately the same value as the calculated values.

Table 19: Sieve analysis result - average diameter (iron ore)

Determination of Average Diameter by Sieve Analysis			
Particle Distribution Size	mm	0.063-0.125	0.5-1
Mean Particle Diameter ($\overline{d_p}$))	mm	0.074	0.698

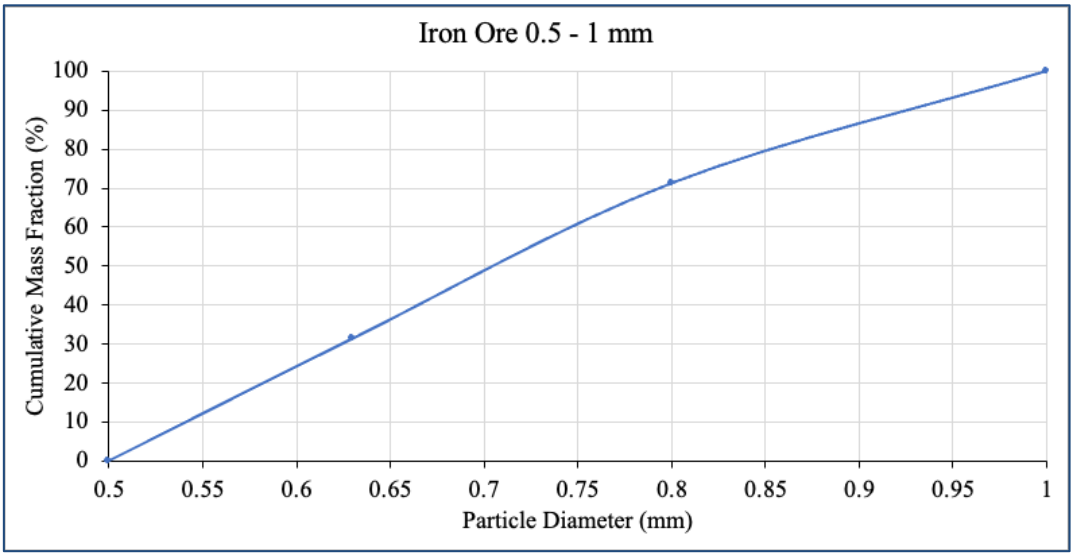

Figure 39: Particle size distribution for iron ore of a particle size range 0.5-1 mm

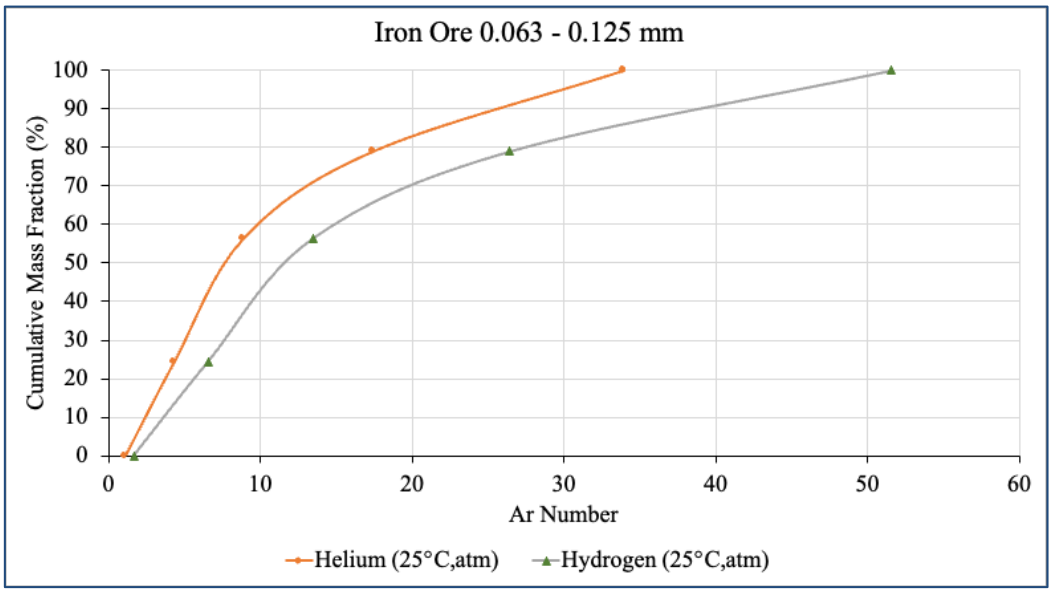

Figure 40: Ar Number Distribution for silica sand of a particle size range 0.063-0.125 mm

As seen in Figure 40 and Figure 41, the Archimedes number for helium is roughly one tenth of the value for air. The Archimedes number for both fluids is roughly in the same order of magnitude.

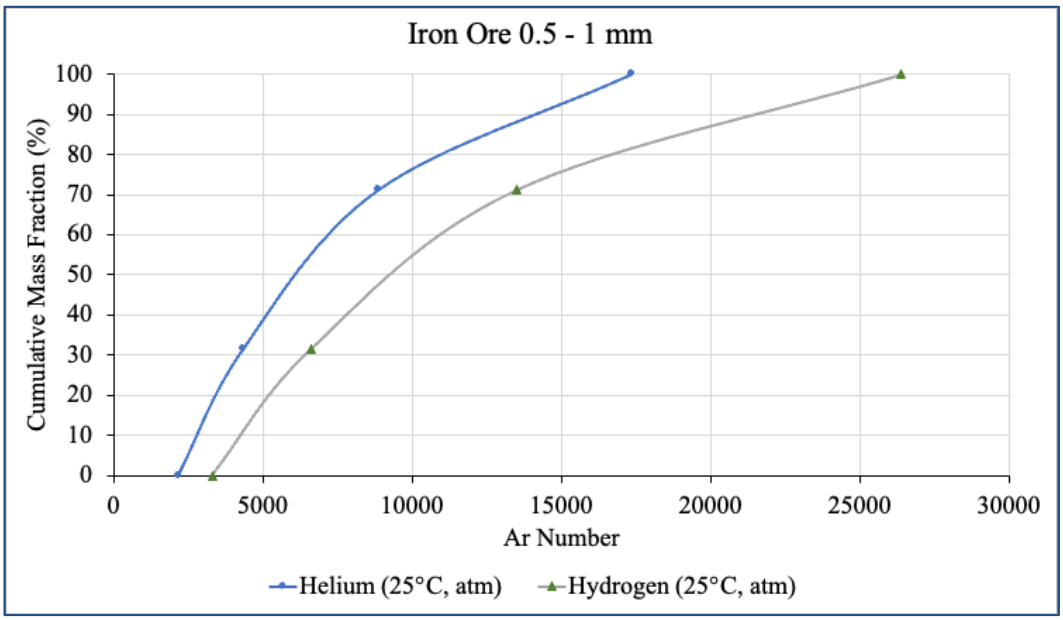

Figure 41: Ar Number Distribution for silica sand of a particle size range 0.5-1 mm

4.3.3 Particle Distribution of Sample Mixtures

This subchapter deals with the particle distributions of the sample mixtures, which are listed in Table 8.

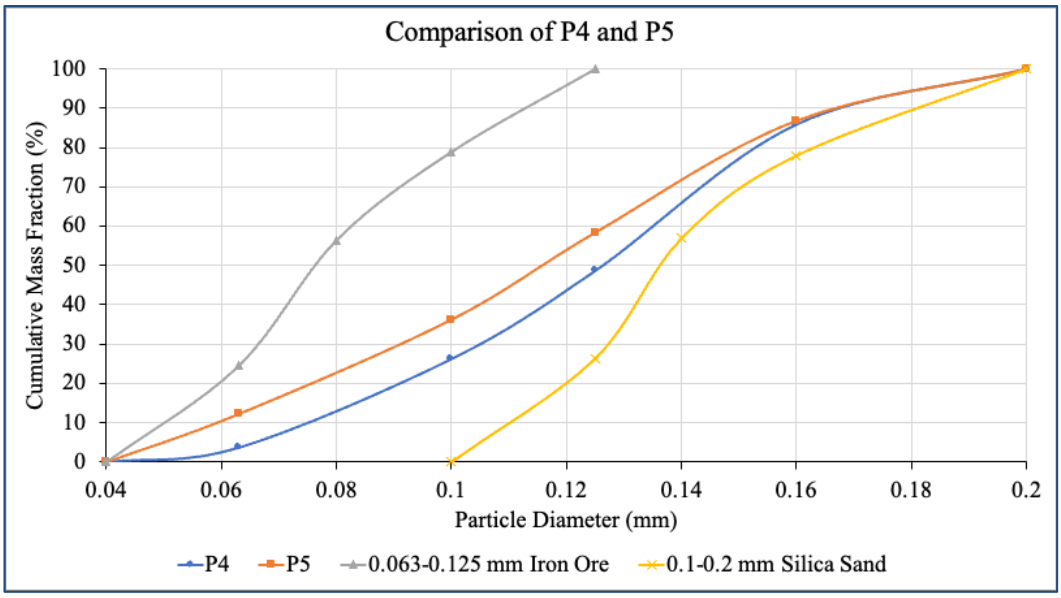

Figure 42: Particle size distributions for samples P4 and P5

Figure 42 highlights the distinctions of particle distribution for samples P4 (20 % 0.063-0.125 mm iron ore and 80 % 0.1-0.2 mm silica sand) and P5 (40 % 0.063-0.125 mm iron ore and 60 % 0.1-0.2 mm silica sand) with same particle size range, but different compositions. In addition, the particle distribution curves for pure iron ore and pure silica sand are illustrated as reference curves. As seen in Figure 42, the particle distribution curves of the samples P4 and P5 are found right between the ones for iron ore and silica sand. When increasing the iron ore

share of the mixture, the particle distribution is shifted into the direction of smaller particle sizes. However, the shape of the curve remains similar. As depicted in Figure 43, the Archimedes number for sample P5 shows slightly higher values than sample P4, which stems from the increased percentage of iron ore in the sample leading to a higher particle density of sample P5. As a result, the Archimedes number also rises due to the direct proportionality between density and Archimedes number.

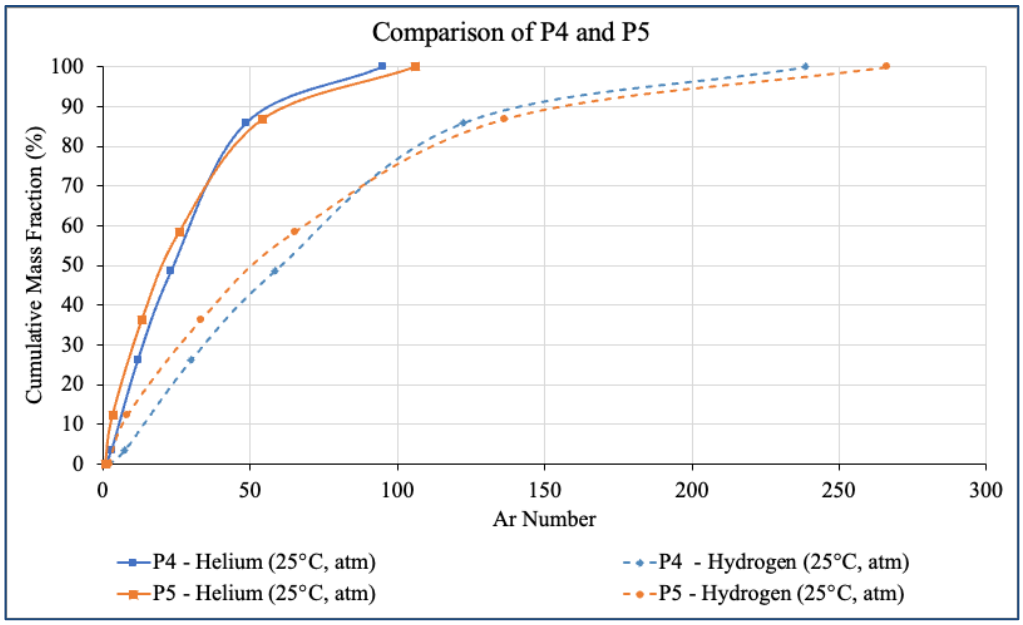

Figure 43: Ar Number distributions for samples P4 and P5

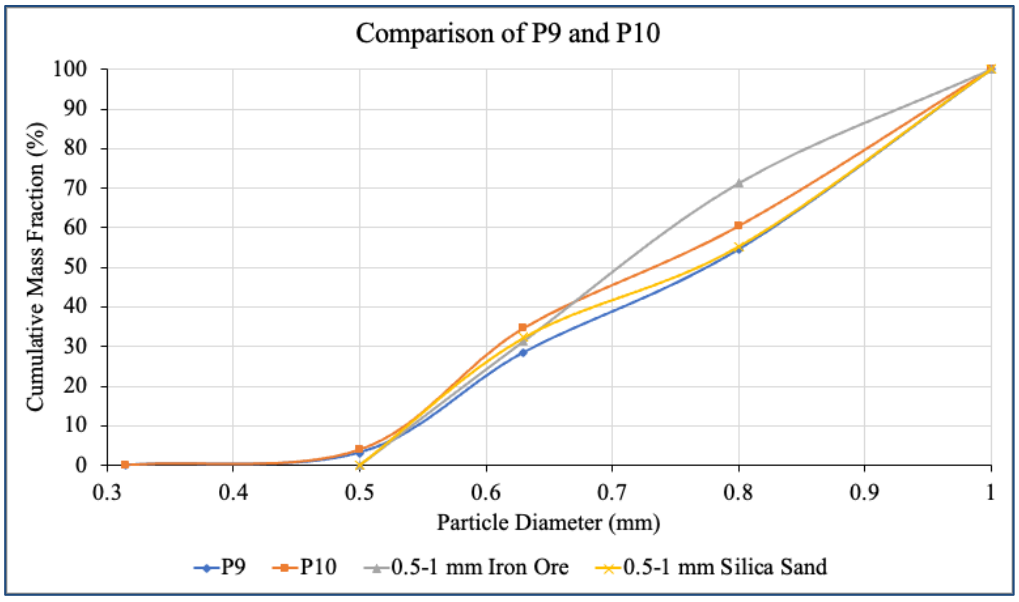

Figure 44: Particle size distributions for samples P9 and P10

As an example, for a sample mixture containing iron ore of a higher and broader particle size range, samples P9 and P10 are compared in Figure 44. Sample P10, which contains 20 % more iron ore than sample P9, only shows a slight shift of the particle distribution curve to reduced

particle size values in contrast to the one for sample P10. However, both curves mostly overlap since iron ore and silica sand in both mixtures feature comparable particle size ranges.

The mean particle diameter is calculated with Equation 2.2 and the according results are listed in Table 20.

Table 20: Sieve analysis result - average diameter (Samples P1-P10)

Sample Name	Particle Distribution Size		Mass Share		Mean particle diameter ($\overline{d_p}$)
	mm		%		mm
	Iron ore	Sand	Iron Ore	Sand	Mixture
P1	0.063 – 0.125	0.1 – 0.8	20	80	0.155
P2	0.063 – 0.125	0.1 – 0.8	40	60	0.129
P3	0.063 – 0.125	0.1 – 0.8	80	20	0.085
P4	0.063 – 0.125	0.1 – 0.2	20	80	0.113
P5	0.063 – 0.125	0.1 – 0.2	40	60	0.100
P6	0.063 – 0.125	0.5 – 0.8	20	80	0.229
P7	0.063 – 0.125	0.5 – 0.8	40	60	0.158
P8	0.5-1	0.8-1	40	60	0.767
P9	0.5-1	0.5-1	20	80	0.717
P10	0.5-1	0.5-1	40	60	0.695

When analyzing the average diameter for samples P1 through P10, it can be deduced that the average diameter decreases with higher iron ore share, confirming the conclusions drawn from the particle size distribution curves. The highest average diameter is found for sample P8.

4.4 Geldart Diagram

The Geldart diagram is chosen to demonstrate the classification of the different types of samples and is pictured in Figure 45. While samples P1-P7 fall into the Group B category, which is known for well – defined bubbling during fluidization, the coarser samples P8-P10 are part of

the Group D category, characterized by bigger particle diameter. Due to their coarser nature, the P8-P10 samples are more challenging to fluidize.

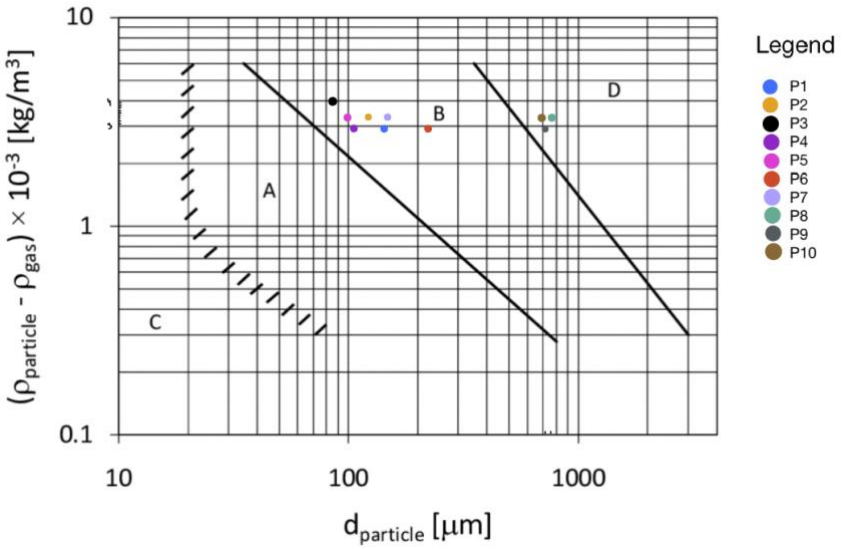

Figure 45: Geldart Diagram - Samples P1-P10 [9]

4.5 Reh and Grace Diagram – Sample Mixtures

The fluidization behaviour of the samples P1-P10 are visualized in two different state diagrams, one being the Reh Diagram, the other being the Grace diagram.

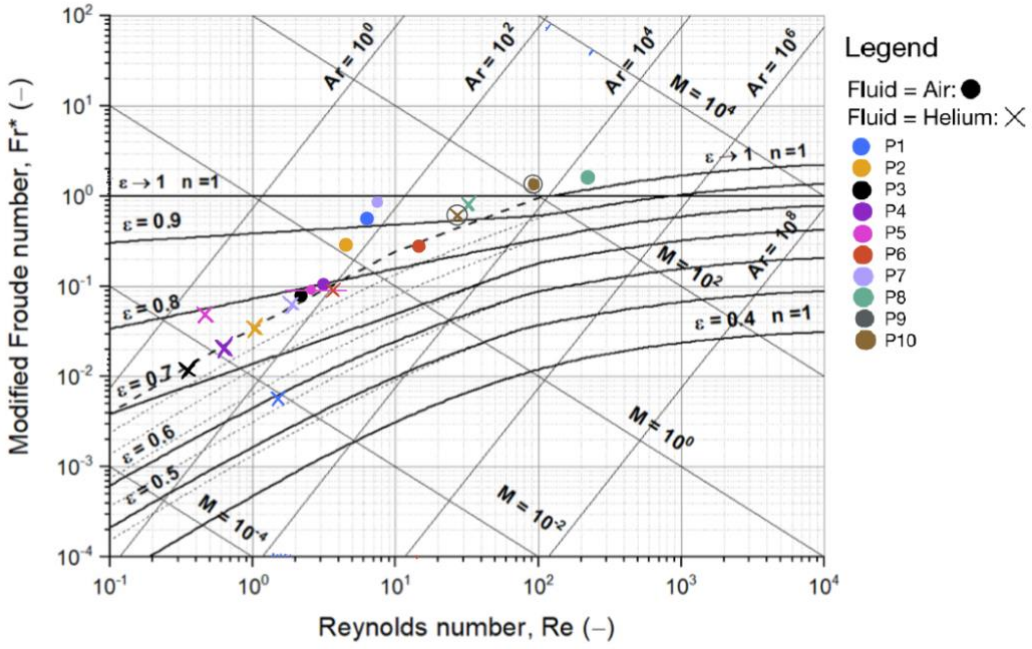

Figure 46: Reh Diagram - Samples P1-P10 for air (cross) and helium (dot) as fluid at cold model conditions; calculation assuming particle density for the mixtures P1-P10 via weighted average as in Equation 2.7 and Equations 2.45-2.49 in Chapter 2.4

As can be expected, the operation field for the samples when utilizing helium as fluidizing gas is at smaller Reynolds and Archimedes numbers, particularly due to its lower density. Samples P9 and 10, as well as P3-P5 completely or partly slightly overlap. It must be considered that only fluid dynamic forces are considered when constructing the Reh diagram. Other factors such as uneven particle distributions, interparticle forces or the reactor´s geometries are not taken into account.

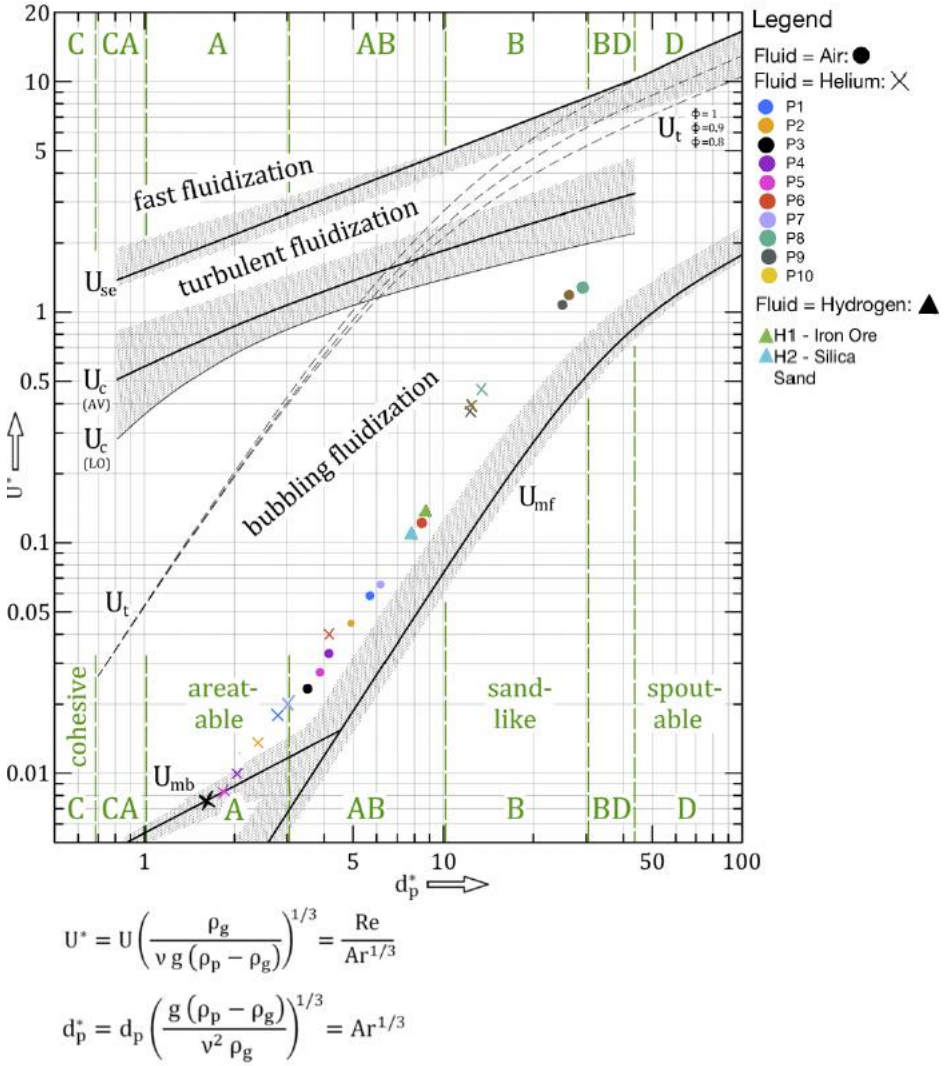

Figure 47: Grace Diagram - Samples P1-P10 for air(cross) and helium(dot) as fluid at cold model conditions; as comparison H1(hydrogen at 700°C and 5 bar with iron ore as seen in Table 10) and H2 (hydrogen at 700°C and 5 bar with silica sand as seen in Table 11) at hot reactor conditions; calculation as in the Appendix assuming a particle density for the mixtures P1-P10 via weighted average as in Equation 2.7 and U=3x U_{mf}

As mentioned in Chapter 2.4, the dimensionless gas velocity (u*) is plotted against the dimensionless particle diameter (d_p*), forming the Grace diagram. The equations needed for both state diagrams are given in Table 2 and Table 3. It is evident that the experiments P1-P10 are conducted within the domain of the bubble-forming fluidized bed, as well as the theoretical

experiments H1-H2 at hot reactor conditions. This observation is supported by the positioning of the data points on the state diagram, which fall between the lines corresponding to u_{mf} (minimum fluidization velocity) and u_t (terminal or floating velocity).

4.6 Cold Model Experiments

4.6.1 Calculation of Theoretical Minimal Fluidization Velocity and Theoretical Pressure Loss

In this chapter the calculation parameters are defined, as well as the calculation methods. In order to calculate the minimum fluidization velocity, the fluid properties and the particle properties are necessary, which are listed in Figure 48.

Particle Properties

Material	Particle Distribution Size	d_p	ρ_P	ρ_B	ε	φ
	mm	mm	kg/m³	kg/m³	-	-
Iron Ore	0.063 - 0.125	0.074	4300	2658	0.38	0.75
	0.5-1	0.698		2255	0.48	
Silica Sand	0.1 - 0.8	0.305	2600	1560	0.40	0.80
	0.1 - 0.2	0.137		1661	0.36	
	0.5 - 0.8	0.616		1614	0.38	
	0.8-1	0.900		1465	0.44	
	0.5-1	0.720		1503	0.42	

Sample Name	Particle Distribution Size		Mass Share		d_p	ρ_P	ρ_B	ε	φ
	mm		%		mm	kg/m³	kg/m³	-	-
	Iron Ore	Sand	Iron Ore	Sand	Mixture				
P1	0.063 - 0.125	0.1 - 0.8	20%	80%	0.155	2940	1570	0.47	0.80
P2	0.063 - 0.125	0.1 - 0.8	40%	60%	0.129	3280	1715	0.48	
P3	0.063 - 0.125	0.1 - 0.8	80%	20%	0.085	3960	1855	0.53	
P4	0.063 - 0.125	0.1 - 0.2	20%	80%	0.113	2940	1585	0.46	
P5	0.063 - 0.125	0.1 - 0.2	40%	60%	0.100	3280	1688	0.49	
P6	0.063 - 0.125	0.5 - 0.8	20%	80%	0.229	2940	1825	0.38	
P7	0.063 - 0.125	0.5 - 0.8	40%	60%	0.158	3280	2076	0.37	
P8	0.5-1	0.8-1	40%	60%	0.767	3280	1645	0.50	
P9	0.5-1	0.5-1	20%	80%	0.717	2940	1558	0.47	
P10	0.5-1	0.5-1	40%	60%	0.695	3280	1693	0.48	

Fluid Properties

Gas	ρ_G	μ_G
	kg/m³	10^{-5} Pas
Air	1.164136	1.8381
Helium	0.1614	1.9846

Figure 48: Calculation Parameters: bed density ρ_B as measured in Chapter 3.4, particle density ρ_p calculated via weighted average as in Equation 2.7, d_p determined by sieve analysis

The particle diameter is determined by sieve analysis, the bulk density is measured, and the fluid properties are assumed at 25 °C and atmospheric pressure. The theoretical minimum fluidization velocity is calculated by applying the approximated calculation method (Equations 2.13-2.15). In order to calculate the minimum fluidization point, the Archimedes number needs

to be determined, for which a particle density is needed. The minimum fluidization point is calculated in three ways, firstly assuming the particle density of silica sand, secondly the one of iron ore and lastly assuming a theoretical density of the mixture calculated by Equation 2.7. The bulk density is measured as described in Chapter 3.4. The theoretical pressure loss is determined using Equation 2.28. In the following chapters, the minimum fluidization point is calculated for the two components in the mixture, resulting in two reference values, which are displayed in the pressure loss diagrams.

4.6.2 Influence of Sieve on Pressure Loss

Since the pressure measurement occurs before and after the sieve tray, the pressure loss that is caused by the sieve and is also the primary contributor to pressure loss in the empty model, must be taken into consideration for further measurements. For this reason, the pressure loss of the empty cold model is measured, all four flowmeters undergo two rounds of testing, during which data is collected under both increasing and decreasing gas velocities. These measurements are conducted for air and helium separately.

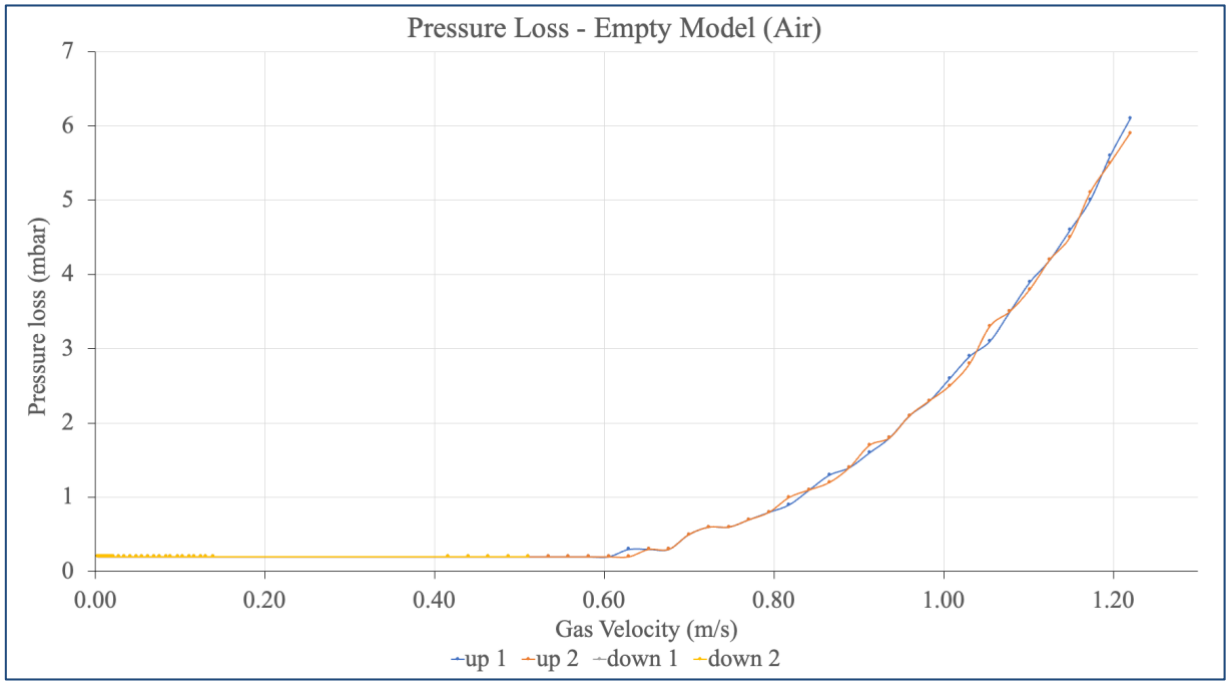

Figure 49: Pressure loss of the empty model caused by the sieve using air

Figure 49 illustrates the pressure loss with air as fluidization gas. Until a gas velocity of up to around 0.7 m/s, the pressure loss is constant at a value of 0.2 mbar. However, the pressure loss starts to exponentially grow from that point on, confirming the sieve´s impact on the pressure loss. The same trend can be seen for helium in Figure 50.

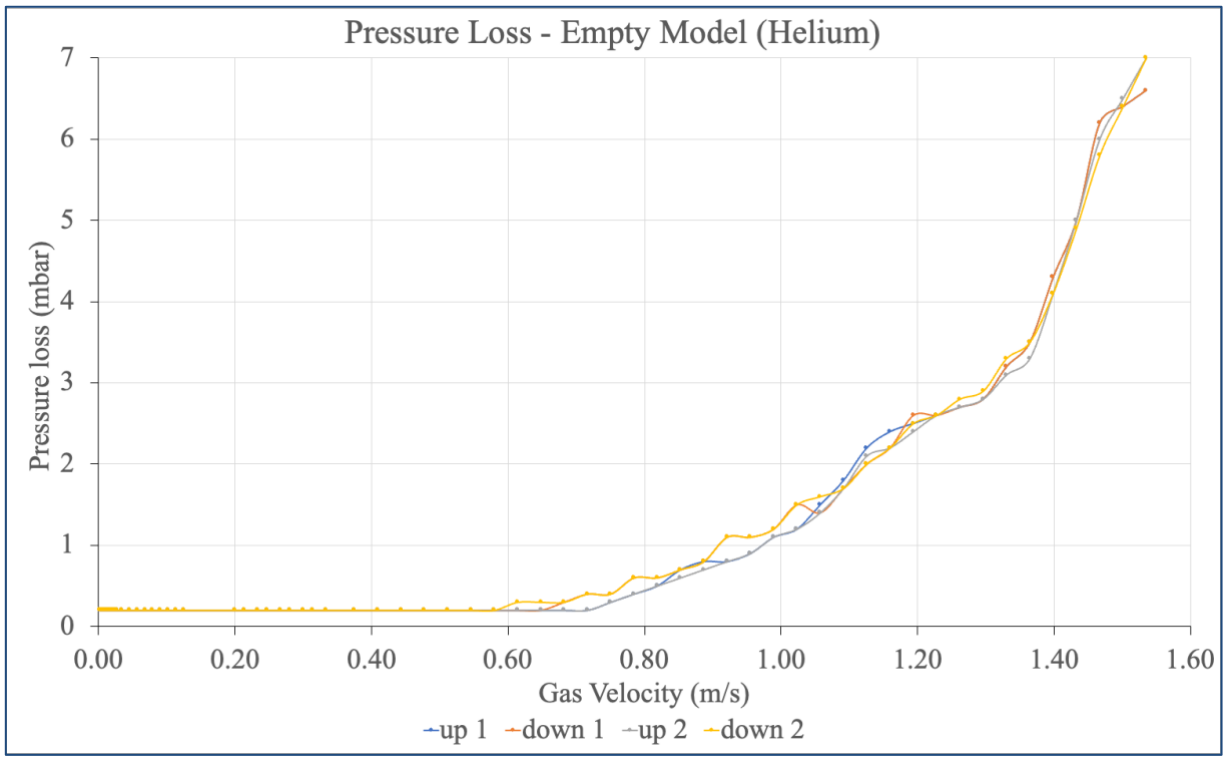

Figure 50: Pressure loss of the empty model caused by the sieve using helium

4.6.2.1 Sample P1 (80 % 0.1-0.8 mm Silica Sand/ 20 % 0.063-0.125 mm Iron Ore)

All pressure loss diagrams are corrected by subtracting the sieve´s pressure loss from the measured pressure loss values.

As seen in Figure 51, where sample P1 is fluidized by air and no cyclone is attached in the internal part of the cold model, the first upwards measurement is distinctly different from all others. This overshooting phenomenon can be explained by a compaction of the fixed bed while filling the reactor. As the reactor is filled, the finer iron ore particles have a tendency to settle into the void spaces within the silica sand and therefore the mixture requires a longer time to loosen up again. For that reason, the pressure first builds up rapidly until the compaction of the mixture is loosened up, then decreases again and finally linearly increases until reaching the fluidization point, characterized by an almost constant pressure loss. Primarily due to the overshooting, the downward measurements are chosen to determine the fluidization point.

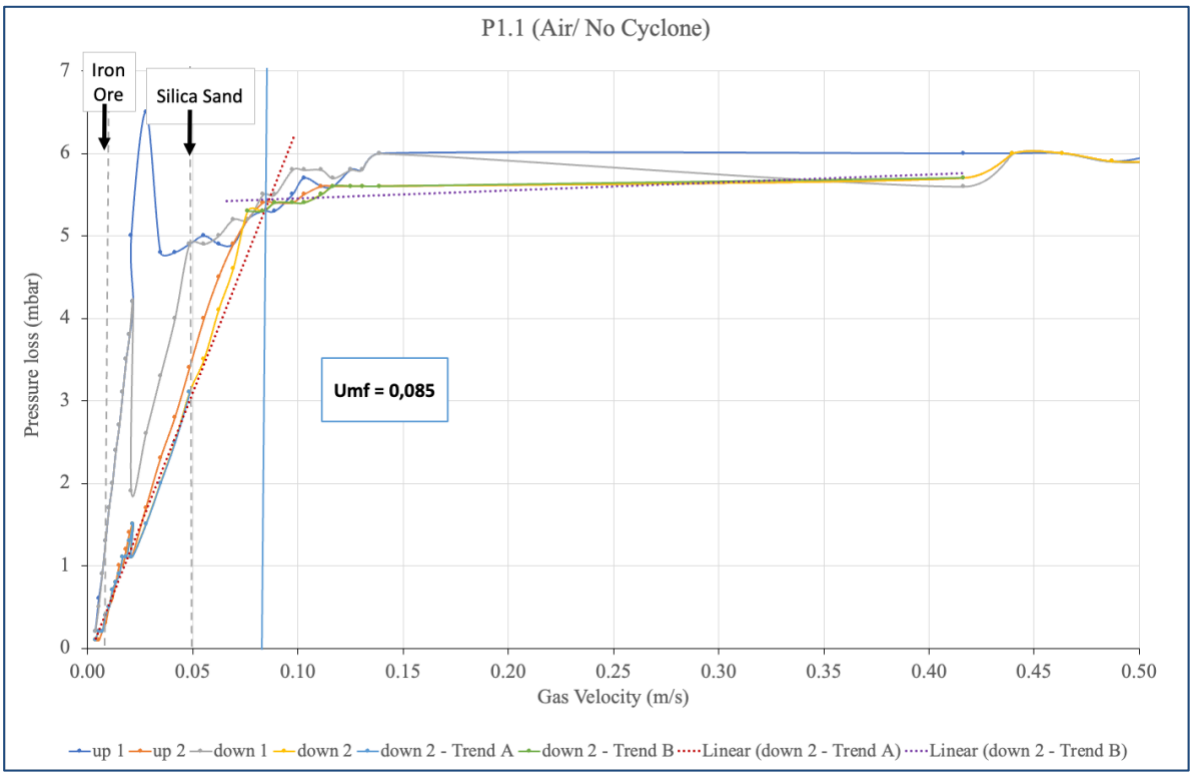

Figure 51: Pressure loss vs gas velocity of sample P1 (80 % 0.1-0.8 mm Silica Sand/ 20 % 0.063-0.125 mm Iron Ore) with air and no cyclone

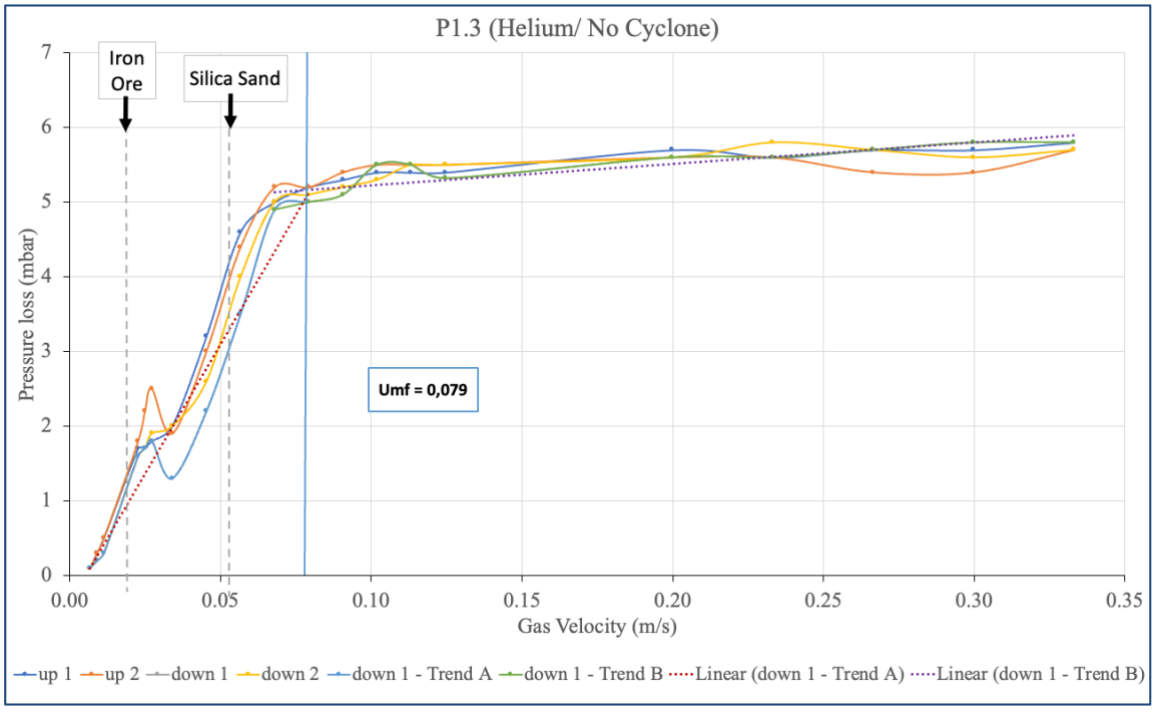

Figure 52: Pressure loss vs gas velocity of sample P1 (80 % 0.1-0.8 mm Silica Sand/ 20 % 0.063-0.125 mm Iron Ore) with air and no cyclone

Figure 52 shows the pressure loss data for sample P1, when utilizing helium as fluidization gas. Since the fixed bed is already decompacted in test P1.1, no overshooting values are seen in this graph. The two local pressure maxima at around 0.03 m/s can be explained by the switch of

Rotameter 1 to Rotameter 2. The fluidization point is at a slightly lower superficial velocity than for tests with air. However, for both experiments (P1.1 and P1.3), the fluidization point does not fall within the two reference points for iron and silica sand.

4.6.2.2 Sample P2 (60 % 0.1-0.8 mm Silica Sand/ 40 % 0.063-0.125 mm Iron Ore)

For the following samples, mostly one graph is chosen as an example, since the tests with air and helium in addition to the ones with and without an internal cyclone will be compared in other chapters. As for sample P1, the overshooting phenomenon can be observed for sample P2. However, the overshooting is not only noticeable for the first upwards measurement, but also for the second, which would mean that the particles are compacted again after turning off the gas flow. That could be explained by the higher percentage of iron ore in the mixture. Due to the finer nature of the iron ore particles and the greater mass share in the mixture, more void spaces within the silica sand can be filled. Furthermore, the following trend is evident: The higher the iron ore share in the mixture, the lower the minimum fluidization velocity. An increase in total pressure loss is also a result of the higher mass share of iron ore. In contrast to sample P1, the fluidization point here lies within the two reference values, leaning more towards the theoretical fluidization point for silica sand, which is a result of the higher mass share of silica sand than iron ore in the mixture.

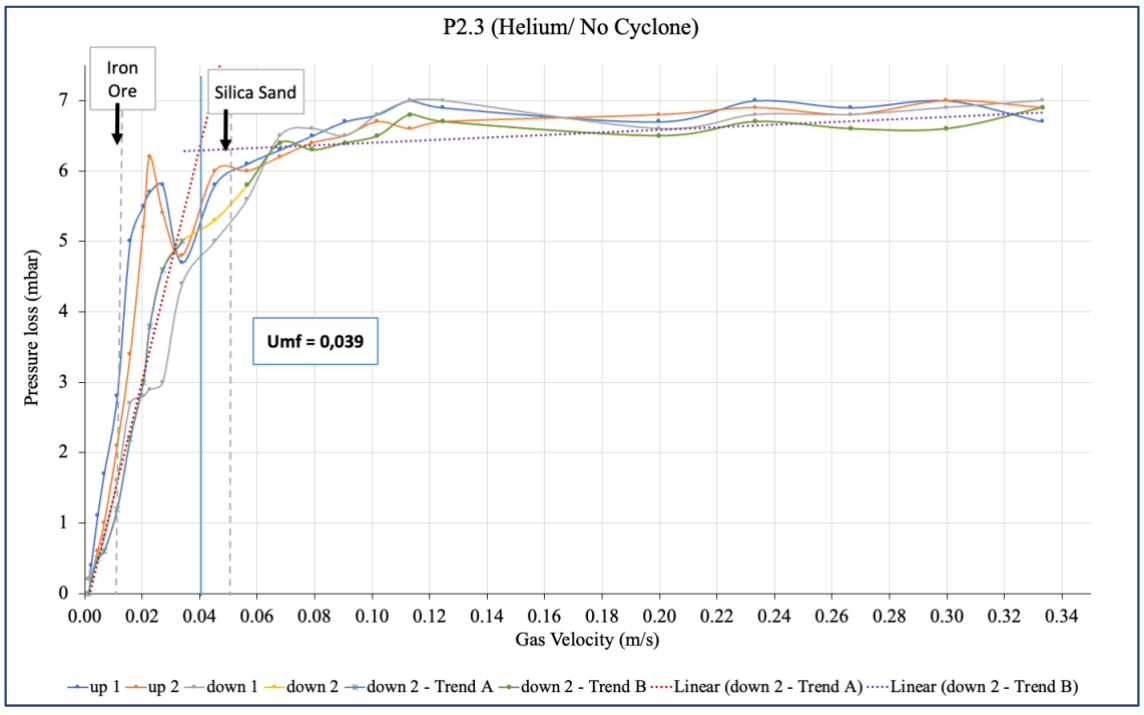

Figure 53: Pressure loss vs gas velocity of sample P2 (60 % 0.1-0.8 mm Silica Sand/ 40 % 0.063-0.125 mm Iron Ore) with helium and no cyclone

4.6.2.3 Sample P3 (20 % 0.1-0.8 mm Silica Sand/ 80 % 0.063-0.125 mm Iron Ore)

The fact that sample P3 comprises of 80 % iron ore leads to a few distinctions in the pressure loss graph, depicted in Figure 54. Firstly, the second upwards, but also downwards measurement shows a shift to higher gas velocities of almost 0.02 m/s, which corresponds to the discharge of fine iron ore particles during the test. By the reduction of fines in the mixture, the share in bigger particles, which is mostly silica sand, rises, also leading to a higher different minimum fluidization velocity. For that reason, the fluidization point was determined with the first downward measurement. If the tangents were applied to the second downward measurement, the fluidization point would be shifted by around 0.01 m/s. The mass of the fixed bed was measured after the end of the test in order to determine the mass difference. The calculation results in a bed material loss of 12 %.

The fluidization point lies exactly within the two reference points, leaning more towards the theoretical point for iron ore, resulting from a high iron ore share. As the fluid velocity rises, the pressure loss does not seem to settle at a constant value, like it does for the previous two samples. In addition, the pressure loss in Figure 55 displays intermittent spikes and fluctuations, which can be explained by the switch from bubbling fluidization to turbulent fluidization. The gradual pressure drop increases due to the intense mixing and chaotic motion of the particles.

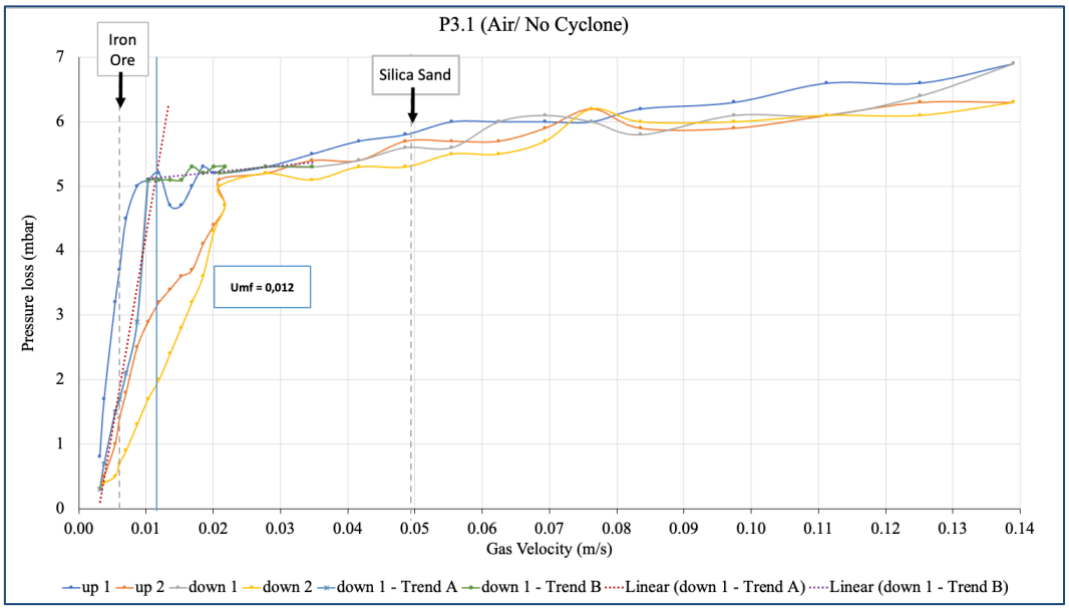

Figure 54: Pressure loss vs gas velocity of sample P3 (20 % 0.1-0.8 mm Silica Sand/ 80 % 0.063-0.125 mm Iron Ore) with air and no cyclone

The pressure loss at the fluidization point is lower than for test P3.1, which corresponds well with the measured bed material loss. The decrease in bed material consequently causes a

reduction of pressure drop. As a result of the observations made for sample P3, it was decided to focus on analyzing mixtures with only up to 40 % iron ore.

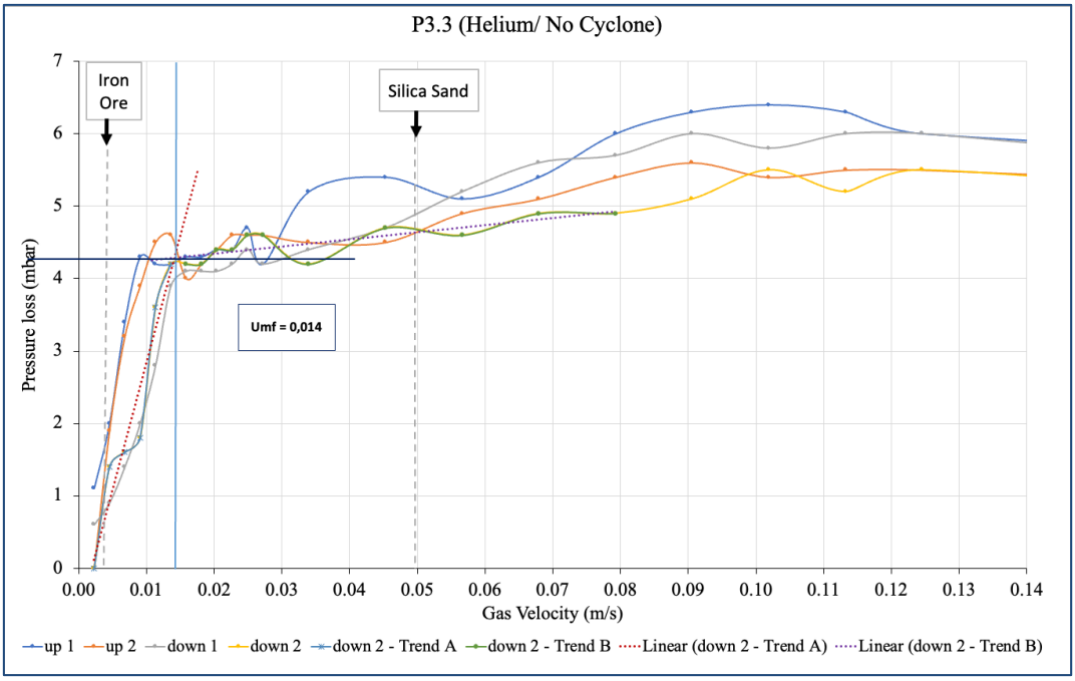

Figure 55: Pressure loss vs gas velocity of sample P3 (20 % 0.1-0.8 mm Silica Sand/ 80 % 0.063-0.125 mm Iron Ore) with helium and no cyclone

4.6.2.4 Sample P4 (80 % 0.1-0.2 mm Silica Sand/ 20 % 0.063-0.125 mm Iron Ore)

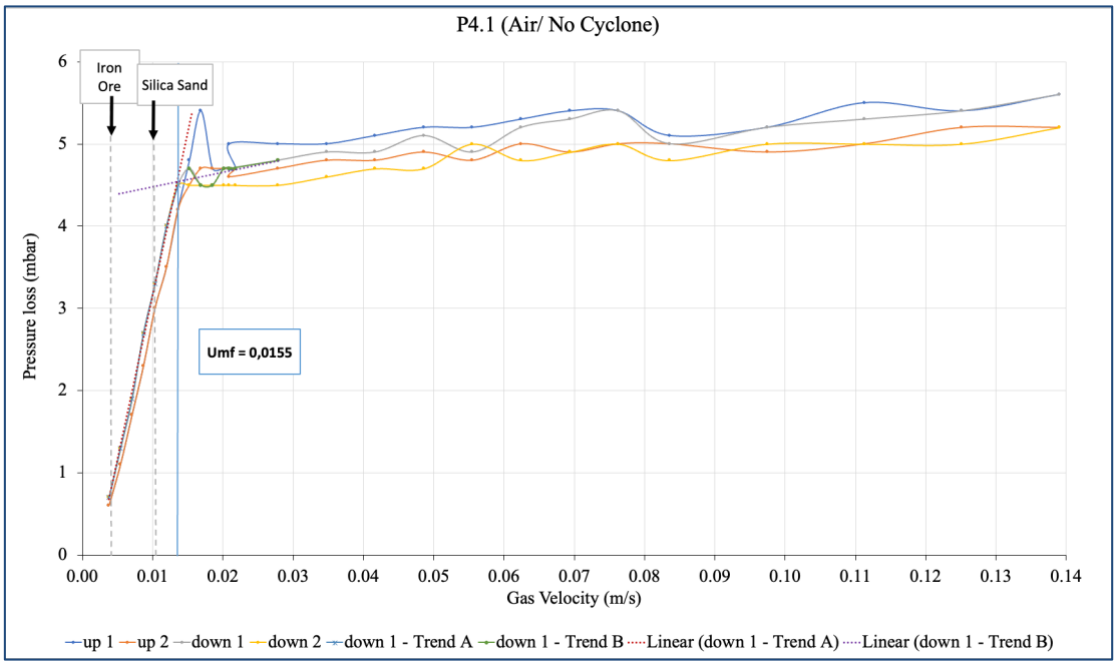

Figure 56: Pressure loss vs gas velocity of sample P4 (80 % 0.1-0.2 mm Silica Sand/ 20 % 0.063-0.125 mm Iron Ore) with air and no cyclone

This sample is chosen to represent a mixture of particles with more similar particle distributions. The overshooting phenomenon is illustrated in Figure 56. Just like for sample P3, a discharge

of particles is noticeable. A bed material loss of up to 18 % is measured. Since both components of the mixture consist of smaller particles, a shift of the pressure loss curve to higher gas velocities is not noticeable. However, the pressure loss curve illustrating the second measurement is shifted slightly lower, indicating a bed material loss after the first test run.

4.6.2.5 Sample P5 (60 % 0.1-0.2 mm Silica Sand/ 40 % 0.063-0.125 mm Iron Ore)

The pressure loss curve depicted in Figure 57 is very similar to the one for sample P4. Due to the higher mass share of iron ore in sample P5, a slight shift of the fluidization point to lower superficial velocities is noticeable. The higher share of iron ore also leads to greater discharge of particles of up to 21 %. In order to diminish these high discharge rates, sample P6 and P7 contain silica sand with higher particle diameter.

4.6.2.6 Sample P6 (80 % 0.5-0.8 mm Silica Sand/ 20 % 0.063-0.125 mm Iron Ore)

In Figure 58, the first upward measurement stands out due to its shift to lower pressure loss. Since the other measurements, as well as the ones during the test with the attached internal cyclone (Figure 59), show similar curves, the fluidization point is determined with the second downward measurement. Neither overshooting nor discharge of particles is observed during the pressure loss tests.

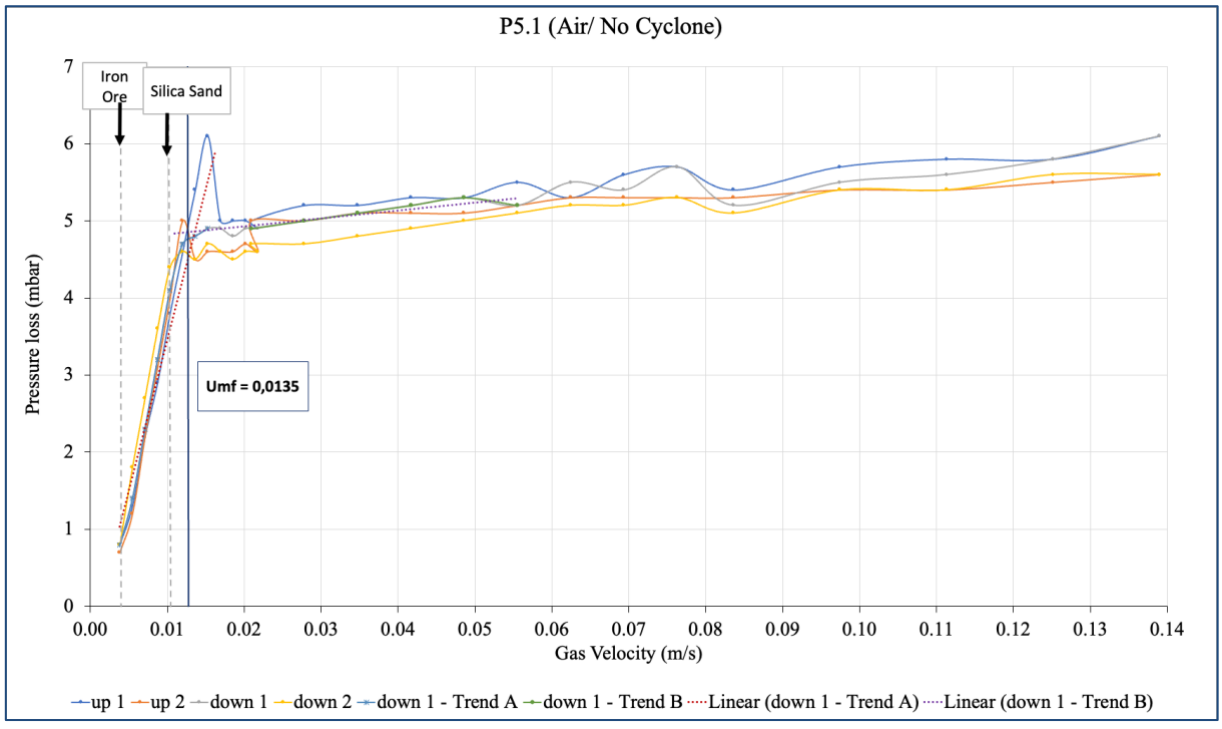

Figure 57: Pressure loss vs gas velocity of sample P5 (60 % 0.1-0.2 mm Silica Sand/ 40 % 0.063-0.125 mm Iron Ore) with air and no cyclone

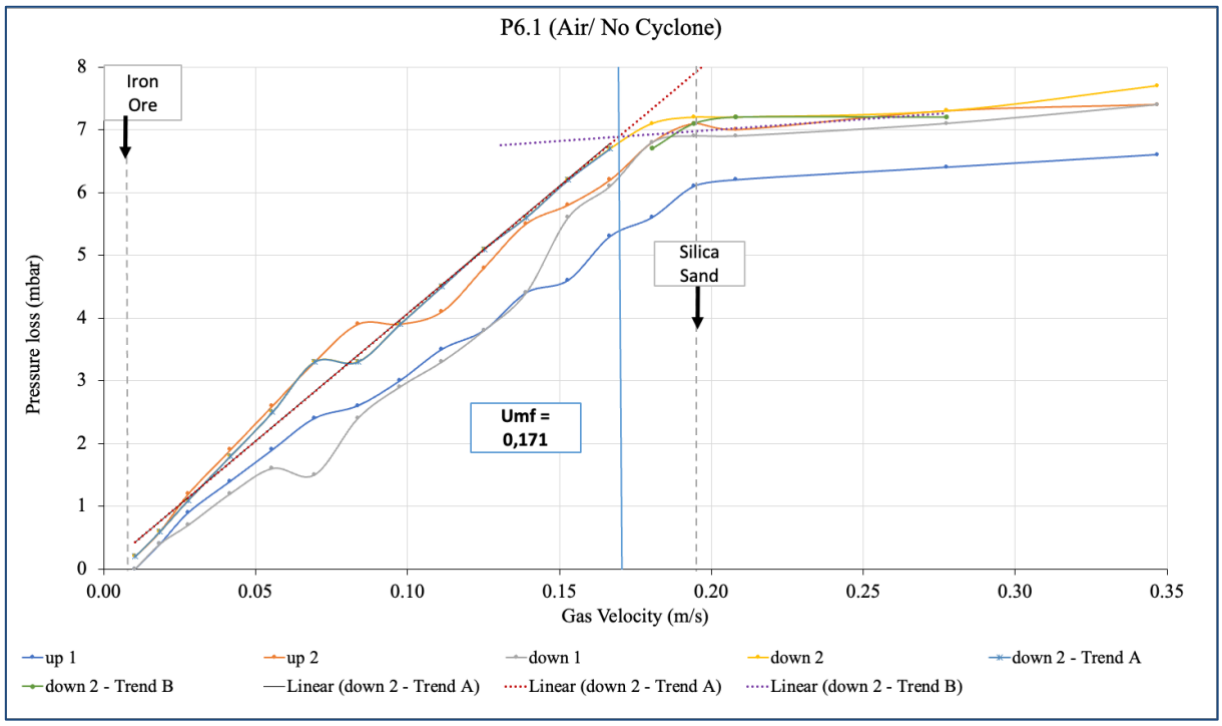

Figure 58: Pressure loss vs gas velocity of sample P6 (80 % 0.5-0.8 mm Silica Sand/ 20 % 0.063-0.125 mm Iron Ore) with air and no cyclone

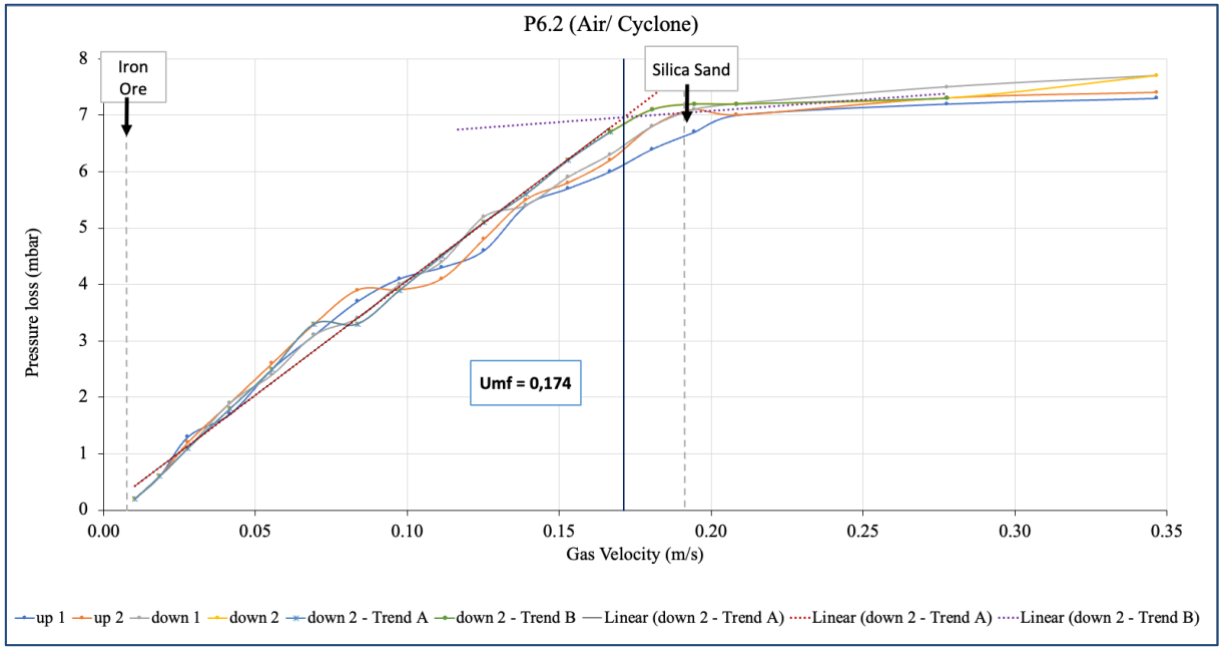

Figure 59: Pressure loss vs gas velocity of sample P6 (80 % 0.5-0.8 mm Silica Sand/ 20 % 0.063-0.125 mm Iron Ore) with air and with internal cyclone

4.6.2.7 Sample P7 (60 % 0.5-0.8 mm Silica Sand/ 40 % 0.063-0.125 mm Iron Ore)

As the superficial velocity rises, the pressure loss linearly increases without any overshooting. The fluidization point is at a lower gas velocity than for sample P6 due to the higher iron ore share in the mixture. In comparison to the location of the fluidization point for sample P6, the

minimum fluidization for sample P7 is slightly closer to the theoretical fluidization point of the iron ore in the mixture.

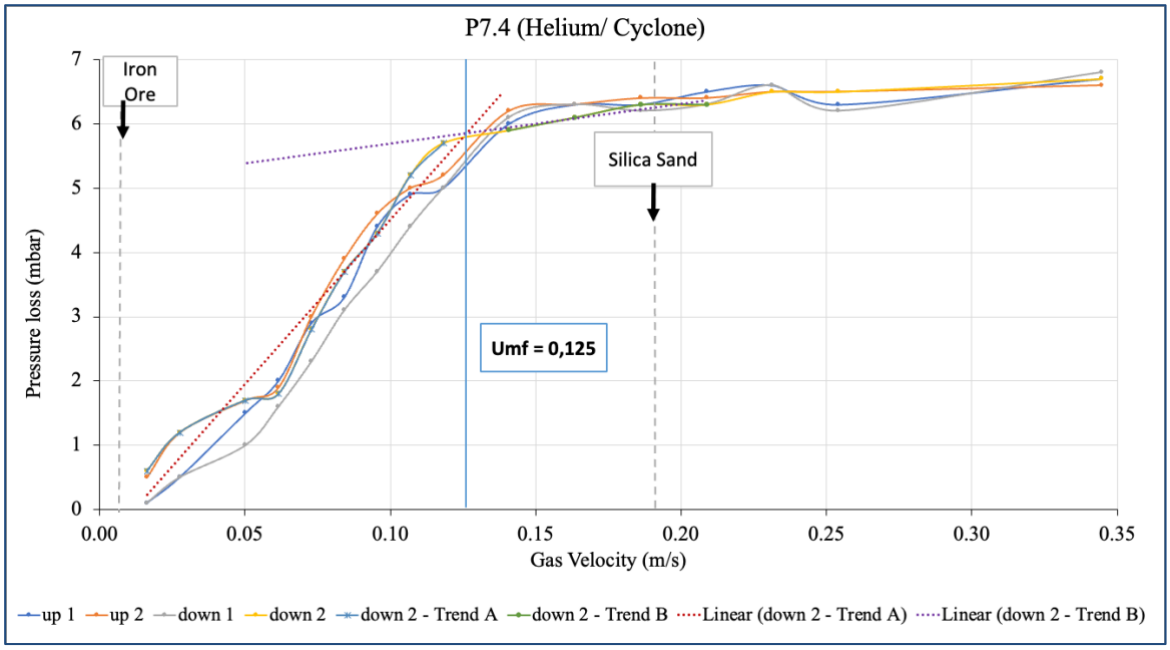

Figure 60: Pressure loss vs gas velocity of sample P7 (60 % 0.5-0.8 mm Silica Sand/ 40 % 0.063-0.125 mm Iron Ore) with helium and with internal cyclone

4.6.2.8 Sample P8 (60 % 0.8-1 mm Silica Sand/ 40 % 0.5-1 mm Iron Ore)

In order to analyze the other side of the iron ore size spectrum, mixtures with iron ore of a particle size of 0.5-1 mm were conducted.

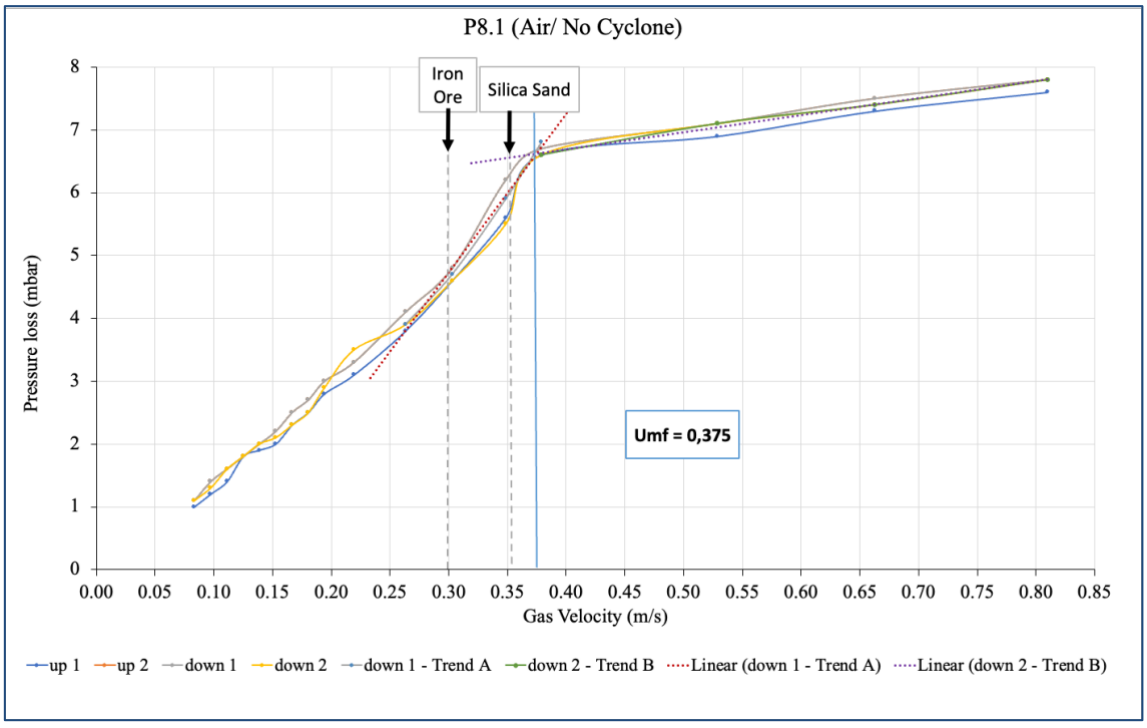

Figure 61: Pressure loss vs gas velocity of sample P8 (60 % 0.8-1 mm Silica Sand/ 40 % 0.5-1 mm Iron Ore) with air and no cyclone

As the particle size of iron ore is approximately as big as the one from sand, the mixture is not compacted by filling the reactor. Therefore, the pressure loss curve does not display any overshooting. It is evident that the minimum fluidization velocity is way higher than for mixtures P1- P7. The fluidization point does not lie within the two reference values for silica sand and iron ore. However, that could be explained by the inaccuracy of Rotameter 4, also shown in Chapter 4.2.

4.6.2.9 Sample P9 (80 % 0.5-1 mm Silica Sand/ 20 % 0.5-1 mm Iron Ore)

Figure 62 illustrates the pressure loss increase for sample P9 with the use of air and no cyclone. The first upward measurement is the only one out of the four that shows a more rapid increase in pressure loss. Due to the similarity of the other test runs, the fluidization point can be determined.

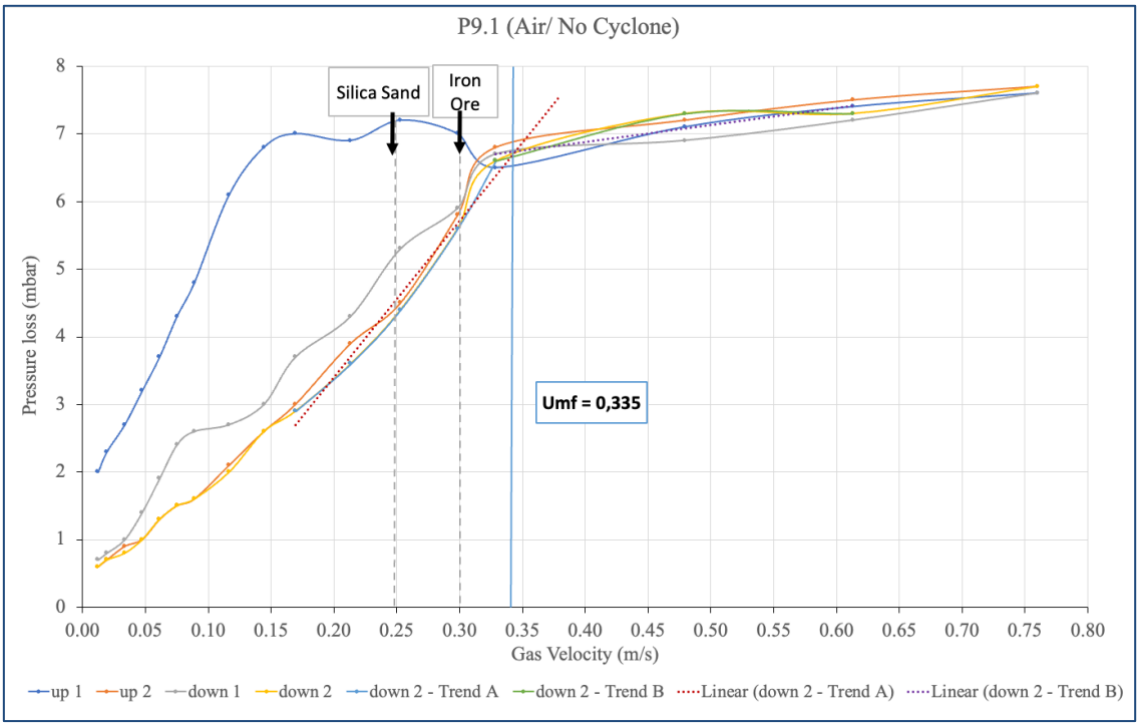

Figure 62: Pressure loss vs gas velocity of sample P9 (80 % 0.5-1 mm Silica Sand/ 20 % 0.5-1 mm Iron Ore) with air and no cyclone

Just like sample P8, the fluidization point for test run P9.1 does not lie within the two referenced values and is similar to the one obtained by sample P8. At around 0.15 m/s there is a slight increase noticeable, followed by a quick decrease. Overall, it is also evident that the shift from fixed bed to fluidized bed occurs gradually.

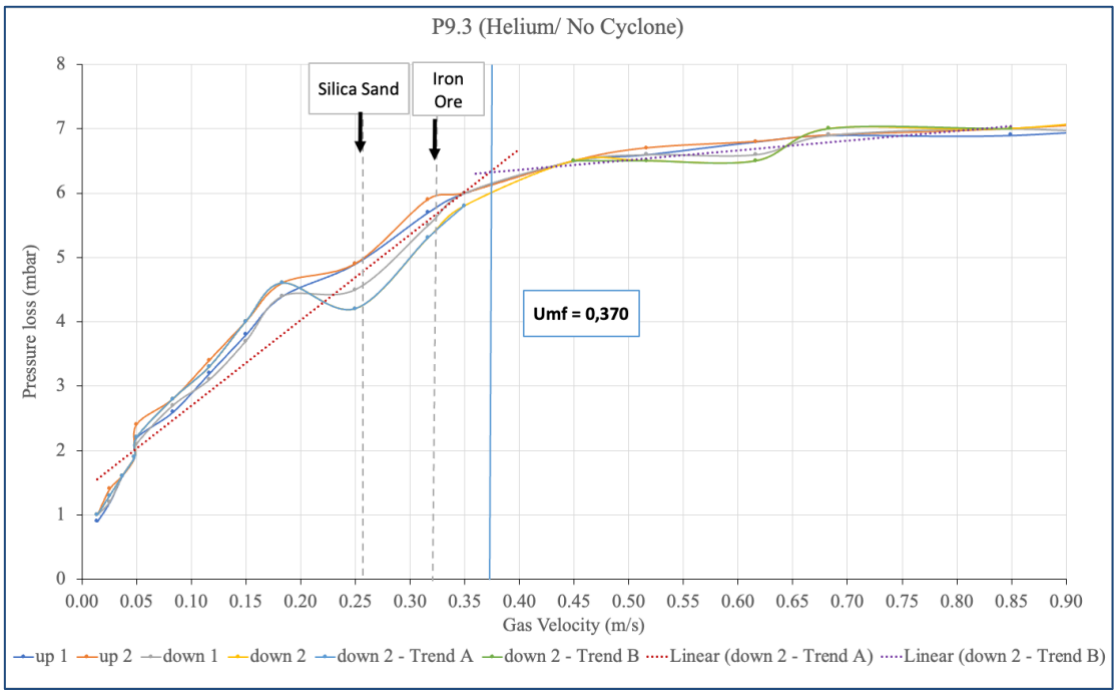

Figure 63: Pressure loss vs gas velocity of sample P9 (80 % 0.5-1 mm Silica Sand/ 20 % 0.5-1 mm Iron Ore) with helium and no cyclone

4.6.2.10 Sample P10 (60 % 0.5-1 mm Silica Sand/ 40 % 0.5-1 mm Iron Ore)

A gradual increase of the pressure loss is seen in Figure 64. During the first measurement, the pressure loss settles at a slightly smaller value than in the second test run. Again, the fluidization point does not align with the displayed fluidization points of silica sand and iron ore.

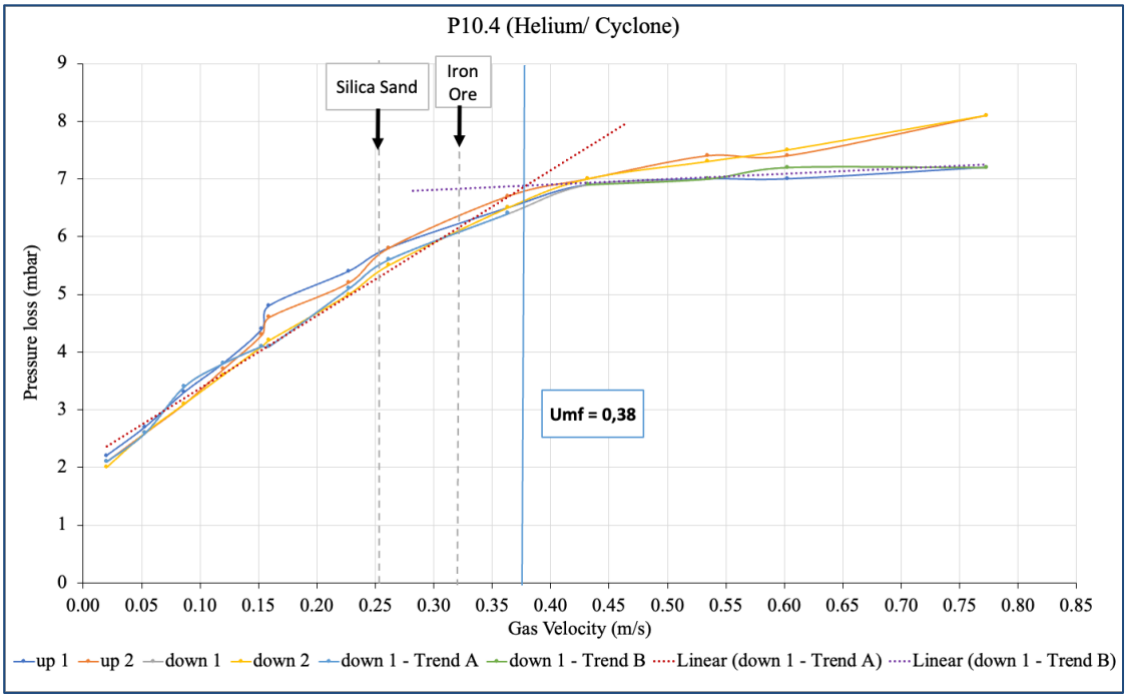

Figure 64: Pressure loss vs gas velocity of sample P10 (60 % 0.5-1 mm Silica Sand/ 40 % 0.5-1 mm Iron Ore) with air and no cyclone

4.7 Comparison of Theoretical and Experimental Results

4.7.1 Comparison of Sample Mixtures

To assess the fluidization characteristics of the sample mixtures, the experimentally determined minimum fluidization velocity is compared with the theoretically derived counterpart. The minimum fluidization velocity is computed through three distinct approaches, each based on differently assumed particle properties, with the primary distinction lying in particle density. Initially, the minimum fluidization velocity is determined using properties representative of sand particles, followed by an assumption of iron ore particle properties. Finally, the theoretical particle density for the mixture, as defined by Equation 2.7, is employed to calculate the theoretical minimum fluidization velocity. The results for these calculations for samples P1-P10 are listed in Table 22 and Table 23, alongside their relations to one another. In Table 22 and Table 23, only the experiments conducted without an internal cyclone are presented. The ratio of the theoretical minimum fluidization velocity for sand and the one for iron ore is calculated to show what mixtures display the most homogenous fluidization behaviour, meaning that all particles fluidize simultaneously, and no particles are left unfluidized. A ratio of 1 would mean that the sand particles as well as the iron ore particles fluidize at the same gas velocity, ensuring a very homogenous fluidization. Additionally, the experimentally determined minimum fluidization velocity is compared to all the theoretically obtained ones. This serves as a means to deduce the most accurate calculation method.

The relations of the minimum fluidization velocities for samples P8-P10 exhibit the lowest values, due to the similarity of particle distribution size of silica sand and iron ore. In addition, it can be said that the calculation of the theoretical minimum fluidization is the most accurate for samples with larger mean particle diameter.

On the other end of the particle distribution size spectrum, samples P4 and P5, consisting of a mixture of iron ore and silica sand with comparable mean particle diameters, show minimum fluidization velocity ratios of around 2. Even though the particles are homogenously fluidized, the large particle discharge (Chapter 4.7.3) observed during the cold model experiments shows that these mixtures are not optimal. However, an improvement of the cyclone design could minimize the discharge rate, making these samples suitable again. For samples P4 and P5, the theoretical minimum fluidization for sand closely matches the observed experimental value.

While the theoretical minimum fluidization velocity of sand is 11 times as high as the one for

iron ore for samples P1-P3, it is noticeable that the calculation approach using the iron ore properties gets increasingly more accurate with a rise in iron ore share in the mixture.

Even though the samples P6 and P7 show a value of around 45 for the ratio $U_{mf,theoret.,Sand}/U_{mf,theoret.,\ Iron\ Ore}$, the fluidization of all mixture components is visually observed in the cold model. Comparing the experimentally obtained minimum fluidization point with $U_{mf,theoret.,Sand}$ allows the assumption that the minimum fluidization point of iron ore is negligible in contrast to the one of sand, since the ratio $U_{mf,exp}/ U_{mf,theoret.,Sand}$ shows a value of around 1, while $U_{mf,exp}/ U_{mf,theoret.,Iron\ Ore}$ is equal to approximately 40. This assumption matches closely with the ratio $U_{mf,exp}/ U_{mf,theoret.,Sand}$ obtained for all mixtures with up to 60 % silica sand.

It can be said that the calculation approach using the properties of silica sand is generally the most accurate one for mixtures consisting of up to 60 % of silica sand, which is why in the following two chapters this calculation method is applied for the determination of the theoretical minimum fluidization velocity.

Table 21: Legend for Table 22 and Table 23 – ratio of minimum fluidization velocities

$0.7 < U_{mf,i}/ U_{mf,j} < 2.5$	$0.5 < U_{mf,i}/ U_{mf,j} < 0.7$ $2.5 < U_{mf,i}/ U_{mf,j} < 10$	$0.3 < U_{mf,i}/ U_{mf,j} < 0.5$ $10 < U_{mf,i}/ U_{mf,j} < 15$	$0 < U_{mf,i}/ U_{mf,j} < 0.3$ $U_{mf,i}/ U_{mf,j} > 15$

4.7.2 Comparison of Cold Model Experiments with Air vs Helium

This chapter focuses on the comparison of the two fluidizations gases utilized in the cold model experiments. For this purpose, samples P2 and P8 are chosen for demonstration, in order to display both sides of the iron ore particle distribution spectrum. The characteristics of the samples are detailed in Table 24, along with the outcomes of theoretical calculations for the theoretical minimal fluidization velocity and pressure loss. Similar to the previous chapter, all test runs presented in Table 24 were conducted without utilizing an internal cyclone.

Analysis of the results reveals the following trends: In the case of sample P2, which is characterized by a smaller mean particle diameter, the minimum fluidization velocity is lower in test runs with helium compared to those with air (as seen in Figure 65) , while for sample P8, which is a representative for samples with a higher mean particle diameter, the opposite holds true. This trend is consistent in the experimental values as well. For both samples, the test run with helium exhibits a slightly higher deviation than the one with air.

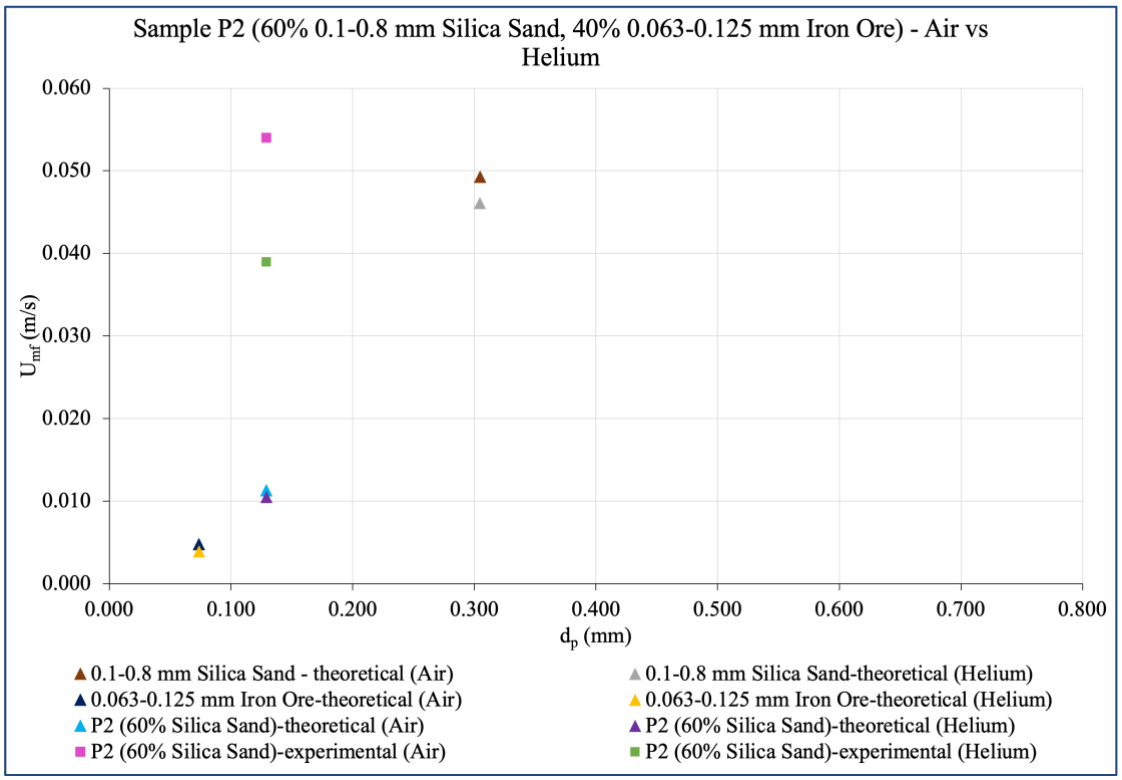

Figure 65: Dependence of minimum fluidization velocity on fluidization gas and particle diameter of mixture components

Figure 65 shows the experimental values of U_{mf} in contrast to the theoretically obtained ones of sample P2, which were calculated in three different ways, assuming particle properties of only iron ore or sand and calculating using a theoretical particle density of the mixture. The calculation for an assumed mixture does not correspond well with the experimental values, its value is about one fifth of the experimental one. The experimental results match best with the theoretical minimum fluidization velocity determined with the particle properties of sand, which is also the main component of mixture P2.

In order to explain the aforementioned trend, Equation 2.13 is analyzed and the dependence of the minimum fluidization velocity on the particle diameter is assessed in Figure 66. Particle diameters ranging from 0.063 mm to 1 mm are assumed for the analysis. Until an iron ore particle diameter of about 0.45 mm, the theoretical minimum fluidization velocity for air is slightly higher than the one calculated for helium. However, once a certain iron ore particle diameter, which is approximately 0.45 mm, is reached, the minimum fluidization velocity obtained when using helium as fluidization gas rapidly increases in comparison to the one determined for air. Even though the same is observed for silica sand, the particle diameter, at which the minimum fluidization velocity determined when using helium overtakes the one calculated with air, is shifted to higher particle diameters and is around 0.50 mm. When

analyzing the first term of Equation 2.13, the following deduction can be made: A small diameter means that the density does not factor into the minimum fluidization calculation as much as the dynamic viscosity does, since the denominator will be a small value, independent from the density value. Due to the similar dynamic viscosities of helium and air, the theoretical minimum fluidization velocity obtained for helium and air is comparable. In contrast, a higher particle diameter corresponds with an increased effect of the density on the minimum fluidization velocity compared to the dynamic viscosity. As the density of helium is much smaller than the one of air, the minimum fluidization velocity calculated for helium is higher than the one for air. This results from the indirect proportionality of density and minimum fluidization velocity. The second term in Equation 2.13 that includes the Archimedes number only amplifies the dependence of the minimum fluidization velocity on the particle diameter, as a result of the direct proportionality of particle diameter and Archimedes number. These deductions are visualized in Figure 67 and Figure 68, where the dependence of the fluid density and viscosity on the minimum fluidization velocity is illustrated, while assuming particle properties of sand.

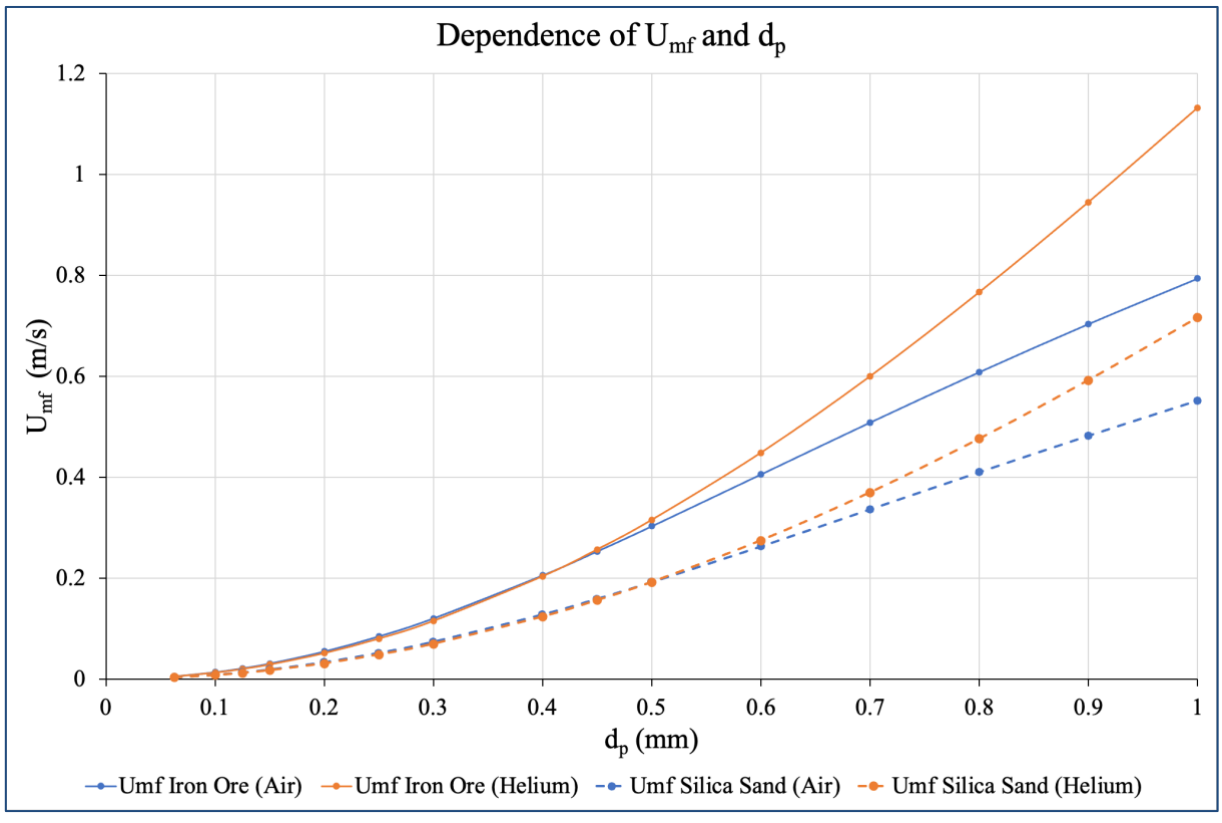

Figure 66: Dependence of the iron ore and silica sand particle diameter on the minimum fluidization velocity

As can be seen in Figure 67, the density does not seem to have a significant influence on U_{mf} at lower particle diameters such as 0.3 mm, since the function seems almost constant. A slight reduction of minimum fluidization velocity is observed with increasing fluid density at a

particle diameter of 0.5 mm. This decrease is amplified at a higher particle diameter of 0.7 mm. In contrast to the density´s effect, higher dynamic viscosities lead to lower minimum fluidization velocities, as depicted in Figure 68.

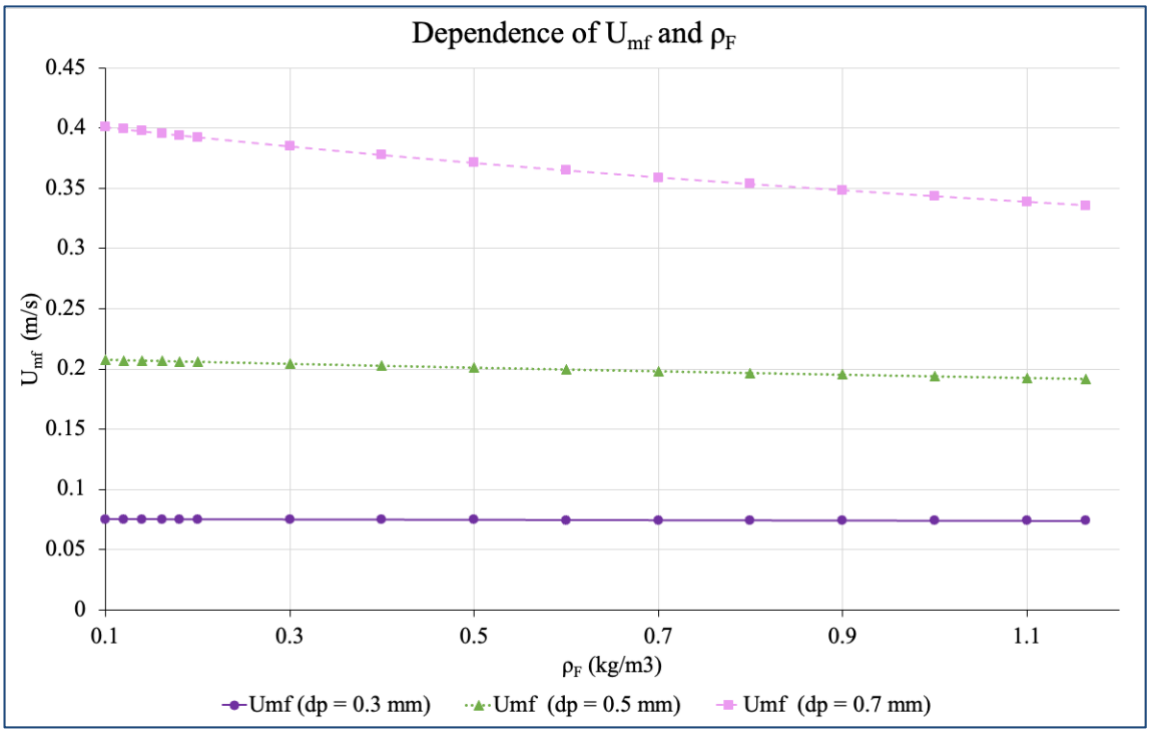

Figure 67: Dependence of the minimum fluidization velocity and the fluid density (assuming particle density of silica sand of 2600 kg/m^3)

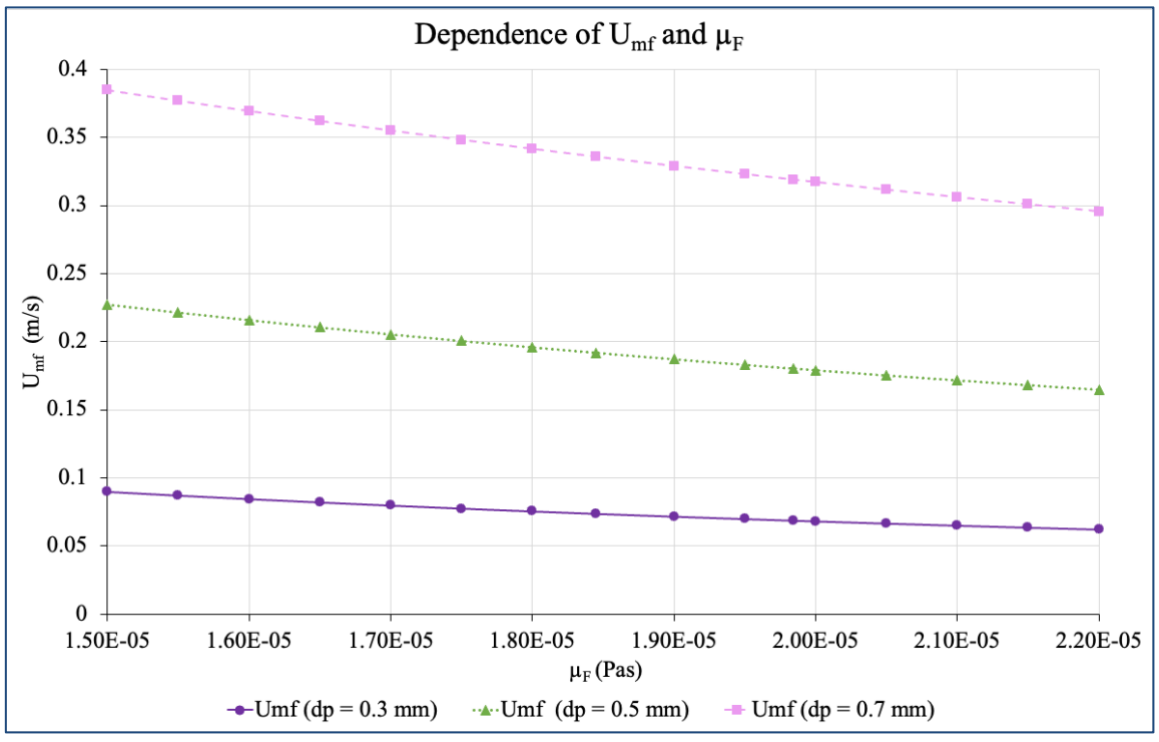

Figure 68: Dependence of the minimum fluidization velocity and the fluid viscosity (assuming particle density of silica sand)

Since pressure loss is predominantly influenced by particle density and just particle properties in general rather than fluid properties, the choice of fluidization gas has practically no impact on pressure loss, as can be seen in in Table 24.

Table 22: Comparison of Theoretical and Experimental Data - Comparison of Sample Mixtures P1-P5

Experiment Nr.	Sample and Test Definition						Comparison U_{mf}							
	Particle Distribution Size		Mass Share		Fluidization Gas	Particle Diameter d_p	Theoretical Min. Fluid. Velocity for Sand $U_{mf,theoret.,Sand}$	Theoretical Min. Fluid. Velocity for Iron Ore $U_{mf,theoret.,Iron\ Ore}$	Theoretical Min. Fluid. Velocity for Mixture $U_{mf,theoret.,Mixture}$	Experimental Min. Fluid. Velocity $U_{mf,exp.}$	$U_{mf,theoret.,Sand}$ / $U_{mf,theoret.,Iron\ Ore}$	$U_{mf,exp}$ / $U_{mf,theoret.,lSand}$	$U_{mf,exp}$ / $U_{mf,theoret.,Iron\ Ore}$	$U_{mf,exp}$ / $U_{mf,theoret.,Mixture}$
	mm		%		-	mm	m/s	m/s	m/s	m/s	-	-	-	-
	Iron Ore	Sand	Iron Ore	Sand										
P1.1	0.063-0.125	0.1-0.8	20	80	Air	0.155	0.049	0.004	0.015	0.085	11.64	1.72	20.07	5.86
P1.3					Helium		0.046	0.004	0.014	0.079	11.76	1.71	20.14	5.87
P2.1	0.063-0.125	0.1-0.8	40	60	Air	0.129	0.049	0.004	0.011	0.054	11.64	1.10	12.77	4.78
P2.3					Helium		0.046	0.004	0.011	0.039	11.76	0.84	9.93	3.71
P3.1	0.063-0.125	0.1-0.8	80	20	Air	0.085	0.049	0.004	0.006	0.012	11.64	0.24	2.85	2.02
P3.3					Helium		0.046	0.004	0.006	0.014	11.76	0.30	3.57	2.53
P4.1	0.063-0.125	0.1-0.2	20	80	Air	0.113	0.010	0.004	0.008	0.016	2.40	1.53	3.67	2.01
P4.3					Helium		0.009	0.004	0.007	0.015	2.40	1.59	3.82	2.09
P5.1	0.063-0.125	0.1-0.2	40	60	Air	0.100	0.010	0.004	0.007	0.014	2.40	1.33	3.18	1.99
P5.3					Helium		0.009	0.004	0.006	0.011	2.40	1.15	2.76	1.73

Table 23: Comparison of Theoretical and Experimental Data - Comparison of Sample Mixtures P5-P10

Experiment Nr.	Sample and Test Definition						Comparison U_{mf}							
	Particle Distribution Size		Mass Share		Fluidization Gas	Particle Diameter d_p	Theoretical Min. Fluid. Velocity for Sand $U_{mf,theoret.,Sand}$	Theoretical Min. Fluid. Velocity for Iron Ore $U_{mf,theoret.,Iron\ Ore}$	Theoretical Min. Fluid. Velocity for Mixture $U_{mf,theoret.,Mixture}$	Experimental Min. Fluid. Velocity $U_{mf,exp.}$	$U_{mf,theoret.,Sand}$ / $U_{mf,theoret.,Iron\ Ore}$	$U_{mf,exp}$ / $U_{mf,theoret.,ISand}$	$U_{mf,exp}$ / $U_{mf,theoret.,Iron\ Ore}$	$U_{mf,exp}$ / $U_{mf,theoret.,Mixture}$
	mm		%		-	mm	m/s	m/s	m/s	m/s	-	-	-	-
	Iron Ore	Sand	Iron Ore	Sand										
P6.1	0.063-0.125	0.5-0.8	20	80	Air	0.229	0.188	0.004	0.032	0.171	44.35	0.91	40.51	5.41
P6.3					Helium		0.189	0.004	0.030	0.129	48.14	0.68	32.93	4.33
P7.1	0.063-0.125	0.5-0.8	40	60	Air	0.158	0.188	0.004	0.017	0.165	44.35	0.88	38.97	9.77
P7.3					Helium		0.189	0.004	0.016	0.130	48.14	0.69	33.20	8.31
P8.1	0.5-1	0.8-1	40	60	Air	0.767	0.352	0.328	0.335	0.375	1.07	1.07	1.15	1.12
P8.3					Helium		0.390	0.345	0.360	0.415	1.13	1.06	1.20	1.15
P9.1	0.5-1	0.5-1	20	80	Air	0.717	0.246	0.328	0.300	0.335	0.75	1.37	1.02	1.12
P9.3					Helium		0.253	0.345	0.316	0.370	0.73	1.46	1.07	1.17
P10.1	0.5-1	0.5-1	40	60	Air	0.695	0.246	0.328	0.285	0.365	0.75	1.48	1.11	1.28
P10.3					Helium		0.253	0.345	0.297	0.348	0.73	1.37	1.01	1.17

Table 24: Comparison of Theoretical and Experimental Data - Comparison of Air vs Helium

Experiment Nr.	Sample and Test Definition						Comparison of Theoretical and Experimental Data						
	Particle Distribution Size		Mass Share		Fluidization Gas	Particle Diameter d_p	Theoretical Min. Fluid. Velocity for Sand $U_{mf,theoret.,Sand}$	Experimental Min. Fluid. Velocity $U_{mf,exp.}$	Deviation $U_{mf,exp} - U_{mf,theoret.}$	Bed Material Mass m,Sand	Experimental Pressure Loss Δp_{exp}	Theoretical Pressure Loss $\Delta p_{theoret.}$	Deviation $\Delta p_{exp} - \Delta p_{theoret.}$
	mm		%		-	mm	m/s	m/s	%	g	Pa	Pa	%
	Iron Ore	Sand	Iron Ore	Sand									
P2.1	0.063-0.125	0.1-0.8	40	60	Air	0.129	0.049	0.054	8.80%	90	660	691.92	4.61%
P2.3					Helium		0.046	0.039	16.56%		635	692.13	8.25%
P8.1	0.5-1	0.8-1	40	60	Air	0.767	0.352	0.375	6.35%	85	660	653.48	0.99%
P8.3					Helium		0.390	0.415	6.08%		650	653.68	0.56%

4.7.3 Influence of the Presence of a Cyclone on the Cold Model Experiments

Since the cyclone´s main task is to diminish the percentage of discharged particles, the pressure loss diagrams for sample P5, which consists of 60 % 0.1-0.2 mm silica sand and 40 % 0.063-0.125 mm iron ore, is chosen. While Figure 57 shows the test run without a cyclone, Figure 69 illustrates the pressure loss for an experiment with the attached internal cyclone.

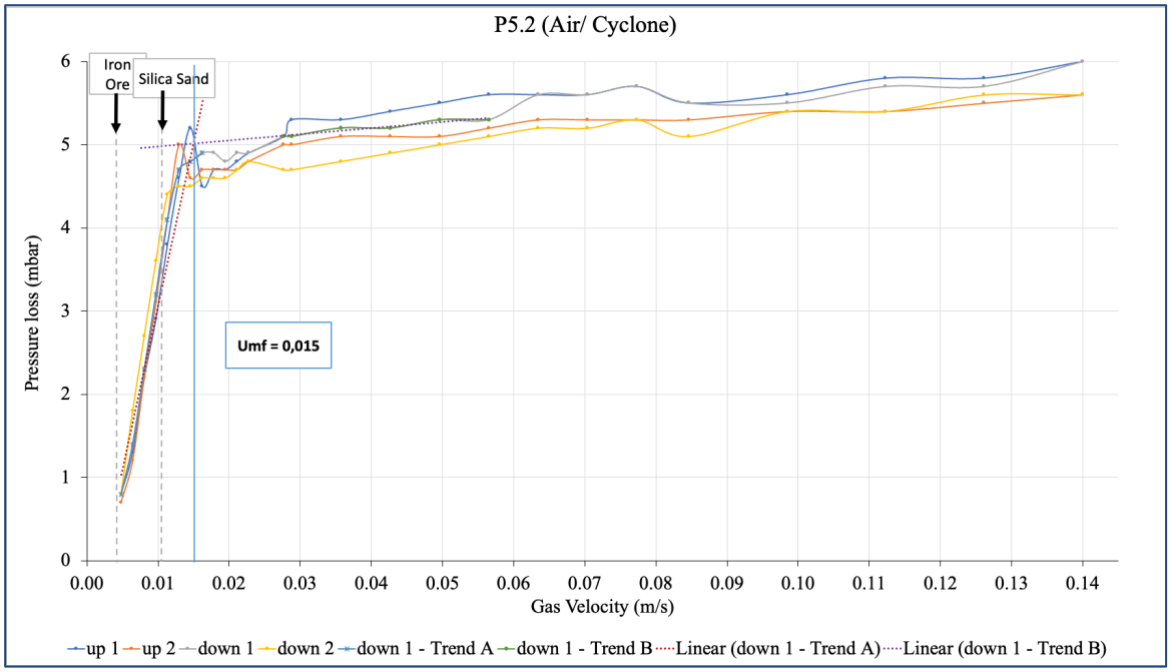

Figure 69: Pressure loss vs gas velocity of sample P5 (60 % 0.1-0.2 mm Silica Sand/ 40 % 0.063-0.125 mm Iron Ore) with air and with internal cyclone

Besides the non – existing overshooting, the pressure loss curves in both diagrams look almost identical.

The bed material loss documented for the test run with the cyclone is about 20 %, which means that the cyclone does not drastically improve the discharge rate.

In order to demonstrate the effectiveness of the internal cyclone for the smaller particle sizes, the discharge was measured for samples P3-P5. As can be deducted from Table 25 the bed material loss increases with higher iron ore fines share, when comparing the results for sample P4 and P5. The higher particle size of silica sand in sample P3 seems to have a substantial influence in decreasing the discharge.

Table 25: Bed Material Losses for samples P3-P5

Experiment Nr.	Sample and Test Definition							Bed Material Loss
	Particle Distribution Size		Mass Share		Fluidization Gas	Cyclone	Particle Diameter d_p	
	mm		%		-	-	mm	%
	Iron Ore	Sand	Iron Ore	Sand				
P3.1	**0.063-0.125**	**0.1-0.8**	**80**	**20**	Air	no	0.085	13
P3.2						yes		11
P3.3					Helium	no		14
P3.4						yes		13
P4.1	**0.063-0.125**	**0.1-0.2**	**20**	**80**	Air	no	0.113	18
P4.2						yes		18
P4.3					Helium	no		19
P4.4						yes		17
P5.1	**0.063-0.125**	**0.1-0.2**	**40**	**60**	Air	no	0.100	21
P5.2						yes		20
P5.3					Helium	no		20
P5.4						yes		19

In order to show the similarities of the test runs with and without an internal cyclone, the results for sample P4 and P8 are chosen and listed in Table 26.

The minimum fluidization velocity barely changes with the use of an internal cyclone, corresponding with the bed material losses shown in Table 25. It can be deduced that the collection of the fine particles and their reintroduction into the system is not executed by the cyclone. A possible explanation could be that the gas flowing through the bed of particles enters the pipe of the cyclone, pushing back the collected particles and possibly even pressing bed particles up the pipe.

Table 26: Comparison of Theoretical and Experimental Data – Influence of the Presence of a Cyclone on the Cold Model Experiments

Experiment Nr.	Sample and Test Definition						Comparison of Theoretical and Experimental Data						
	Particle Distribution Size		Mass Share		Fluidization Gas	Cyclone	Particle Diameter d_p	Theoretical Min. Fluid. Velocity for Sand $U_{mf,theoret.,Sand}$	Experimental Min. Fluid. Velocity $U_{mf,exp.}$	Deviation $U_{mf,exp} - U_{mf,theoret.}$	Bed Material Mass m	Experimental Pressure Loss Δp_{exp}	Theoretical Pressure Loss $\Delta p_{theoret.}$	Deviation $\Delta p_{exp} - \Delta p_{theoret.}$
	mm		%		-	-	mm	m/s	m/s	%	g	Pa	Pa	%
	Iron Ore	Sand	Iron Ore	Sand										
P4.1	0.063-0.125	0.1-0.2	20	80	Air	no	0.113	0.0101	0.016	34.66%	75	447	545.83	18.11%
P4.2						yes			0.016	36.43%		495		9.31%
P4.3					Helium	no		0.0095	0.015	36.42%		475	542.73	12.48%
P4.4						yes			0.015	34.52%		430		20.77%
P8.1	0.5-1	0.8-1	40	60	Air	no	0.767	0.352	0.375	6.35%	85	660	653.48	0.99%
P8.2						yes			0.385	8.72%		650		0.53%
P8.3					Helium	no		0.390	0.415	6.08%		650	653.68	0.56%
P8.4						yes			0.410	4.89%		580		11.27%

5 Conclusion

The focus of this thesis is set on the cold modelling of a fluidized bed with helium as fluidization gas, simulating the fluidization behaviour of mixtures of silica sand and iron ore during the reduction of fine iron ores with hydrogen in a pressurized and hot reactor. In addition, the influence of a cyclone on the fluidization behaviour and especially on the discharge of finer particles is investigated.

The use of helium as fluidization gas was argued by applying Glicksman ´s similarity rules from the cold model to the hot pressurized reactor. While the reactor geometry as well as the Froude number in cold and hot reactor are identical, the ratio of particle density and fluid density is only comparable and not identical. The density of helium in cold model conditions (25°C, 1.013 bar) at 0.16 kg/m^3 [50] is twice as high as the one of hydrogen in cold model conditions with 0.08 kg/m^3 [50]. Furthermore, the density of helium in cold model conditions is 1.3 times higher than the one of hydrogen in hot reactor conditions (700°C, 5 bar) with 0.12 kg/m^3 [50]. However, in contrast to air in cold model conditions (25°C, 1.013 bar), which is characterized by a density of 1.17 kg/m^3 [50] that is 14 times higher than the one for hydrogen in cold model conditions, helium is a more suitable fluidization gas for the simulation of hydrogen in the hot reactor. The Reynolds number obtained with helium as fluidization gas is in the same order of magnitude as the one calculated for hydrogen, while the one for air is up to ten times larger, as seen in Table 10 and Table 11. Even though two of the four Glicksman criteria are not completely met, helium is a very comparable gas to hydrogen.

Designing a cold model enabled the conduction of experiments with mixtures of iron ore and silica sand due to their utilization in the pressurized vessel to optimize the fluidization characteristics. The required rotameters as well as the piping essential to transfer the fluidization gases from their source to the cold model were dimensioned to fit the necessary air and helium flow. The pressure measurement was facilitated by incorporating a SPS system into the cold model.

When comparing the theoretical minimum fluidization velocities of iron ore and silica sand for the ten sample mixtures, one can say that similar particle distribution sizes of both mixture components lead to similar theoretical minimum fluidization points, despite their different densities, meaning that all particles fluidize almost simultaneously. This can be observed for coarser as well as for finer samples, as seen in Table 22 and Table 23. Furthermore, the test

results validate the accuracy of the U_{mf} calculation approach using silica sand particle properties, particularly for samples containing up to 60 % silica sand. Even though samples with very dissimilar particle distributions sizes and a large ratio $U_{mf,theoret.,Sand}/U_{mf,theoret.,\ Iron\ Ore}$ of up to 45 do not seem like ideal samples for fluidization, as seen in Table 23, it was observed that the particles are evenly distributed throughout the fluidized bed during the cold model experiments.

Samples with a smaller mean particle diameter (Table 24) subjected to helium as fluidization gas fluidize at lower velocities than when fluidized by air. However, the opposite is observed for samples with a larger mean particle diameter. These trends can be observed for theoretical, as well as experimental values. The dependency of the minimum fluidization velocity on the particle diameter, depicted in Figure 66, shows that at an iron ore particle diameter of about 0.45 mm, the minimum fluidization velocity for helium is higher than for air, while the same happens for silica sand at a particle diameter of 0.50 mm. The fluid density shows a stronger impact in the equation for the minimum fluidization velocity at larger particle diameters (as depicted in Figure 67), while the dynamic viscosity is the main contributor to the trend seen for smaller particle diameters (as seen in Figure 68). As the density of helium is much lower than the one of air, the minimum fluidization velocity rises once the particle diameter surpasses the observed 0.45 mm for iron ore or 0.50 mm for silica sand, as illustrated in Figure 66.

Even with the use of an internal cyclone during the cold model experiments conducted with the finer samples, a distinct discharge of particles was observed. This discharge proves the low efficiency of the internal cyclone. As seen in Table 25, the loss of bed material increases with a higher iron ore share. The highest material loss that was documented is for a sample consisting of a fine iron ore fraction as well as a fine silica sand fraction, with up to 21 % discharge. A larger particle size of silica sand in the mixture appears to significantly contribute to the reduction of discharge. Even though the fine samples with similar particle distributions sizes seem ideal in terms of fluidization due to the similarity of U_{mf} of both mixture components, the discharge of particles indicates that these samples may not be fitting. Nevertheless, by refining the cyclone design, it may be possible to restore the suitability of these samples.

Outlook

As the experimental setup was originally designed to mix two gases, the next step would be to determine a mixture of helium and possibly air or nitrogen to simulate the gas mixture

properties in the hot reactor, since not pure hydrogen is used as a reduction gas. Another critical step would be the improvement of the cyclone design, especially since an updated cold model is under construction.

6 Bibliography

[1] International Energy Agency, Emissions Measurement and Data Collection for a Net Zero Steel Industry, Paris, 2023, URL: https://www.iea.org/reports/emissions-measurement-and-data-collection-for-a-net-zero-steel-industry/executive-summary (last visited on 12.01.2024)

[2] Erneuerbare Energie Österreich, Grüner Stahl, 2022, URL: https://www.erneuerbare-energie.at/energiefakten/2022/9/11/gruener-stahl#:~:text=In%5C%20Europa%5C%20hat%5C%20die%5C%20Stahlindustrie,3%5C%25%5C%20zu%5C%20den%5C%20Treibhausgasemissionen%5C%20bei. (last visited on 12.01.2024)

[3] J. Kim et al., "Decarbonizing the iron and steel industry: A systematic review of sociotechnical systems, technological innovations, and policy options," Energy Res Soc Sci, vol. 89, p. 102565, 2022, doi: https://doi.org/10.1016/j.erss.2022.102565.

[4] V. Vogl, M. Åhman, and L. J. Nilsson, "Assessment of hydrogen direct reduction for fossil-free steelmaking," J Clean Prod, vol. 203, pp. 736–745, 2018, doi: https://doi.org/10.1016/j.jclepro.2018.08.279.

[5] Joint Research Centre, EU climate targets: how to decarbonise the steel industry, 2022, URL: https://joint-research-centre.ec.europa.eu/jrc-news-and-updates/eu-climate-targets-how-decarbonise-steel-industry-2022-06-15_en (last visited on 12.01.2024)

[6] D. Kunii and O. Levenspiel, Fluidization engineering, 2. ed. in Butterworth-Heinemann series in chemical engineering. Boston [u.a.]: Butterworth-Heinemann, 1991.

[7] J. R. Grace, X. Bi, and N. Ellis, "Essentials of fluidization technology," Essentials of Fluidization Technology, pp. 1–604, Jan. 2020, doi: 10.1002/9783527699483.

[8] D. Geldart, "Types of gas fluidization," Powder Technol, vol. 7, no. 5, pp. 285–292, May 1973, doi: 10.1016/0032-5910(73)80037-3.

[9] J. Drake, "Hydrodynamic Characterization of 3D Fluidized Beds Using Noninvasive Techniques," Jan. 2011.

[10] H. Hofbauer, "Wirbelschichttechnik-Grundlagen", Institut für Verfahrenstechnik, Umwelttechnik und technische Biowissenschaften, TU Wien, 2019.

[11] VDI Heat Atlas. Berlin, Heidelberg: Springer Berlin Heidelberg, 2010. doi: 10.1007/978-3-540-77877-6.

[12] C. Y. Wen and Y. H. Yu, "A generalized method for predicting the minimum fluidization velocity," AIChE Journal, vol. 12, no. 3, pp. 610–612, May 1966, doi: 10.1002/AIC.690120343.

[13] A. Anantharaman, R. A. Cocco, and J. W. Chew, "Evaluation of correlations for minimum fluidization velocity (Umf) in gas-solid fluidization," Powder Technol, vol. 323, pp. 454–485, Jan. 2018, doi: 10.1016/J.POWTEC.2017.10.016.

[14] P. Bourgeois and P. Grenier, "The ratio of terminal velocity to minimum fluidising velocity for spherical particles," Can J Chem Eng, vol. 46, no. 5, pp. 325–328, Oct. 1968, doi: 10.1002/CJCE.5450460508.

[15] R. P. Vaid and P. Sen Gupta, "Minimum fluidization velocities in beds of mixed solids," Can J Chem Eng, vol. 56, no. 3, pp. 292–296, Jun. 1978, doi: 10.1002/CJCE.5450560304.

[16] A. K. Biń, "Prediction of the minimum fluidization velocity," Powder Technol, vol. 81, no. 2, pp. 197–199, Nov. 1994, doi: 10.1016/0032-5910(94)02868-0.

[17] J. Baeyens and D. Geldart, "Predictive calculations of flow parameters in gas fluidised beds and fluidisation behaviour of various powders," In Proc. Conf. La Fluidisation et ses Applications, pp. 263–273, 1973.

[18] Yang, W.-C., "Handbook of Fluidization and Fluid-Particle Systems," CRC Press, Mar. 2003, doi: 10.1201/9780203912744.

[19] G. Yates, Paola Lettieri, "Fluidized-Bed Reactors: Processes and Operating Conditions", Springer International Publishing, 2016, doi: https://doi.org/10.1007/978-3-319-39593-7.

[20] T. Battle, U. Srivastava, J. Kopfle, R. Hunter, and J. Mcclelland, "The Direct Reduction of Iron," no. 2, 2014, doi: 10.1016/B978-0-08-096988-6.00016-X.

[21] L. von Bogdandy and H.-J. Engell, The Reduction of Iron Ores. Springer Berlin Heidelberg, 1971. doi: 10.1007/978-3-662-10400-2.

[22] D. Spreitzer and J. Schenk, "Reduction of Iron Oxides with Hydrogen—A Review," Steel Res Int, vol. 90, no. 10, Oct. 2019, doi: 10.1002/SRIN.201900108.

[23] Franz. Oeters, Metallurgie der Stahlherstellung, Verlag Stahleisen, 1989.

[24] Bernd Weiss, "Kinetics of iron ore fines reduction under fluidized bed conditions at elevated pressures", Ph.D. Thesis, Institut für Verfahrenstechnik, Umwelttechnik und technische Biowissenschaften, TU Wien, 2008.

[25] L. V. Bogdandy, H. P. Schulz, I. N. Stranski, and B. Würzner, "Über den Reduktionsmechanismus von Eisenoxyden," Berichte der Bunsengesellschaft für physikalische Chemie, vol. 67, no. 9–10, pp. 958–964, Nov. 1963, doi: 10.1002/BBPC.19630670918.

[26] C. Y. Wen, "Noncatalytic heterogeneous solid-fluid reaction models," Ind Eng Chem, vol. 60, no. 9, pp. 34–54, Sep. 1968, doi: 10.1021/IE50705A007.

[27] J. Sturn, B. Weiss, F. Winter, and J. Schenk, "Limiting steps in multistage iron ore fines reduction with H2-rich gases in fluidized beds at elevated pressures," Proceedings of 9th Int.Conf.on Circulating Fluidized Bed Technology, p. 6, 2008.

[28] "World Steel in Figures 2023 - worldsteel.org." URL: https://worldsteel.org/steel-topics/statistics/world-steel-in-figures-2023/#crude-steel-production-by-process-2022 (last visited on 02.09.2024)

[29] R. Remus, S. Roudier, and L. et al. Delgado Sancho, "Best Available Techniques (BAT) Reference Document for Iron and Steel Production.", Report, Joint Research Centre, European Comission, 2013, doi:10.2791/97469.

[30] M. Degner and Stahlinstitut VDEh, "Steel manual", Verlag Stahleisen, 2008.

[31] R. S. Treptow and L. Jean, "The iron blast furnace: A study in chemical thermodynamics," J Chem Educ, vol. 75, no. 1, pp. 43–47, 1998, doi: 10.1021/ED075P43.

[32] P. Cavaliere, "Smelting Reduction: Most Efficient Technologies for Greenhouse Emissions Abatement," Clean Ironmaking and Steelmaking Processes, pp. 377–417, 2019, doi: 10.1007/978-3-030-21209-4_7.

[33] J. L. Schenk, "Recent status of fluidized bed technologies for producing iron input materials for steelmaking," Particuology, vol. 9, pp. 14–23, 2011, doi: 10.1016/j.partic.2010.08.011.

[34] Metso Outotec, "Circored™ : 100% Hydrogen-based Fine Ore Reduction as one route to CO2 neutral steelmaking", 2023. URL: https://www.metso.com/portfolio/circored-hydrogen-based-

reduction/?r=3#:~:text=The%5C%20Circored%5C%20process,indicated%5C%20by%5C%20the%5C%20gray%5C%20circle (last visited on 22.08.2023)

[35] A. Brent, P. Mayfield, T: Honeyands, "The Port Hedland FINMET (R) Project - Fluid bed Production of High Quality Virgin Iron for the 21st Century.", 1997.

[36] Primetals Technologies Ltd. and Posco Ltd., The Finex® Process: Economical and Environemtally safe ironmaking, 2020, URL: https://www.primetals.com/fileadmin/user_upload/content/01_portfolio/1_ironmaking/finex/THE_FINEX_R__PROCESS.pdf (last visited on 24.08.2023)

[37] Federal Ministry Republic of Austria: Climate Action, Environment, Energy, Mobility, Innovation and Technology, "HYFOR® - Hydrogen-based technology for iron- and steelmaking." URL: https://www.energy-innovation-austria.at/article/hyfor/?lang=en# (last (last visited on 12.01.2024)

[38] D. Spreitzer, J. Wurm, B. Hiebl, N.Rein, T. Wolfinger, W. Sterrer, A.Fleischanderl, HYFOR-Hydrogen based Fine-Ore Reduction, Mitsubishi Heavy Industries Technial Review, vol. 59, no. 2, 2022.

[39] L. R. Glicksman, "Scaling relationships for fluidized beds," Chem Eng Sci, vol. 39, no. 9, pp. 1373–1379, Jan. 1984, doi: 10.1016/0009-2509(84)80070-6.

[40] L. R. Glicksman, M. Hyre, and K. Woloshun, "Simplified scaling relationships for fluidized beds," Powder Technol, vol. 77, no. 2, pp. 177–199, Nov. 1993, doi: 10.1016/0032-5910(93)80055-F.

[41] L. R. Glicksman, "Scaling relationships for fluidized beds," Chem Eng Sci, vol. 43, no. 6, pp. 1419–1421, Jan. 1988, doi: 10.1016/0009-2509(88)85118-2.

[42] J. C. Schmid, T. Pröll, C. Pfeifer, R. Rauch, and H. Hofbauer, "Cold Flow Model Investigation on a Modified Riser with Enhanced Gas-Solid Contact: Locating the Regions of Operation in a Fluidization Regime Map", Proc.21st Int. Conf. Fluid. Bed. Combust. (FBC), pp. 80-87, 2012.

[43] T. Wolfinger, D. Spreitzer, and J. Schenk, "Analysis of the Usability of Iron Ore Ultra-Fines for Hydrogen-Based Fluidized Bed Direct Reduction—A Review," Materials 2022, Vol. 15, Page 2687, vol. 15, no. 7, p. 2687, Apr. 2022, doi: 10.3390/MA15072687.

[44] L. Reh, Das Wirbeln von Körnigem Gut im Schlanken Diffusor als Grenzzustand Zwischen

Wirbelschicht und Pneumatischer Förderung, Technische Hochschule Karlsruhe, 1961.

[45] J. R. Grace, "Contacting modes and behaviour classification of gas—solid and other two-phase suspensions," Can J Chem Eng, vol. 64, no. 3, pp. 353–363, Jun. 1986, doi: 10.1002/cjce.5450640301.

[46] X. Liu et al., "Measuring Technologies for CFB Solid Circulation Rate: A Review and Future Perspectives," Energies (Basel), vol. 15, no. 2, 2022, doi: 10.3390/en15020417.

[47] A. Habermann, "Kinetik der Eisenerzreduktion in der Wirbelschicht", Ph.D. Thesis, Institut für Verfahrenstechnik, Umwelttechnik und technische Biowissenschaften, TU Wien, 2001.

[48] Haberkorn, "Rotameter Gestell." 2023.

[49] A. Walla, "Design Principles of a Fluidized Bed Experimental Unit for Iron Ore Reduction with Hydrogen", Institut für Verfahrenstechnik, Umwelttechnik und technische Biowissenschaften, TU Wien, 2023.

[50] National Institute of Standards and Technology, NIST Chemistry WebBook, SRD 69, 2023, doi: https://doi.org/10.18434/T4D303, URL: https://webbook.nist.gov/chemistry/ (last visited on 12.01.2024)

Symbols

Ar	Archimedes Number	[-]
c_w	Drag coefficient	[-]
d_p	Particle diameter	m
d_{SV}	Equivalent diameter; diameter of a sphere with the same surface area and volume as the particle	m
$\overline{d_p}$	Mean particle diameter	m
Fr	Froude number	[-]
g	Gravitational force (=9.81 m/s^2)	m/s^2
G_s	Feed/circulation rate	kg/m^2s
H	Bed height	m
m_p	Mass of bed of particles	kg
M_i	Molar mass of component i	kg/mol
n	Number of mol	mol
p	Pressure	Pa
R	Gas costant (8,314 J/molK)	J/molK
Re	Reynolds number	[-]
S_p	Particle Surface	m^2
T	Temperature	°C
U	Superficial velocity	m/s
U_{mf}	Minimum fluidization velocity	m/s
$U_{mf,exp.}$	Experimental minimum fluidization velocity	m/s

$U_{mf,theoret.}$	Theoretical minimum fluidization velocity	m/s
U_t	Terminal velocity	m/s
$\bar{u}$	Fluid velocity (Glicksman)	m/s
$\bar{v}$	Particle velocity (Glicksman)	m/s
V_p	Volume of bed of particles	m^3
V_{pores}	Pore volume	m^3
V_i	Volume of component. i of a gas mixture	m^3
x_i	Mole fraction of component i	mol/mol
X	Molar load of oxygen	mol O/mol Fe
y_i	Mass share of component i	kg/kg
Z	Compressibility factor (Z=1 for ideal gas)	-
Δp	Pressure loss	Pa
Δp_{exp}	Experimental pressure loss	Pa
$\Delta p_{theoret.}$	Theoretical pressure loss	Pa
ε	Porosity of the bed (void fraction)	[-]
ρ_{bulk}	Bulk density	kg/m^3
ρ_g	Gas density	kg/m^3
ρ_p	Particle density	kg/m^3
$\rho_{p,porous}$	Porous particle density	kg/m^3
$\rho_{p,mix}$	Density of the sample mixture	kg/m^3
$\rho_{p,theoretical}$	Theoretical density	kg/m^3
μ	Dynamic gas viscosity	Pa s

ν	Kinematic gas viscosity	m^2/s
φ	Sphericity of a particle	[-]

List of tables

Table 1: Dimensionless numbers 33

Table 2: Dimensionless numbers for Reh Diagram 34

Table 3: Dimensionless numbers for Grace Diagram 35

Table 4: Assumptions for lowest and highest particle diameters 41

Table 5: Calculation of Flowrates for Rotameter assuming air as fluidization gas 41

Table 6: Calculation of Flowrates for Rotameter assuming helium as fluidization gas 41

Table 7: Rotameter - Flowrates 42

Table 8: Sample Mixtures – Test Matrix 43

Table 9: Constants A-E for hydrogen for calculation of its dynamic viscosity 45

Table 10: Theoretical data for similarity parameters assuming iron ore as particle 49

Table 11: Theoretical data for similarity parameters assuming silica sand as particle 49

Table 12: Validation samples 51

Table 13: Calculation Parameters 53

Table 14: Test Results 53

Table 15: Validation results 54

Table 16: Silica Sand - Particle Distribution Size 55

Table 17: Sieve analysis result - average diameter (silica sand) 56

Table 18: Iron Ore - Particle distribution size 58

Table 19: Sieve analysis result - average diameter (iron ore) 59

Table 20: Sieve analysis result - average diameter (Samples P1-P10) 62

Table 21: Legend for Table 22 and Table 23 – ratio of minimum fluidization velocities 78

Table 22: Comparison of Theoretical and Experimental Data - Comparison of Sample Mixtures

P1-P5 83

Table 23: Comparison of Theoretical and Experimental Data - Comparison of Sample Mixtures P5-P10 84

Table 24: Comparison of Theoretical and Experimental Data - Comparison of Air vs Helium 85

Table 25: Bed Material Losses for samples P3-P5 87

Table 26: Comparison of Theoretical and Experimental Data – Influence of the Presence of a Cyclone on the Cold Model Experiments 88

List of figures

Figure 1: Types of fluidization [6] 4

Figure 2: Geldart Characteristics of Particles [9] 7

Figure 3: Acting forces on spherical particle[10] 12

Figure 4: Pressure drop as a function of superficial velocity [7] 14

Figure 5: Pressure drop as a function of superficial velocity for a wide size distribution of particles [6] 15

Figure 6: Fe - O binary system [21] 17

Figure 7: Baur - Glässner diagram for metallic iron, wüstite, magnetite, hematite and a CO_2/CO mixture [23] 19

Figure 8:Baur - Glässner Diagram for metallic iron, wüstite, magnetite, hematite and a H2/H2O mixture [21] 20

Figure 9: Reduction mechanism - mass transfer phenomena [24], [25] 21

Figure 10: Crude steel production methods [30] 22

Figure 11: Blast furnace [31] 23

Figure 12: Classification of direct reduction processes [33] 25

Figure 13: Flowchart of the Circored® process [34] 26

Figure 14: Flowsheet of the Finmet® Process [35] 28

Figure 15: Flowsheet of the FINEX® Process [36] 29

Figure 16: Schematic flowsheet of the HYFOR® pilot plant [38] 30

Figure 17: HYFOR Industrial Prototype Plant - Schematic Flowsheet [38] 31

Figure 18: Fluidization regime map following Reh[44] 35

Figure 19: Fluidization regime map following Grace [45] 36

Figure 20: Flow chart of the compressed fluidized bed reactor [24] 39

Figure 21:a) Front view of test rack with dimensions; b) Side view of test rack with dimensions; c) Back of view of the rack[48] 40

Figure 22: Cold Model - Experimental Setup 42

Figure 23: Temperature Dependence of Density 45

Figure 24: Temperature Dependence of Kinematic Viscosity 46

Figure 25: Temperature Dependence of Archimedes Number 47

Figure 26: Temperature Dependence of Minimum Fluidization Velocity 47

Figure 27 and Figure 28: Particle size distributions for Samples A1 and A2 51

Figure 29: Particle size distribution for sample A3 51

Figure 30: Pressure loss diagram for sample A1 52

Figure 31: Pressure loss diagram for sample A3 52

Figure 32: Correction of Rotameter Flowrate by Gas Meter (Air) 54

Figure 33: Correction of Rotameter Flowrate by Gas Meter (Helium) 55

Figure 34: Particle size distribution for silica sand of a particle size range 0.1-0.8 mm 56

Figure 35: Particle size distribution for silica sand of a particle size range 0.1-0.2 mm 57

Figure 36: Ar Number Distribution for silica sand of a particle size range 0.1-0.8 mm 57

Figure 37: Ar Number Distribution for silica sand of a particle size range 0.1-0.2 mm 58

Figure 38: Particle size distribution for iron ore of a particle size range 0.063-0.125 mm ... 58

Figure 39: Particle size distribution for iron ore of a particle size range 0.5-1 mm 59

Figure 40: Ar Number Distribution for silica sand of a particle size range 0.063-0.125 mm . 59

Figure 41: Ar Number Distribution for silica sand of a particle size range 0.5-1 mm 60

Figure 42: Particle size distributions for samples P4 and P5 60

Figure 43: Ar Number distributions for samples P4 and P5 61

Figure 44: Particle size distributions for samples P9 and P10 61

Figure 45: Geldart Diagram - Samples P1-P10 [9] 63

Figure 46: Reh Diagram - Samples P1-P10 for air and helium as fluid..... 63

Figure 47: Grace Diagram - Samples P1-P10 for air and helium as fluid 64

Figure 48: Calculation Parameters 65

Figure 49: Pressure loss of the empty model caused by the sieve using air 66

Figure 50: Pressure loss of the empty model caused by the sieve using helium..... 67

Figure 51: Pressure loss vs gas velocity of sample P1 (80 % 0.1-0.8 mm Silica Sand/ 20 % 0.063-0.125 mm Iron Ore) with air and no cyclone..... 68

Figure 52: Pressure loss vs gas velocity of sample P1 (80 % 0.1-0.8 mm Silica Sand/ 20 % 0.063-0.125 mm Iron Ore) with air and no cyclone..... 68

Figure 53: Pressure loss vs gas velocity of sample P2 (60 % 0.1-0.8 mm Silica Sand/ 40 % 0.063-0.125 mm Iron Ore) with helium and no cyclone..... 69

Figure 54: Pressure loss vs gas velocity of sample P3 (20 % 0.1-0.8 mm Silica Sand/ 80 % 0.063-0.125 mm Iron Ore) with air and no cyclone..... 70

Figure 55: Pressure loss vs gas velocity of sample P3 (20 % 0.1-0.8 mm Silica Sand/ 80 % 0.063-0.125 mm Iron Ore) with helium and no cyclone..... 71

Figure 56: Pressure loss vs gas velocity of sample P4 (80 % 0.1-0.2 mm Silica Sand/ 20 % 0.063-0.125 mm Iron Ore) with air and no cyclone..... 71

Figure 57: Pressure loss vs gas velocity of sample P5 (60 % 0.1-0.2 mm Silica Sand/ 40 % 0.063-0.125 mm Iron Ore) with air and no cyclone..... 72

Figure 58: Pressure loss vs gas velocity of sample P6 (80 % 0.5-0.8 mm Silica Sand/ 20 % 0.063-0.125 mm Iron Ore) with air and no cyclone..... 73

Figure 59: Pressure loss vs gas velocity of sample P6 (80 % 0.5-0.8 mm Silica Sand/ 20 % 0.063-0.125 mm Iron Ore) with air and with internal cyclone 73

Figure 60: Pressure loss vs gas velocity of sample P7 (60 % 0.5-0.8 mm Silica Sand/ 40 %

0.063-0.125 mm Iron Ore) with helium and with internal cyclone 74

Figure 61: Pressure loss vs gas velocity of sample P8 (60 % 0.8-1 mm Silica Sand/ 40 % 0.5-1 mm Iron Ore) with air and no cyclone 74

Figure 62: Pressure loss vs gas velocity of sample P9 (80 % 0.5-1 mm Silica Sand/ 20 % 0.5-1 mm Iron Ore) with air and no cyclone 75

Figure 63: Pressure loss vs gas velocity of sample P9 (80 % 0.5-1 mm Silica Sand/ 20 % 0.5-1 mm Iron Ore) with helium and no cyclone 76

Figure 64: Pressure loss vs gas velocity of sample P10 (60 % 0.5-1 mm Silica Sand/ 40 % 0.5-1 mm Iron Ore) with air and no cyclone 76

Figure 65: Dependence of minimum fluidization velocity on fluidization gas and particle diameter of mixture components 79

Figure 66: Dependence of the iron ore and silica sand particle diameter on the minimum fluidization velocity 80

Figure 67: Dependence of the minimum fluidization velocity and the fluid density (assuming particle density of silica sand) 81

Figure 68: Dependence of the minimum fluidization velocity and the fluid viscosity (assuming particle density of silica sand) 81

Figure 69: Pressure loss vs gas velocity of sample P5 (60 % 0.1-0.2 mm Silica Sand/ 40 % 0.063-0.125 mm Iron Ore) with air and with internal cyclone 86

Appendix

ad, Table 10/11 S.48

$$Ar_{iron\,ore,He(25°C,1.013\,bar)} = \frac{\rho_{He}\cdot(\rho_{iron\,ore}-\rho_{He})\cdot g\cdot d_{iron\,ore}^3}{\eta_{He}^2} = \frac{0.161\cdot(4300-0.161)\cdot(0.5\cdot10^{-3}\cdot 0{,}75)^3\cdot 9.81}{(1.98\cdot10^{-5})^2}$$

(d_p: $\varphi_{iron\,ore}$; sphericity φ)

$$Ar_{iron\,ore,He(25°C,1.013\,bar)} = 911$$

$$U_{mf,iron\,ore,He(25°C,1.013\,bar)} = \frac{\eta_{He}}{\rho_{He}\cdot d_{iron\,ore}}\cdot\left[\sqrt{33.7^2+0.0408\cdot Ar_{iron\,ore,He(25°C,1.013\,bar)}}-33.7\right] =$$

$$= \frac{1.98\cdot10^{-5}}{0.16\cdot0.5\cdot10^{-3}\cdot0.75}\cdot\left[\sqrt{33.7^2+0.0408\cdot2160.54}-33.7\right] = 0.18\ m/s$$

$$U_{iron\,ore,He(25°C,1.013\,bar)} = 3\cdot U_{mf,iron\,ore,He(25°C,1.013\,bar)} = 3\cdot 0.18 = 0.54\ m/s$$

$$Re_{iron\,ore,He(25°C,1.013\,bar)} = \frac{\rho_{He}\cdot U_{iron\,ore,He(25°C,1.013\,bar)}\cdot d_{iron\,ore}}{\eta_{He}} = \frac{0.16\cdot0.54\cdot0.5\cdot10^{-3}\cdot0.75}{1.98\cdot10^{-5}} = 1.64$$

$$Fr_{iron\,ore,He(25°C,1.013\,bar)} = \frac{U^2_{iron\,ore,He(25°C,1.013\,bar)}}{g\cdot d_{iron\,ore}} = \frac{0.54}{9.81\cdot0.5\cdot10^{-3}\cdot0.75} = 79$$

ad, Grace Diagram S.63

Point P1 ⊗

$$\rho_{P1mix} = Y_{iron\,ore}\cdot\rho_{iron\,ore} + Y_{sand}\cdot\rho_{sand} = 0.2\cdot4300 + 0.8\cdot2600 = 2940\ kg/m^3$$

$$Ar_{P1,He} = \frac{\rho_{He}\cdot(\rho_{P1mix}-\rho_{He})\cdot g\cdot d_{P1}^3}{\eta_{He}^2} = \frac{0.1614\cdot(2940-0.1614)\cdot9.81\,(0.155\cdot10^{-3}\cdot0.8)^3}{(1.9846\cdot10^{-5})^2} = 22.37$$

$$U_{mf,P1,He} = \frac{\eta_{He}}{\rho_{He}\cdot d_{iron\,ore}}\cdot\left[\sqrt{33.7^2+0.0408\cdot Ar_{P1,He}}-33.7\right] =$$

$$= \frac{1.9846\cdot10^{-5}}{0.1614\cdot0.155\cdot10^{-3}\cdot0.8}\cdot\left[\sqrt{33.7^2+0.0408\cdot22.37}-33.7\right] = 0.0135\ m/s$$

$$U_{P1,He} = 3\cdot U_{mf,P1,He} = 3\cdot0.0135 = 0.04\ m/s$$

$$Re_{P1,He} = \frac{\rho_{He}\cdot U_{P1,He}\cdot d_{P1}}{\eta_{He}} = \frac{0.1614\cdot0.04\cdot0.155\cdot10^{-3}\cdot0.8}{1.9846\cdot10^{-5}} = 0.05$$

$$d^*_{P1} = (Ar_{P1,He})^{\frac{1}{3}} = (22.37)^{\frac{1}{3}} = 2.82$$

$$u^*_{P1} = \frac{Re_{P1,He}}{(Ar_{P1,He})^{\frac{1}{3}}} = \frac{0.05}{2.82} = 0.018$$

ad, Table 23 S.82

Experiment P 9.3 :

- iron ore properties :

$$Ar_{pg,He,iron\ ore} = \frac{\rho_{He} \cdot (\rho_{iron\ ore} - \rho_{He}) \cdot g \cdot d_{pg}^3}{\mu_{He}^2} = \frac{0.1614 \cdot (4300 - 0.1614) \cdot 9.81 \cdot (0.717 \cdot 10^{-3} \cdot 0.75)^3}{(1.9846 \cdot 10^{-5})^2}$$

$$Ar_{pg,He,iron\ ore} = 2480.20$$

$$U_{mf,pg,He,iron\ ore} = \frac{\mu_{He}}{\rho_{He} \cdot d_{pg}} \cdot \left[\sqrt{33.7^2 + 0.0408 \cdot Ar_{pg,He,iron\ ore}} - 33.7 \right] =$$

$$= \frac{1.9846 \cdot 10^{-5}}{0.1614 \cdot 0.717 \cdot 10^{-3} \cdot 0.75} \cdot \left[\sqrt{33.7^2 + 0.0408 \cdot 2480.20} - 33.7 \right] = 0.345\ m/s$$

- silica sand properties :

$$Ar_{pg,He,sand} = \frac{\rho_{He} \cdot (\rho_{sand} - \rho_{He}) \cdot g \cdot d_{pg}^3}{\mu_{He}^2} = \frac{0.1614 \cdot (2600 - 0.1614) \cdot 9.81 \cdot (0.717 \cdot 10^{-3} \cdot 0.75)^3}{(1.9846 \cdot 10^{-5})^2}$$

$$Ar_{pg,He,sand} = 1993.80$$

$$U_{mf,pg,He,sand} = \frac{\mu_{He}}{\rho_{He} \cdot d_{pg}} \cdot \left[\sqrt{33.7^2 + 0.0408 \cdot Ar_{pg,He,sand}} - 33.7 \right] =$$

$$= \frac{1.9846 \cdot 10^{-5}}{0.1614 \cdot 0.717 \cdot 10^{-3} \cdot 0.75} \cdot \left[\sqrt{33.7^2 + 0.0408 \cdot 1993.80} - 33.7 \right] = 0.253\ m/s$$

- mixture properties :

$$Ar_{pg,He,mix} = \frac{\rho_{He} \cdot (\rho_{mix} - \rho_{He}) \cdot g \cdot d_{pg}^3}{\mu_{He}^2} = \frac{0.1614 \cdot (2940 - 0.1614) \cdot 9.81 \cdot (0.717 \cdot 10^{-3} \cdot 0.75)^3}{(1.9846 \cdot 10^{-5})^2}$$

$$Ar_{pg,He,mix} = 2228.96$$

$$U_{mf,pg,He,mix} = \frac{\mu_{He}}{\rho_{He} \cdot d_{pg}} \cdot \left[\sqrt{33.7^2 + 0.0408 \cdot Ar_{pg,He,mix}} - 33.7 \right] =$$

$$= \frac{1.9846 \cdot 10^{-5}}{0.1614 \cdot 0.717 \cdot 10^{-3} \cdot 0.75} \cdot \left[\sqrt{33.7^2 + 0.0408 \cdot 2228.96} - 33.7 \right] = 0.316\ m/s$$